國立臺灣大學光電工程學研究所

碩士論文

Graduate Institute of Photonics and Optoelectronics

National Taiwan University

Master Thesis

氮化銦鎵, 氮化鋁鎵, 碳化矽及氮化銦鎵/氮化鎵多重量子井之布里淵散射光譜與材料研究

Brillouin Scattering Spectroscopy and Material Studies of InGaN, AlGaN, SiC and InGaN/GaN Multi-Quantum Wells Light Emitting Diodes

吳宗翰

Wu, Tsung Han

指導教授: 馮哲川 博士

Advisor: Feng, Zhe-Chuan Ph.D.

中華民國九十九年 7 月

國立臺灣大學光電工程學研究 碩士論文 氮化銦鎵，氮化鋁鎵，碳化矽及氮化銦鎵／氮化鎵多重量子井之布里淵散射光譜與材料研究 吳宗翰 撰 99 7

國立臺灣大學碩士學位論文
口試委員會審定書

氮化銦鎵、氮化鋁鎵、碳化矽及氮化銦鎵/氮化鎵多重量子井之布里淵散射光譜與材料研究
Brillouin Scattering Spectroscopy and Material Studies of InGaN, AlGaN, SiC and InGaN/GaN Multi-Quantum Wells Light Emitting Diodes

本論文係吳宗翰君（學號 R97941106）在國立臺灣大學光電工程學研究所完成之碩士學位論文，於民國 99 年 7 月 27 日承下列考試委員審查通過及口試及格，特此證明

口試委員：

馮哲川 （指導教授）

陳雅義　　盛芳銘

所長 黃炎龍

誌謝

首先,我要感謝我的指導教授馮哲川教授，從進入實驗室的第一天起就不斷的督促著我，在老師的細心指導下，我在研究所期間接觸了很多種不同的量測技術，也學習到如何獨當一面、解決問題的能力。老師除了提供我在學術領域的專業知識外，更教導了我許多做學問的態度以及待人處事的方法。這些可貴的經驗，使我獲益良多，也成長了不少。

感謝一路上曾給予我幫助的人，感謝中研院地科所林忠成博士及楊翊中博士在布里淵散射實驗上給予我相當多的幫助與指導，並熱心的教誨我軟體操作及相關問題 。 感謝同步輻射中心張凌雲博士以及李振民經理的幫助讓我得以順利地完成實驗，感謝實驗室的所有同學及學長，因為有你們，研究過程才能這麼的充實與豐富，我們一起度過了許多歡樂時光，我們一起創造了許多深刻的回憶，研究所兩年多期間，多虧有你們的一路相隨，我將會銘記在心。

最後我要感謝我的家人，你們是我一路走來最大的依靠，過程雖然不盡順遂，但有你們的支持與鼓勵，我才能心無旁騖的完成我的論文，拿到碩士學位。

摘要

光學量測對於分析半導體材料具有很重要的地位，尤其是對於材料的結構、特性，甚至是物理機制。而近幾年的半導體材料，由於它的材料特性非常適合應用在現今生活的電器設備用品上，譬如：發光二極體、積體電路原件…等，所以被廣泛而且深入的研究，縱使已經有不少上市產品應用半導體為材料，但是仍然有許多的問題與困難需要解答與突破，因此，我們將針對目前的許多挑戰做研究。

我們會利用各種不同的光學量測系統得到更多的材料特性。在第三章，我們利用布里淵散射光譜量測氮化鎵，氮化銦鎵以及不同鋁含量的氮化鋁鎵之布里淵位移頻率。藉由聲子縱波與橫波的位移頻率進而算出聲速，然後利用克里斯托夫方程式得到其彈性常數。藉由拉曼散射中，縱向光學聲子的位移量來判斷估計出不同氮化鋁鎵材料中的鋁含量，並用X光繞射譜來分析樣品內部的材料結構以及結晶性的好壞。在第四章，利用同步輻射X光吸收光源精細結構頻譜圖探討參雜濃度不同的碳化矽樣品中，矽原子跟鄰近碳原子的距離變化，也討論參雜濃度對拉曼光譜的影響。在第五章中，我們量測的是不同溫度生長方向的氮化銦鎵/氮化鎵多重量子井發光二極體之光電性質，由變溫光激螢光光譜了解其發光現象，然後利用時間鑑別光激發光頻譜，來測定樣品的衰退時間。

Abstract

The III–V nitrides GaN, AlN, InN and their ternary compounds are of significant technological importance for semiconductor device applications in the blue and UV wavelengths, such as light-emitting diodes and semiconductor lasers. These nitrides possess large direct bandgaps, extremely high hardness, very large heterojunction offsets, high thermal conductivity and high melting temperature, which also make them promising candidates for high-temperature and high-power devices.

In chapter 3, we measured the Brillouin scattering spectroscopy of GaN, InGaN, and AlGaN. The Brillouin shift frequencies have obtained from the spectra, and the acoustic velocities can be calculated. Further, the elastic constants can be computed by Christiffel's equation. The shifts of A1(LO) peak in Raman scattering spectroscopy can determine the aluminum contents in AlGaN sample. And X-ray diffraction (XRD) show us the sample's crystallinity. In chapter 4, we discuss the distance between silicon atom and neighbor carbon atom by extended X-ray absorption fine structure, and try to realize how the nitrogen doped concentrations affect the Raman scattering spectrum. We investigate the InGaN/GaN multiple-quantum well with different growth direction in chapter 5. Via PL spectra to analyze the temperature-dependent emission energy. Besides, the temperature TRPL measurement results show that sample's decay time.

Content

口試委員會審定書.....

誌謝.....I

摘要.....II

Abstract.....III

Content.....IV

Lists of Figures.....VIII

Lists of Tables.....XIV

Chapter 1 Introduction

1.1. Publication……...1

1.1.1. Conference or Proceeding Papers…….1

1.2. III-Nitride semiconductors……...2

1.3. Properties of AlGaN alloys…….…4

1.4. Properties of InGaN…….....6

1.5. SiC……....8

Reference……..10

Chapter 2 Theoretical Background and Experimental Details

2.1. Introduction of Brillouin scattering spectroscopy……..…13

2.1.1 History……...…….. 13

2.1.2 Spectrometer……14

2.1.3 Principles……..14

2.1.4 Application……15

2.2. Photoluminescence (PL)……16

2.3. Raman Scattering (RS)……...19

2.4. Time-Resolved Photoluminescence (TRPL)……..20

Reference ……24

Chapter 3 Brillouin scattering and the other material studies of GaN, InGaN, and AlGaN

3.1 InGaN/GaN Heterostructure Grown on Sapphire Substrate by Metalorganic Chemical Vapor Deposition……..27

3.1.1 Introduction……27

3.1.2 Experimental……...28

3.1.3 Results and discussion……29

3.1.3.1 Brillouin scattering……..…29

3.1.3.2 Photoluminescence (PL)……..36

3.1.3.3 Optical transmission (OT)……..……37

3.1.4 Summary…….……....38

3.2 AlGaN Grown on Sapphire Substrate by Metalorganic Chemical Vapor Deposition……..……..39

3.2.1 Introduction……39

3.2.2 Experimental……...40

3.2.3 Result and discussion……..43

3.2.3.1 Brillouin scattering……..43

3.2.3.2 High-resolution X-ray Diffraction Measurement…50

3.2.3.3 Raman scattering (RS)……52

3.2.4 Summary……55

References……...…55

Chapter 4 Synchrotron Radiation and Related Studies on 6H-SiC materials

4.1 Introduction……....59

4.1.1 Silicon carbide…….…....59

4.1.2 Synchrotron radiation beamline end station……61

4.2 Result and discussion……...65

4.2.1 Sample information……65

4.2.2 Raman Scattering……...……65

4.2.3 X-ray Absorption Fine-Structure Study on 6H-SiC……...67

4.2.4 X-ray absorption near edge spectroscopy (XANES)…….76

4.3 Summary……77

References……77

Chapter 5 Optical Study of InGaN/GaN Multi-quantum Wells Structures Light Emitting Diode

5.1. Sample Information……81

5.2. Optical Measurement and analysis…….82

5.2.1 PL Experimental Results……..……..…82

5.2.2 Activation energy……..……89

5.2.3 Photoluminescence Excitation Experimental Results...…91

5.2.4 TRPL experimental results……....94

5.3 Summary……..…104

References……..105

Chapter 6 Others

6.1. Brillouin scattering spectrum of 6H-SiC……..…107

6.1.1. Introduction……...…107

6.1.2. Ressults…….…….108

6.2. InGaN N K-edge X-ray Asorption Near Edge Spectroscopy (XANES)……..111

6.2.1. Synchrotron Radiation Beamline End Station……...111

6.2.2. Ressults……..……114

References……...……...117

Lists of Figures

Figure 2.1 *Energy transitions in (a) direct and (b) indirect gap semiconductors between initial states E_i and final states E_f. For indirect transitions, the participation of a phonon (E_{ph}) is required*.....17

Figure 2.2 *the schematic representation of low temperature photoluminescence (after R. A. Strading and P. C. Klipstein)*.....18

Figure 3.1 *Representative Brillouin spectra of GaN on sapphire at Ψ=105°*.....29

Figure 3.2 *Representative Brillouin spectra of $In_{0.02}Ga_{0.98}N$ on sapphire at Ψ=45°* 30

Figure 3.3 *Sketch of the incident light and scattered light*..... 31

Figure 3.4 *(a) Acoustic velocities versus Ψ angle of GaN*

(b) Acoustic velocities versus Ψ angle of $In_{0.02}GaN_{0.98}$ 1940i..... 33

Figure 3.5 *Acoustic velocities versus Ψ angle of GaN (dash lines and dash dots) and $In_{0.02}GaN_{0.98}$ (solid lines and solid dots)*.....34

Figure 3.6 *Product of density times velocity squared versus propagation angle about GaN*.....34

Figure 3.7 *Representative Brillouin spectra of $In_{0.15}Ga_{0.85}N$ on sapphire at Ψ=0°*...36

Figure 3.8 *Representative Brillouin spectra of $In_{0.29}Ga_{0.71}N$ on sapphire at Ψ=0°*...36

Figure 3.9 *PL spectra of $In_xGa_{1-x}N$ on sapphire*.....37

Figure 3.10 Optical transmittance of $In_{0.02}Ga_{0.98}N$ (1940i)……...38

Figure 3.11 Schematic Structures of the samples (a) M1216, (b) M1170, and (c)M1686……41

Figure 3.12 Schematic Structures of the samples M1052……...42

Figure 3.13 Representative Brillouin spectra of $Al_{0.2}Ga_{0.8}N$ on sapphire at Ψ＝15°…43

Figure 3.14 Representative Brillouin spectra of $Al_{0.4}Ga_{0.6}N$ on sapphire at Ψ＝75°…43

Figure 3.15 Representative Brillouin spectra of $Al_{0.48}Ga_{0.52}N$ on sapphire at Ψ＝120°……44

Figure 3.16 Representative Brillouin spectra of $Al_{0.62}Ga_{0.38}N$ on sapphire at Ψ＝55°……44

Figure 3.17 Acoustic velocities versus Ψ angle of (a) AlGaN~20% (b) AlGaN~40% (c) AlGaN~48% (d) AlGaN~62%…….....48

Figure 3.18 SAW (dashed line) and BAW (solid lines) velocities of different modes propagating in the of $Al_xGa_{1-x}N$ [3.16]……49

Figure 3.19 (a) XRD spectrum of $Al_xGa_{1-x}N$ (b) FWHM of XRD spectra versus aluminum contents……..……51

Figure 3.20 (a) Raman spectrum of $Al_{0.2}Ga_{0.8}N$……..……...…53

(b) Raman spectrum of $Al_{0.4}Ga_{0.6}N$……...53

(c) Raman spectrum of $Al_{0.48}Ga_{0.52}N$……..54

(d) Raman spectrum of $Al_{0.62}Ga_{0.38}N$……54

Figure 3.21 (a) *Phonon frequency of the E2 and A1(LO) phonons of $Al_xGa_{1-x}N$ as a function of the aluminum composition x, obtained at room temperature under 488 nm excitation. (From [3.18]) (b) Our results in this work*……..55

Figure 4.1 Stacking sequence of three common SiC polytypes……60

Figure 4.2 Optical Layout of BL16A…….……..64

Figure 4.3. The comparison of Raman scattering in the samples 6H-SiC…….66

Figure 4.4 The XAFS raw spectra of 6H-SiC……70

Figure 4.5 The Si K-edge oscillation $k^3\chi(k)$ for 6H-SiC 054…… ……...70

Figure 4.6 The Si K-edge oscillation $k^3\chi(k)$ for 6H-SiC 151…… ……...70

Figure 4.7 The Si K-edge oscillation $k^3\chi(k)$ for 6H-SiC 177…… ……...71

Figure 4.8 (a)Fourier Transformation spectra of 6H-SiC 054……..……72

Figure 4.9 (b)Fourier Transformation spectra of 6H-SiC 151……..……..……72

Figure 4.10 (c)Fourier Transformation spectra of 6H-SiC 177……....……..……74

Figure 4.11 The 6H-SiC crystal structure with doping nitrogen……...75

Figure 4.12 C K-edge XANES spectra……...76

Figure 5.1 Structures of the InGaN/GaN MQWs……...81

Figure 5.2 Growth direction of L46, L47, L48……..……82

Figure 5.3 Growth direction of L52……..82

Figure 5.4 The room-temperature PL spectrum of InGaN MQWs for the sample L36, L46, L47, L48 and L52. The spectrum is normalized……...….83

Figure 5.5 The room-temperature PL FHWM spectrum……..83

Figure 5.6 The PL spectra for the InGaN/GaN MQW structures in the temperature range from 10 to 300 K. (a)L36, (b)L46, (c)L47, (d)L48 and (e)L52…….85

Figure 5.7 Temperature dependence of the peak position of the QW-related emission for the InGaN/GaN blue LED structure (a)L36, (b)L46, (c)L47, (d)L48 and (e)L52……..87

Figure 5.8 Temperature dependence of the FWHM PL peak intensity of the QW-related emission for the InGaN/GaN blue LED structure (a)L36, (b)L46, (c)L47, (d)L48 and (e)L52……88

Figure 5.9 Arrhenius plot of the normalized integrated PL intensity (I_{PL}) versus temperature for the InGaN/GaN MQW structure(a)L36, (b)L46, (c)L47, (d)L48 and (e)L52. Experimental data are represented by the solid squares; the red line is a fitting curve……..……90

Figure 5.10 RTPL and PLE spectra of L36……..……91

Figure 5.11 RTPL and PLE spectra of L46……..……92

Figure 5.12 RTPL and PLE spectra of L47……..……92

Figure 5.13 RTPL and PLE spectra of L48……..……93

Figure 5.14 RTPL and PLE spectra of L52……..……93

Figure 5.15 (a) Measured TRPL (10K) for the InGaN/GaN MQW LED structure (L36) with detecting wavelength at λ= 445.2, and 459.2 nm, respectively. The red curve is a single exponential function fit…….……95

Figure 5.15 (b) Measured TRPL (10K) for the InGaN/GaN MQW LED structure (L46) with detecting wavelength at λ= 433.6, and 445.6 nm, respectively. The red curve is a single exponential function fit……..96

Figure 5.15 (c) Measured TRPL (10K) for the InGaN/GaN MQW LED structure (L47) with detecting wavelength at λ= 447, and 471 nm, respectively. The red curve is a single exponential function fit……...……97

Figure 5.15 (d) Measured TRPL (10K) for the InGaN/GaN MQW LED structure (L48) with detecting wavelength at λ= 425.2, and 445.2 nm, respectively. The red curve is a single exponential function fit……..98

Figure 5.16 Photon energy dependence of PL lifetime τ_{PL} for the InGaN/GaN MQW (a) L36, (b) L46, (c) L47, and (d) L48 at 10K……101

Figure 5.17 Temperature dependence of PL lifetime τ_{PL} for the InGaN/GaN MQW (a)L36, (b)L46, (c)L47, (d)L48. in the temperature range from 10 K to 300 K……104

Figure 6.1 Brillouin spectrum of (a)6HSiC052 (b)6HSiC177 (C)6HSiC intrinsic

(d) Brillouin spectrum of (a), (b), and (c) in one figure……..109

Figure 6.2 (a) Elastic constants fitting results of 6H052……110

Figure 6.2 (b) Elastic constants fitting results of 6H177……110

Figure 6.2 (c) Elastic constants fitting results of 6H intrinsic……..……...…111

Figure 6.3 Photon flux of BL20A,,,,,,,,,……..113

Figure 6.4. Fitting of a representative spectrum from a hexagonal GaN

from [6.9]……..…115

Figure 6.5 N K-edge XANES of $In_xGa_{1-x}N$……117

List of Tables

Table 3.1 Brillouin frequency shifts ($\Delta\omega$) and acoustic velocities of GaN……..……..31

Table 3.2 Brillouin frequency shifts ($\Delta\omega$) and acoustic velocities of $In_{0.02}Ga_{0.98}N$ ….32

Table 3.3 Elastic constant of GaN from [3.4,3.5] , fitting, and $In_{0.02}Ga_{0.98}N$……35

Table 3.4 Brillouin frequency shifts ($\Delta\omega$) and acoustic velocities of $Al_{0.2}Ga_{0.8}N$…….45

Table 3.5 Brillouin frequency shifts ($\Delta\omega$) and acoustic velocities of $Al_{04}Ga_{0.6}N$……..46

Table 3.6 Brillouin frequency shifts ($\Delta\omega$) and acoustic velocities of $Al_{048}Ga_{0.52}N$…...46

Table 3.7 Brillouin frequency shifts ($\Delta\omega$) and acoustic velocities of $Al_{0.62}Ga_{0.38}N$…...47

Table 3.8 Elastic constants of GaN, $Al_xGa_{1-x}N$, and AlN……50

Table 3.9 Raman mode of $Al_xGa_{1-x}N$……..……..55

Table 4.1 SiC Polytype of 6H……..61

Table 4.2 BL16A DCM Tender X-ray Beamline……..……63

Table 4.3 Optical Parameters of BL16A……..……..64

Table 4.4 Characteristics of DCM Tender X-ray Beamline……..……64

Table 4.5 Facilities in Experimental Station of BL16A……..……65

Table 4.6 Sample information of 6H-SiC……..……65

Table 4.7 Statics of Raman fitting……..……67

Table 4.8 EXAFS Model of 6H-SiC……69

Table 4.9 Statistics of EXAFS fitting in 6H-SiC……73

Table 4.10 The electronegativity……74

Table 5.1 Activation energy (E_a) obtained from equation (5.1)……91

Table 5.2 Radiative lifetime, the energy similar to the mobility edge, and the depth of localization (τ_{rad}, E_{me}, and E_0) obtained from equation (5.2)……102

Table 6.1 Light source of BL20A……112

Table 6.2 Optical Parameters……112

Table 6.3 Calculated Resolutions……113

Table 6.4 G_1~G_6 position of GaN and $In_xGa_{1-x}N$……116

Chapter 1 Introduction

1.1 Publication

In this thesis, we have investigated the optical and structure properties of many wide band gap semiconductor materials and already published or submitted. Below are the publication lists:

1.1.1 Conference or Proceeding Papers:

(1) I-Hsiang Hung, You-Ren Lan, Tsung Han Wu, Zhe Chuan Feng, Nola Li, Hongbo Yu, Ian Ferguson, and Weijie Lu, "Nanoscale InGaN/GaN on ZnO substrate for LED applications", SPIE 7422-19, 12-pages, oral, San Diego, 2-6 August (2009).

(2) Yu Li Wu, Tsung Han Wu, Zhe Chuan Feng, Jyh-Fu Lee, Ian Ferguson, and Weijie Lu, "Extended X-ray Absorption Fine-Structures from MOCVD-Grown Si-doped GaN on Sapphire", Optics and Photonics Taiwan (OPT) 2009, AO125, 3-pages.

(3) Tsung-Han Wu, Zhe Chuan Feng, Chung-Cherng Lin, Weijie Lu, "A Brillouin scattering study of indium gallium nitride", *White LEDs 2009, 13-16 Dec 2009, Taipei, 2-pages, PO-8.*

(4) Fangfei Li, Tsung-Han Wu, Zhe Chuan Feng, Chung-Cherng Lin, Weijie Lu, " Brillouin scattering study of gallium nitride", The 13th International Conference on Phonon Scattering in Condensed Matter (Phonon 2010), Oral, p.189.

(5) Tsung Han Wu, Zhe Chuan Feng, Fangfei Li, Chung Cherng Lin, Ian Ferguson, Ray-Hua Horng and Weijie Lu, "Brillouin scattering studies of gallium nitride and Indium gallium nitride", ICORS 2010, 2-pages, #116.

(6) Tsung Han Wu, Chung Cherng Lin, Ian Ferguson, Dong-Sing Wuu, Gu Xu and Zhe Chuan Feng, "Brillouin scattering studies of aluminum gallium nitride", 16th MicroOptics Conference (MOC 2010), Oct31-Nov3, Hsingchu, Taiwan, submitted.

1.2 III-Nitride semiconductors

In the last three decades, the group III-nitride wide-band-gap semiconductors with strong bond strength have been recognized as very important materials for many optoelectronic devices, such as blue ultraviolet (UV) light emitting diodes (LEDs), laser diodes (LDs), and high-temperature/high-power electronic devices [1.1-1.9]. Based on the III-nitride semiconductors, many studies have been published in authored book, special issues, several conferences proceedings, and the reviews. As we know, GaN, which is one of the III-nitride semiconductors, can be alloyed with one of InN or AlN. The heterostructures can be used to modulate the band gap and emission wavelength. In addition, the quantum wells (QWs) and superlattice can be well fabricated by using AlGaN or GaN as the barrier and cladding layers [1.10-1.11]. This heterostructures technology used in the fabrication of QWs is essential for fabricating modern devices, such as solid-state LEDs and LDs. In fact, InGaN/GaN multiple quantum wells (MQWs)

heterostructures have successfully been used as the active layers in LEDs and LDs. InGaN/GaN MQWs are indispensable for LEDs since the incorporation of small Indium in the active GaN layer increase the luminescence efficiency considerably. LEDs based on the InGaN/GaN MQWs structures in the visible light regions of the spectrum have been also commercialized nowadays. Let us take solid-state LEDs as an example. LEDs with high external efficiency are currently in high demand for a variety of applications including flat panel displays, printers; optical interconnects in computers, and general lighting. A number of specific physical phenomena have been observed in InGaN/GaN QWs, including the quantum-confined Stark effect (QCSE), and strong optical anisotropy [1.12]. The study of the QCSE is important both for fundamental physics and device applications, such as in electro-optical modulators, light-emitting devices, and quantum information technology. In wurtzite structural InGaN heterostructures, due to the existence of a strong piezoelectric (PZ) field [1.13], they possess many peculiar features, such as giant optical anisotropy as well as the strong QCSE induced by built-in PZ field. Therefore, the influence of the PZ field on the properties of InGaN quantum structures has attracted a great deal of attention. While the potential applications of optoelectronic devices based on III-nitride semiconductors are quite high, the work demonstrating the significance of the optical modulation on the PZ field is still very limited. Besides, it is well known that defects always play a very important role in the

determination of the quality of a working device [1.14]. There still remain many unresolved issues in the study of defect in nitride semiconductors. In other to improve the performance of nitride based devices, a complete understanding of the defects is required. In addition, several recent reports indicate that it is possible to generate spin polarized current in semiconductors without applying magnetic field, such as in GaAs and ZnSe. The research along this line is very important to put spintronics in practical application. It is therefore interesting to see whether spin generation is feasible in nitride semiconductors. Moreover, III-nitride semiconductors for spintronics open up new possibilities for devices that integrate logic and magnetic storage.

1.3 Properties of AlGaN alloys

An accurate knowledge of the compositional dependence of the barrier and well materials is requisite in attempts to analyze heterostructures, in general, and in quantum wells and superlattices, in particular. With the nitride system, a plethora of options is available for constructing such structures. The barriers can be formed of AlGaN or GaN; while depending on the barrier material; the wells can be constructed of GaN or InGaN layers. The energy bandgap of $Al_XGa_{1-X}N$ may be expressed by

$$Eg\ (GaN) = xEg\ (AlN) + (1-x)\ Eg\ (GaN) - bx\ (1-x)$$

where Eg (GaN) = 3.4 eV, Eg(AIN) = 6.2 eV, x is the AIN mole fraction, and b is the bowing parameter having controversial values, to be discussed below. It shows the

compositional dependence of the bandgap of the AlGaN, as compiled by Amano *et al*. The solid line drawn through the square data points of Amano *et al*. represents the calculated compositional dependence with the effect of strain included.

A recent Hall measurement for n-$Al_{0.09}G_{0.91}N$ demonstrated a carrier concentration of $5*10^{18}$ cm^{-3} and a mobility of 35 cm^2/Vs at 300 K. This measurement did not reveal any temperature-dependent mobility of n- $Al_{0.09}G_{0.91}N$. Other Hall measurements on Mg-doped p- $Al_{0.09}G_{0.91}N$ grown by MOVPE, however addressed the temperature of the mobility. The indicate that the hole mobility decrease with increasing temperature, reach a value of about 9 cm^2/Vs for a doping density of $1.48*10^{19}$ cm^{-3}. This low mobility is ascribed to a high carrier concentration and the inter-grain scattering present in the sample. While the lattice constant was studied, it was observed to be almost linearly dependent on the AIN mole fraction in AlGaN [1.15].

Until recently the resistivity of unintentionally doped AlGaN was believed to increase so rapidly with increasing AIN mole fraction that AlGaN became almost insulating for AIN mole fractions exceeding 20%. As the AIN mole fraction increased from 0 to 30%, then n-type carrier concentration dropped from 10^{20} to $10^{17}cm^{-3}$, and the mobility increase from 10 to 30 cm^2/Vs. An increase in the native-defect ionization energies with increasing AIN may possibly be responsible for this variation [1.16]. Our knowledge of the doping characteristics of AlGaN is still incomplete. It is not, for

example, known how the doping atoms such as Si and Mg respond to the variation of the AIN mole fraction in AlGaN. It was, however, suggested that, as the AIN mole fraction increase, the doping atom deeper into the forbidden energy bandgap. AlGaN with Al mole fraction as 50 ~ 60% dope by both n- and p- type impurity atoms. The ability to dope a high-mole fraction AlGaN, especially when low-resistivity p-type material is required, is important because it may otherwise restrict the overall characteristics of devices such as laser diodes. Until now, a low AIN mole fraction in AlGaN is considered to be sufficient for good optical-field confinement [1.17]. However, it has not yet been confirmed how well it is and, hence, this must be addressed before the potential of AlGaN respect to the other wide-bandgap semiconductors is fully realized.

1.4 Properties of InGaN

Indium gallium nitride (InGaN, $In_xGa_{1-x}N$) is a semiconductor material made of a mix of gallium nitride (GaN) and indium nitride (InN). It is a ternary group III/group V direct bandgap semiconductor. Its band gap can be tuned by varying the amount of indium in the alloy. The ratio of In/Ga is usually between 0.02/0.98 and 0.3/0.7.Indium gallium nitride is the light-emitting layer in modern blue and green LEDs and often grown on a GaN buffer on a transparent substrate as, e.g. sapphire or silicon carbide. It has a high heat capacity and its sensitivity to ionizing radiation is low (like other group

III nitrides), making it also a potentially suitable material for solar cell arrays for satellites.

InN does not mix homogeneously with GaN. In a composition regime between ~ 15% -85% Indium nitride spinodal decomposition occurs leading to In-rich and Ga-rich InGaN regions or clusters. GaN is a defect rich material with typical dislocation densities exceeding 10^8 cm^{-2}. Light emission from InGaN layers grown on such GaN buffers used in blue and green LEDs is expected to be low because of non-radiative recombination at such defects. Nevertheless InGaN quantum wells are efficient light emitters in green, blue, white and ultraviolet light-emitting diodes and diode lasers. In the indium-rich regions, with a lower bandgap than the surrounding material, most electron-hole pairs recombine and by the lower potential energy of these clusters carriers are hindered to diffuse and recombine non-radiatively at crystal defects.

The wavelength emitted, dependent on the material's band gap, can be controlled by the GaN/InN ratio, from near ultraviolet for 0.02In/0.98Ga through 390 nm for 0.1In/0.9Ga, violet-blue 420 nm for 0.2In/0.8Ga, to blue 440 nm for 0.3In/0.7Ga, to red for higher ratios and also by the thickness of the InGaN layers which are typically in the range of 2-3 nm.

This defect tolerance, together with a good spectral match to sunlight, also makes the material suitable for solar cells. It is possible to grow multiple layers with different

bandgaps, as the material is relatively insensitive to defects introduced by a lattice mismatch between the layers. A two-layer multifunction cell with bandgap of 1.1 eV and 1.7 eV can attain a theoretical 50% maximum efficiency, and by depositing multiple layers tuned to a wide range of bandgap an efficiency up to 70% is theoretically expected. Quantum heterostructures are often built from GaN with InGaN active layers. InGaN is often used together with other materials, eg. GaN, AlGaN, on SiC, sapphire and even silicon etc.

1.5 SiC

In 1824, Jons Jacob Berzelius discovered silicon carbide accidentally while he was trying to make some diamonds dreamed to be wealthy. Silicon Carbide (SiC), and also called carborundum, has caught a lot of attentions in the past decades because of its excellent material properties. Due to its good thermal conductivity, the high breakdown voltage (2.6 – 3.2 MV/cm), and the high radiation resistance, it becomes the promising material for semiconductor devices which have to work under harsh environments, such as high temperature, high frequency, and high power. However, the abrasion resistance, heat resistance and chemical resistance that make SiC a very desirable engineering material also makes manufacturing SiC products very challenging. SiC is another wide band gap material with the indirect band gap and crystallize in different modifications (polytype) [1.18]. The most important are: cubic unit cell: 3C-SiC (cubic unit cell,

zincblende); 2H-SiC; 4H-SiC; 6H-SiC (hexagonal unit cell, wurtzite); 15R-SiC (rhombohedral unit cell). 4H- and 6H-SiC are of considerable technological interest due to their large band gaps and high electron mobility. Alpha silicon carbide (α-SiC) is the most commonly encountered polymorph and has a hexagonal crystal structure (similar to Wurtzite). Pure α-SiC is an intrinsic semiconductor with band gaps of 3.28 eV (4H) and 3.03 eV (6H) respectively. The beta modification (β-SiC) is a face-centered cubic crystal structure (similar to diamond and zincblende or sphalerite). Until recently, the beta form has had relatively few commercial uses, although there is now increasing interest in its use as a support for heterogeneous catalysts, owing to its higher surface area compared to the alpha form [1.19]. There is currently much interest in its use as a semiconductor material in electronics, where its high thermal conductivity, high electric field breakdown strength and high maximum current density make it more promising than silicon for high-powered devices. In addition, it has strong coupling to microwave radiation, which together with its high melting point, permits practical use in heating and casting metals. SiC also has a very low coefficient of thermal expansion and experiences no phase transitions that would cause discontinuities in thermal expansion. Due to the rarity of natural moissanite, it is typically man-made. Purer silicon carbide can be made by the more expensive process of CVD.

References

[1.1] H. L. Tsai, T. Y. Wang, J. R. Yang, C. C. Chuo, J. T. Hsu, Z. C. Feng and M. Shiojiri, *Materials Transactions*, 48, 894-898 (2007).

[1.2] Z. C. Feng, J. H. Chen, A. G Li, and L. C. Chen, *J. Physics: Conf. Ser.*, 28, 42-47 (2006).

[1.3] J. H. Chen, Z. C. Feng, H. L. Tsai, J. R. Yang, P. Li, C. Wetzel, T. Detchprohm, and J. Nelson, *Thin Solid Films*, 498, 123-127 (2006).

[1.4] J. H. Chen, Z. C. Feng, J. C. Wang , H. L. Tsai, J. R. Yang, A. Parekh, E. Armour, and P. Faniano, *Journal of Crystal Growth*, 287, 354-358 (2006).

[1.5] Pécz B, di Forte-Poisson M A, Huet F, et al. *J. Appl. Phys.* 86, 6059-6067 (1999).

[1.6] KAMINSKA E, PIOTROWSKA A, BARCZ A, *Material Science and Engineering B*, 82, 265-267 (2001).

[1.7] H. Amano, M. Kito, K. Hiramatsu, I. Akasaki, *Japanese Journal of Applied Physics*, 28, L2112 (1989).

[1.8] S. Nakamura, M. Senoh, S. Hagahama, N. Iwasa, T. Yamada, T. Matsushita, Y. Sugimoto, and H. Kiyoku, *Appl. Phys. Lett.* 69, 3034 (1996).

[1.9] K. Itaya, M. Onomura, J. Nishio, L. Sugiura, S. Saito, M. Suzuki, J. Rennie, S.

Nunoue, M. Yamamato, H. Fujimoto, Y. Kokomot, Kokobun, Y. Ohba, G. Hatakoshi, and M. Ishikawa, *Jpn. J. Appl. Phys.*, 35, 11315 (1996).

[1.10] I. Akasaki, S. Sota, H. Sakai, T. Tanaka, M. Koike, and H. Amano, *Electron. Lett.* 32, 1105 (1996).

[1.11] G. F. Bulman, K. Doverspike, S. T. Sheppard, T. W. Weeks, H. S. Kong, H. M. Dieringer, J. A. Edmond, J. D. Brown, J. T. Swindell, and J. F. Schetzina, *Electron. Lett.* 33, 1556 (1997).

[1.12] M. P. Mack, A. Abare, M. Aizcorbe, P. Kozodov, S. Keller, U. K. Mishra, L. Coldren, and S. DenBaars, *MRS Internet J. Nitride Semicond. Res.* 2, 41 (1997).

[1.13] E. S. Jeon, V. Kozlov, Y. K. Song, A. Vertikov, M. Kuball, A. V. Nurmikko, H. Liu, C. Chen, R. S. Kern, C. P. Kuo, and M. G. Craford, *Appl. Phys. Lett.* 69, 4194 (1996).

[1.14] M. Pophristic, F. H. Long, C. Tran, I. T. Ferguson, and R. F. Karlicek, Jr., *J. Appl. Phys.* 86, 1114 (1999).

[1.15] Tsutomu Araki and Hiroaki Misawa, *Rev. Sci. Instrum.* 66, 5469 (1995).

[1.16] S. F. Chichibu, M. Sugiyama, T. Onuma, T. Kitamura, H. Nakanishi, T. Kuroda, A. Tackeuchi, T. Sota, Y. Ishida, and H. Okumura, *Appl. Phys. Lett.* 79, 4319 (2001).

[1.17] K. S. Ramaiah, Y. K. Su, S. J. Chang, B. Kerr, H. P. Liu, and I. G. Chen, *Appl. Phys. Lett.* 84, 3307 (2004).

[1.18] S. Nakashima and H. Harima, phys. stat. sol. (a) 162, 39 (1997).

[1.19] Goldberg Yu., Levinshtein M.E. and Rumyantsev S.L., "in Properties of Advanced SemiconductorMaterials GaN, AlN, SiC, BN, SiC, SiGe", Wiley, New York, (2001).

Chapter 2 Theoretical Background and Experimental Details

2.1 Introduction of Brillouin scattering spectroscopy

Brillouin scattering (BLS) is defined as inelastic scattering of light in a physical medium by thermally excited acoustical phonons. Prediction of the BLS became possible with the development of the theory of thermal fluctuations in condensed matter at the beginning of the 20th century. Brillouin scattering belongs to statistical phenomena, when scattering of the light occurs in a physical medium due to interaction of light with medium inhomogeneities. Such inhomogeneities can be thermal fluctuations of the density in the medium.

2.1.1 History

With the studies conducted by [2.1], it became obvious that the thermal fluctuations of density can be considered as a superposition of the acoustic waves (thermal phonons), propagating in all directions in condensed media. The first theoretical study of the light scattering by thermal phonons was done by Mandelstam in 1918, however, the correspondent paper was published only in 1926 [2.2]. Brillouin independently predicted light scattering from thermally excited acoustic waves gave experimental confirmation of such a prediction in liquids and crystals.

2.1.2 Spectrometer

In almost all Brillouin experiments, the Fabry-Perrot interferometer has been instrument of choice (Grimsditch, 2001). However, conventional Fabry Perot interferometers do not achieve the contrast needed to resolve the weak Brillouin doublets. Sandercock first showed that the contrast can be significantly improved by multipassing (Sandercock, Opt. Commun. 2 73-76 (1970). The usefulness of coupling two synchronized Fabry-Perot, thus avoiding the overlapping of different orders of interference, was also recognized .

2.1.3 Principles

The scattering in this case is mediated by the elasto-optic scattering mechanism, in which dynamic fluctuations in the strain field bring about fluctuations in the dielectric constant, and these in turn translate into fluctuations in the refractive index. These fluctuating optical inhomogeneities result in inelastic scattering of the light as it passes through the solid. The phonons present inside a solid move in thermal equilibrium with very small amplitudes creating fluctuations in the dielectric constant, which is viewed as a moving diffraction grating by an incident light wave. Therefore Brillouin scattering can be explained by the two concepts of Braggs reflection and Doppler shift. In the case of a transparent solid, most of the scattered light emanates from the refracted beam in a

region well away from the surface, and the kinematic conditions relating wave vector and frequency shift of the light pertain to bulk acoustic wave scattering.

2.1.4 Applications

The main application of Brillouin scattering is to measure elastic properties (acoustic velocities) of micron size samples. BLS is widely used in material sciences for measuring the elastic properties of submicron films and specimens [2.3]. The films and materials that have been studied to date are many and diverse, and include inorganic materials like silicon and silicides, superhard materials, C_{60}, cubic BN, cubic BC_2N, a variety of carbonaceous materials like diamond, CVD diamond and diamond-like films, various types of hard coatings like carbides and nitrides, Langmuir-Blodgett films, and various types of multilayers. SBS can probe acoustic waves of frequencies up to 100 GHz and characterize films of thickness as thin as a few tens of nanometers. BLS is one of the main tools in studying the elastic properties of Earth interior. Understanding of the elastic behavior of minerals under high pressure is a crucial factor for developing a model of the Earth's structure because most information about the Earth's interior comes mainly from seismological data. Brillouin scattering can be used for measuring elastic properties of transparent materials at pressures up to 172 GPa [2.4].

2.2 Photoluminescence (PL)

Photoluminescence is the optical emission obtained by photon excitation (usually a laser) and is commonly observed with III-V semiconductor materials. This type of analysis allows non-destructive characterization of semiconductors (material composition, qualitative investigations, etc.). For a perfect semiconductor crystal, a light source with photon energy higher than the band gap of the semiconductor crystal will excite the carriers to excited states. As soon as the excitation occurs, all excited electrons and holes will relax to the bottom of the conduction band and the top of valence band, respectively, and then the radiative recombination may occur under the condition of momentum conservation as shown in figure 2.1. When the maximum of the valence band and the minimum of the conduction band occur at the same value of the wave vector **k**, transitions are direct and the material is a direct-gap semiconductor (for instance, GaAs and GaN). For a direct-gap material, the most probable transition is across the minimum energy gap which is between the most probably filled states at the minimum of the conduction band and the states most likely to be unoccupied at the maximum of the valence band. If the band extreme do not occur at the same wave vector **k**, the transition is indirect. Light is directed onto a sample, where it is absorbed and imparts excess energy into the material in a process called photo-excitation. One way this excess energy can be dissipated by the sample is through the emission of light,

or luminescence. In this case of photo-excitation, this luminescence is called photoluminescence.

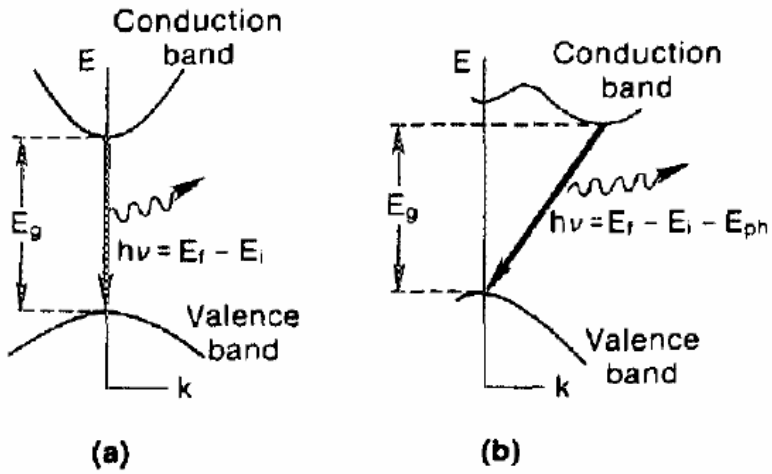

Figure 2.1 *Energy transitions in (a) direct and (b) indirect gap semiconductors between initial states E_i and final states E_f. For indirect transitions, the participation of a phonon (E_{ph}) is required.*

As shown in figure 2.2, for example, if there is a multiplicity of excited states, only transitions from the lowest excited state can generally be observed at low temperatures because of rapid thermalization [2.5]. Impurities or defects in structure responsible for the emissions are termed as “activators”. Because impurities can be either the energy levels of the impurity ion perturbed by the crystal field or the band structure of the crystal disturbed by the impurity, so the electronic states involved in the luminescence.

Other imperfections that are necessary for the luminescence but have little influence on the spectral distribution of emission are called “co-activators” [2.6].

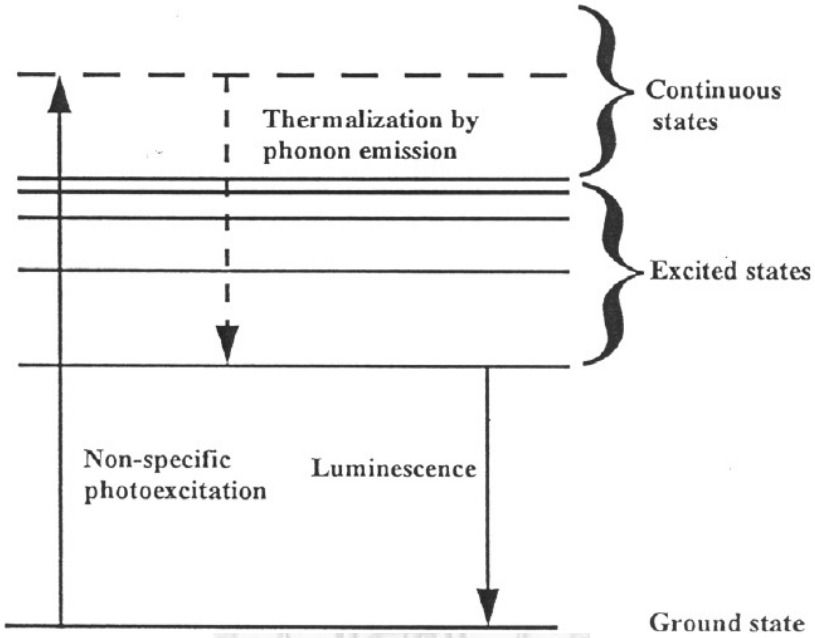

Figure 2.2 *the schematic representation of low temperature photoluminescence (after R. A. Strading and P. C. Klipstein).*

PL is one of the most useful optical methods for the semiconductor industry, with its powerful and sensitive ability to find impurities and defect levels in silicon and group III-V element semiconductors, which affect materials quality and device performance. The intensity and spectral content of this photoluminescence is a direct measure of various important material properties. In another use, the full width at half maximum (FWHM) of PL peak is an indication of sample quality and crystallinity, although such analysis has not yet become highly quantitative. Photoluminescence can

also determine the band gaps of semiconductors. This is very important for binary (A_xB_{1-x}) and ternary ($A_xB_{1-x}C$) alloys whose gaps vary with the compositional parameter x which must be accurately known for applications.

2.3 Raman Scattering (RS)

Raman spectroscopy is a convenient technique for characterizing semiconductors. It is in principle non-destructive, contactless, and requires no special sample preparation technique such as thinning or polishing. It is a standard optical characterization technique for studying various aspects of solids such as lattice, electronic and magnetic properties.

It is possible that an excited atom will not return to its initial state after the emission of a photon. This kind of behavior had been observed and studied extensively by Sir G. G. Stokes [2.7] prior to the advent of quantum theory. If a monochromatic light is scattered from a substance, it will thereafter consist mainly of light of the same frequency. Yet it is possible to observe very weak additional components having higher and lower frequencies (side band). Moreover, the difference between the side bands and the incident frequency ϖ is found to be characteristic of the material and therefore suggests an application to spectroscopy. This effect was predicted in 1923 by Adolf Smekal [2.8], theoretically described by Kramers and Heisenberg (1925), Schrödinger (1926), Dirac (1927) [2.9] and for the first time experimentally identified by the Indian

physicist, Sir Chandrasekhara Vankata Raman [2.10] in 1928. It was found that the light scattered by liquids such as benzene contains sharp sidebands in pairs symmetrically disposed around the incident frequency with shifts identical to the frequencies of some of the infrared vibrational lines. At much the same time in Moscow, Landsberg and Mandelstam (1928) [2.11] independently found this phenomenon in quartz. This inelastic scattering of light by molecular and crystal vibrations is now known as the Raman effect. It is caused by modulation of the susceptibility (or, equivalently, polarizability) of the medium by the vibrations. The vibrational Raman effect was well documented and well understood by Placzek (1934) [2.12].

To appreciate how the phenomenon operates, we could utilize the germane features of molecular spectra. A molecule can absorb radiant energy in the far-infrared and microwave regions, converting it to rotational kinetic energy. Furthermore, it can absorb infrared photons, transforming that energy into vibrational motion of the molecule. Finally, a molecule can absorb energy in the visible and ultraviolet regions through the mechanism of electron transitions. Suppose that we have a molecule in some vibrational state, which, using quantum-mechanical notation,

2.4 Time-Resolved Photoluminescence: TRPL

Time-resolved photo- luminescence (TRPL) is a powerful experimental tool to study the carrier dynamic processes in materials. By using Time-Resolved Photo-

luminescence (TRPL) can find out about life time of carrier, and distinguish fluorescence different physics mechanisms, more spectral and temporal information, can even receive the information of the molecule layers, all these results are not able to get by the photoluminescence spectrum.

There are a lot of methods to examine life time, for example: Phase-Sensitive detection, Time-resolved analog detection and Streak camera setection , etc.. The examine methods mentioned above need to use pulse laser diode to excite the sample, and basically the resolution of time is limited by the width of pulse laser wave.

When CW excitation is used in a PL experiment, the system quickly converges on steady state. The rate of excitation equals the rate of recombination, and the photogenerated carrier density is constant in time. In contrast, when a material is excited by a series of short laser pulses, the concentration of carriers depends strongly on time. Because the laser pulse can be much shorter than the average recombination time, a specific carrier density can be generated almost instantaneously. The photoexcited carriers then recombine at a rate that is characteristic of the recombination path they follow. Time-resolved PL measurements can be used to determine carrier lifetimes, and to identify and characterize various recombination mechanisms in the material. For instance, consider a semiconductor which has two process of recombination, PL measurement can not resolve the emission from the steady-state data because of spectra

overlap of emission. Photogenerated carrier lifetimes are obtained by monitoring the transient PL signal after pulsed excitation. Although the experimental apparatus required to make such a measurement depends on the desired resolution, the most common detection scheme is time-correlated single photon counting (TCSPC). When a photon is incident on a photodetector, an electrical pulse is generated. This pulse and an excitation reference pulse are fed into a constant fraction discriminator, which is designed to create output pulses that are timed correctly independent of input pulse size. Next, the signal and reference pulses are sent to a time-to-amplitude converter. Time-resolved measurements may reveal two decay times, which can be used to resolve the emission spectra and relative intensities of the two process of recombination. The output pulses are sorted according to amplitude and counted by a multichannel analyzer, yielding the transient PL decay.

Before further discussion of lifetime measurements, it is important to have a firm understanding of the meaning of the lifetime τ. Example a sample is excited with an infinitely sharp （δ function） pulse laser. This results in an initial population n_0 of carriers in the excited state. The excited-state population decays with a rate $\Gamma + k_{nr}$ according to

$$\frac{dn(t)}{dt} - (\Gamma + k_{nr})n(t) \tag{2-1}$$

where n(t) is the number of excited carriers at time t following excitation, Γ is the

emissive rate, and nr k is the nonradiative decay rate. Emission is a random event, and each excited carriers have the same probability of emitting in a given period of time. This result in an exponential decay of the excited-state population,

$$n(t) = n_0 \exp^{-t/\tau} \tag{2-2}$$

In a PL experiment we do not observe the number of excited carriers, but rather PL intensity, which proportional to n(t). Hence, equation (2-4) can also be written in terms of the time-dependent intensity I(t). Integration of equation (2-4) yield the usual expression for a single exponential decay

$$I(t) = I_0 \exp^{-t/\tau} \tag{2-3}$$

where I_0 is the intensity at time zero. The inverse of $\tau_{PL}(T)$ is the sum of three different types of transition probability,

$$\frac{1}{\tau_{PL}(T)} = \frac{1}{\tau_{rad}(T)} + \frac{1}{\tau_{non-rad}(T)} + \frac{1}{\tau_{trans}(T)} \tag{2-4}$$

Where $\tau_{rad}(T)$ and $\tau_{non-rad}(T)$ denote the radiative and non-radiative lifetimes, and $\tau_{trans}(T)$ is the transfer time toward lower-lying energy levels. If radiative recombination occurs at the bottom of energy levels, the term of the transfer time can be neglected so that the equation is simplified as shown below.

$$\frac{1}{\tau_{PL}(T)} = \frac{1}{\tau_{rad}(T)} + \frac{1}{\tau_{non-rad}(T)} \tag{2-5}$$

PL time-resolved measurement was performed using the technique of Time-Correlated Single Photon Counting (TCSPC). With a periodic excitation (e.g. from a laser) it is possible to extend the data collection over multiple cycles, one can reconstruct the single cycle decay profile from single photon events collected over many cycles. The method is based on the repetitive, precisely timed registration of single photons of e.g. a fluorescence signal. The reference for the timing is the corresponding excitation pulse. As a single photon sensitive detector a Photomultiplier Tube (PMT) or a Single Photon Avalanche Photodiode (SPAD) can be used. Provided that the probability of registering more than one photon per cycle is low, the histogram of photon arrivals per time bin represents the time decay one would have obtained from a single shot time-resolved analog recording. The precondition of single photon probability can be met by simply attenuating the light level at the sample if necessary. If the single photon probability condition is met, there will actually be no photons at all in many cycles.

Reference

[2.1] Smoluchovskii, Einstein and Debye, W. Hayes, R. Loudon, Scattering of Light by Crystals (1978)

[2.2] Mandelstam, Zh. Russ. Fiz-Khim. Ova., 58, 381 (1926)

[2.3] Beghi, Every, Zinin, in T. Kundu ed., Ultrasonic Nondestructive Evaluation: Engineering and Biological Material Characterization, chpt. 10, 581, (2003)

[2.4] http://www.soest.hawaii.edu/~zinin/Zi-Brillouin.html

[2.5] R. A. Stradling and P. C. Klipstein, in Growth and Characterisation of Semiconductors (Hilger, 1990).

[2.6] Department of Physics National Taiwan University, Optical and Electrical Properties of Type-II GaAsSb/GaAs Multiple Quantum Wells, Tzung Te Chen.

[2.7] Timothy H. Gfroerer, "Photoluminescence in Analysis of Surfaces and Interfaces", Ó John Wiley & Sons Ltd, Chichester, 2000, pp. 9209–9231.

[2.8] Lee, Zhen-Sheng, "Optical Properties of InGaN/GaN Multi-Quantum Wells Structure Grown by Metalorganic Chemical Vapor Deposition", Graduate Institute of Photonics and Optoelectronics, National Taiwan University, Master Thesis (2007).

[2.9] Huang, Yi-Zhe, "Optical Measurements and Analyses of InGaN/GaN on ZnO and Field Emission Studies of Carbon Nanotubes", Graduate Institute of Photonics and Optoelectronics, National Taiwan University, Master Thesis (2008).

[2.10] Rothen et al., Ellipsometry in the Measurement of Surfaces and Thin Films, Washington, DC: U.S. Government Printing Office, Nati. Bur. Stand. Misc. PubI. 256 (1964).

[2.11] N. M. Bashara, A. B. Buckman, and A. C. Hall (eds.), Proceedings of the Symposium on Recent Developments in Ellipsometiy, Amsterdam: North Holland (1969).

[2.12] N. M. Bashara and R. M. A. Azzam (eds.), Ellipsometiy, Proceedings of the Third International Conference on Ellipsometiy, Amsterdam: North Holland (1976).

Chapter 3 Brillouin scattering and the other material studies of GaN, InGaN, and AlGaN

3.1 InGaN/GaN Heterostructure Grown on Sapphire Substrate by Metalorganic Chemical Vapor Deposition

3.1.1 Introduction

GaN and its ternary alloys InGaN and are the main materials for the bluegreen light-emitting optoelectronic and other electronic devices. GaN-based Light Emitting Diodes (LEDs) are now commercially available and marvelous progress has been made in recent years [3.1-3.3]. Metalorganic Chemical Vapor Deposition (MOCVD) technology has been widely employed in research and industry production for these GaN-based optoelectronic and electronic materials and devices currently. However, many technological and scientific barriers still exist in this materials system. The most dominant ones are stoichiometric nitrogen incorporation, p-type doping, and the availability of lattice and thermally-matched substrates. Due to the use of large amounts of various organic and inorganic gases in the chemical reaction chamber, the surface chemical states of grown materials are affected by many factors. It has been found that the composition and structure of III-V nitride films strongly influence their optoelectronic properties. Doping can also change the strength of light emitted. The fabricated semiconductor devices are sensitive to surface properties.

InGaN is the main material of blue-violet light, and its lattice mismatch with GaN can cause a strong piezoelectric effect, which would affect the white LED emissions. The lattice mismatch and different thermal stability of the two constituents, InN and GaN, also complicate the growth of $In_xGa_{1-x}N$. The lattice mismatch also can lead to a miscibility gap, which causes fluctuations of In content across the film. But many fundamental properties of InGaN, such as elastic constants etc, are lacking research. For the case of GaN, there exists only few reports [3.4,3.5] using Brillouin scattering to get its elastic constants, which are not very reliable, to our opinion. This work is performing a Brillouin scattering study on an InGaN/GaN on sapphire, to calculate the phonon velocity and deduce the elastic constants of InGaN with ~2% In. Analytical techniques of photoluminescence (PL), optical transmission (OT), have been employed to investigate their optical and properties.

3.1.2 Experimental

The sample 1940i, 1947i, and 1935i of InGaN/GaN was grown on sapphire by metal organic chemical vapor deposition (MOCVD). Ihe indium contents are ~2%, 15%, and 29%, respectively. An argon ion laser (λ＝514.5 nm) with 80–100 mW of power and a six-pass tandem Fabry–Pe´rot interferometer were used for the Brillouin measurements on AlGaN/sapphire. And an laser (λ＝532 nm) was used for GaN on sapphire measurements. Our Brillouin experiment utilizes a 60°/60° symmetric

scattering geometry, which yields acoustic velocity measurements independent of the refractive index of the specimen and the Brillouin frequency shift Δω is directly related to the acoustic velocity V and the incident laser wavelength λ. Details of the Brillouin scattering technique have been widely elucidated in the literature, e.g. [3.6,3.7]. The birefringence of non-isotropic crystals can be problematic, because birefringence can yield double peaks or cause peak broadening in the Brillouin spectrum. However, this case has not been a trouble because double peaks and appreciable broadening were not observed in our samples. In this work, Brillouin scattering measurements of InGaN/GaN on sapphire and GaN on sapphire with angular variations over 0 to 180 degrees with interval of 15 degrees.

3.1.3 Result and discussion

3.1.3.1 Brillouin scattering

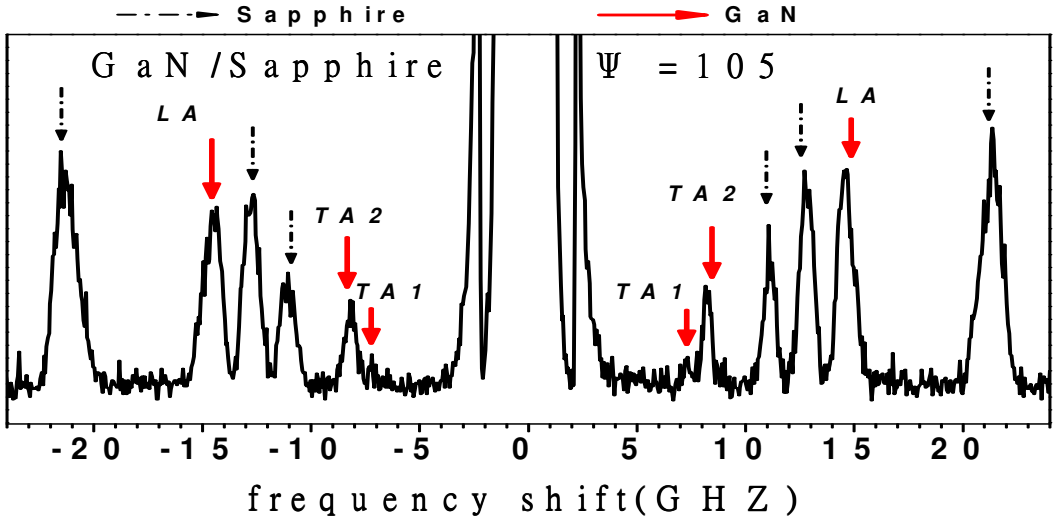

Figure 3.1 *Representative Brillouin spectra of GaN on sapphire at Ψ=105°*

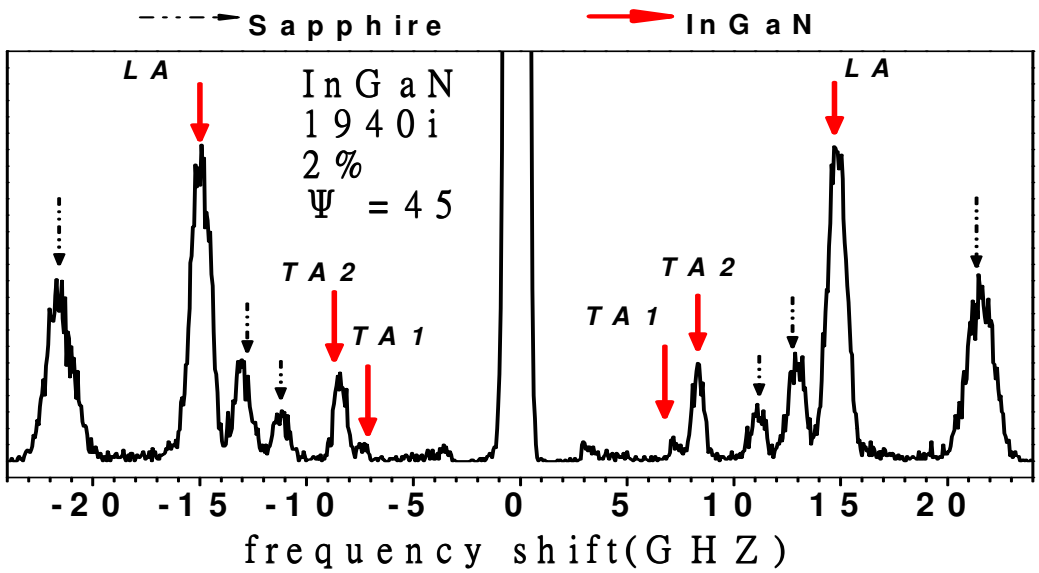

Figure 3.2 *Representative Brillouin spectra of $In_{0.02}Ga_{0.98}N$ on sapphire at Ψ=45°*

Figure 3.1 showed the Brillouin frequency shifts of GaN and sapphire. We obtained the TA (transverse acoustics)1, TA2, and LA (longitudinal acoustics) frequency shifts at 7.494, 8.201, and 14.564 (GHZ) of GaN. Besides, figure 3.2 showed TA1, TA2, and LA frequency shifts of $In_{0.02}Ga_{0.98}N$ at 7.314, 8.371, and 14.925 (GHZ), respectively. In.Our Brillouin experiment utilizes a symmetric scattering geometry with an external angle between the incident and scattered beams of 60° as figure 3.3 showed. We computed the θ = 12.23° by Snell's law, and 2.36 is use for refractive index of GaN [3.8]. These acquisition enabled us to calculate the velocity (V) of each acoustic mode according to the equation：

$$V=\lambda\Delta\omega/(2n\sin\theta) \qquad (3.1)$$

where n, Δω, and λ are the refractive index of sample, the Brillouin frequency shift, and

the wavelength of laser, respectively.

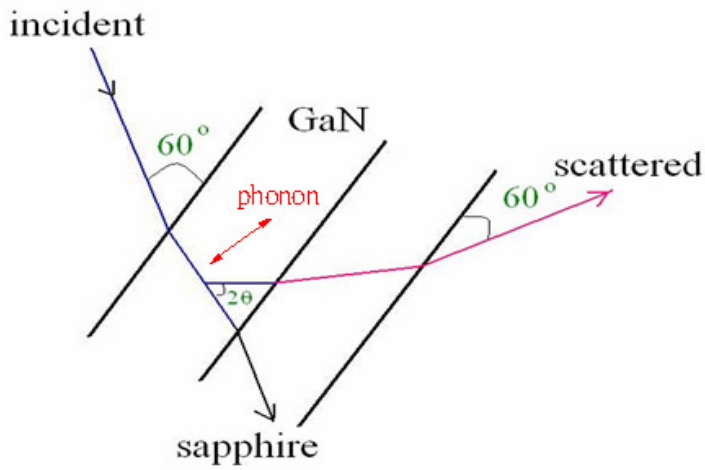

Figure 3.3 *Sketch of the incident light and scattered light*

Table 3.1 list the Brillouin frequency shifts and acoustic velocities were calculated by equation (3.1). For $In_{0.02}Ga_{0.98}N$, we do the same treatments and list them in table 3.2

Ψ (chi)	Δω(LA) GHZ	Δω(TA2) GHZ	Δω(TA1) GHZ	V(LA) km/sec	V(TA2) km/sec	V(TA1) km/sec
0	14.555	8.197	7.269	7.743	4.361	3.867
15	14.560	8.186	7.179	7.746	4.355	3.819
30	14.566	8.177	7.118	7.749	4.350	3.787
45	14.568	8.173	7.103	7.750	4.348	3.779
60	14.564	8.179	7.137	7.748	4.351	3.797
75	14.555	8.182	7.173	7.743	4.353	3.816
90	14.513	8.175	7.252	7.721	4.349	3.858
105	14.564	8.201	7.494	7.748	4.363	3.987
120	14.543	8.216	7.289	7.737	4.371	3.878
135	14.571	8.226	7.250	7.752	4.376	3.857
150	14.568	8.158	7.474	7.750	4.340	3.976
165	14.532	8.263	7.259	7.731	4.396	3.862
180	14.596	8.248	7.231	7.765	4.388	3.847

Table 3.1 *Brillouin frequency shifts (Δω) and acoustic velocities of GaN*

Ψ (chi)	Δω(LA) GHZ	Δω(TA2) GHZ	Δω(TA1) GHZ	V(LA) km/sec	V(TA2) km/sec	V(TA1) km/sec
0	14.832	8.309	7.345	7.631	4.275	3.779
15	14.847	8.344	7.392	7.639	4.293	3.803
30	14.861	8.365	7.347	7.646	4.304	3.780
45	14.925	8.371	7.314	7.674	4.307	3.763
60	14.851	8.362	7.318	7.641	4.302	3.765
75	14.933	8.391	7.384	7.683	4.317	3.799
90	14.913	8.441	7.345	7.714	4.343	3.779
105	15.007	8.455	7.361	7.721	4.350	3.787
120	15.166	8.509	7.477	7.803	4.378	3.843
135	15.180	8.511	7.524	7.818	4.379	3.871
150	15.217	8.550	7.520	7.829	4.399	3.869
165	15.153	8.525	7.541	7.796	4.382	3.880
180	15.149	8.531	7.528	7.794	4.389	3.873

Table 3.2 *Brillouin frequency shifts (Δω) and acoustic velocities of* $In_{0.02}Ga_{0.98}N$

According to the Christoffel's equation, the elastic constants relate to the velocities of ultrasonic waves in an anisotropic solid as [3.9] :

$$[\Gamma_{ij} - \delta_{ij}\rho V^2][P_m] = 0 \tag{3.2}$$

Where Γ_{ij} is the Christiffel's tensor and $\Gamma_{ij} = C_{ij}n_in_j$. C_{ij} is the stiffness tensor, n_i and n_j are the direction cosines, δ_{ij} is the Kronecker tensor, ρ is the mass density (6.087g/cm^3 is used for ρ of GaN, 6.101g/cm^3 is used for ρ of $In_{0.02}Ga_{0.98}N$ [3.10]). P_m is the polarization vector.

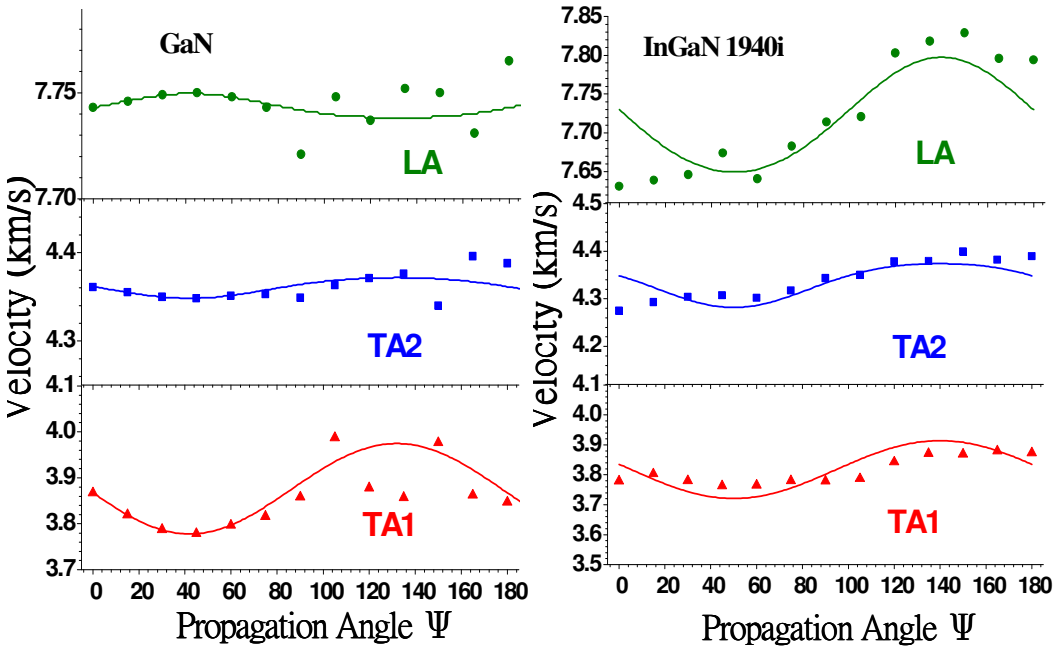

Figure 3.4(a) *Acoustic velocities versus Ψ angle of GaN*

(b) *Acoustic velocities versus Ψ angle of* $In_{0.02}GaN_{0.98}$ *1940i*

Figure 3.4(a) shows the variation of TA1, TA2 and LA phonon waves velocity of GaN with propagation angle Ψ, while figure 3.4(b) are those of InGaN with In comcentrations~2%. In Figure 3.4, the solid dots are our data, and the solid curves are the fitting results. The velocities of acoustics waves of GaN and $In_{0.02}Ga_{0.98}N$ are similar, because the In composition of InGaN 1940i is very weak. We put all the datum and fitting results in figure 3.5 to compare easier. There is just a little difference in two samples. The LA velocity of $In_{0.02}Ga_{0.98}N$ is a little lower than the LA velocity of GaN.

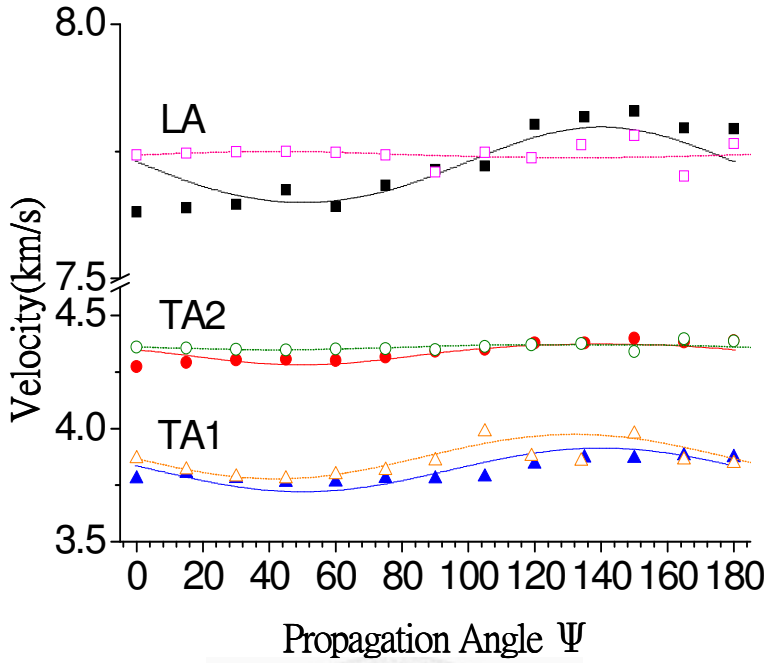

Figure 3.5 *Acoustic velocities versus Ψ angle of GaN (dash lines and dash dots) and*

$In_{0.02}GaN_{0.98}$ (solid lines and solid dots)

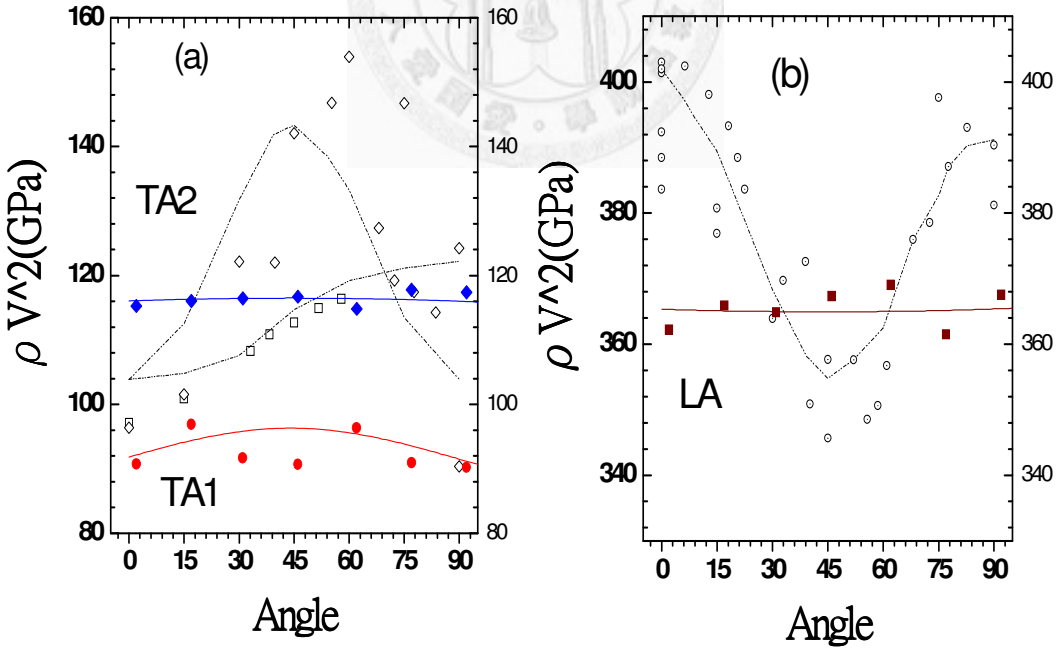

Figure 3.6 *Product of density times velocity squared*

versus propagation angle about GaN

In figure 3.6, the solid dots are our GaN experimental datum, and the solid lines are the fitting results. On the contrary, the dash dots and dash lines are the datum and their fitting results of reference [3.4] respectively. Accordingly, the elastic constants Cijs were listed in table 3.3. In hexagonal system, only C_{11}, C_{33}, C_{44}, C_{66}, C_{12}, C_{13} have non-zero values ($C_{66}=(C_{11}-C_{12})/2$). Using the measured elastic moduli, it is easy to compute the bulk modulus. In a hexagonal lattice, the bulk modulus is related to the elastic constants by this equation

$$B_0=(C_{11}+C_{22})C_{33}-2C^2_{13}/(C_{11}+C_{12}+2C_{33}-4C_{13}) \quad (3.3)$$

C_{ij}	C_{11}	C_{33}	C_{44}	C_{66}	C_{12}	C_{13}
GaN[3.4]	***390***	***398***	***105***	***123***	***145***	***106***
GaN[3.5]	***365***	***381***	***109***	***115***	***135***	***114***
GaN	***365.68***	***366.5***	***115.14***	***86.88***	***191.91***	***132.52***
$In_{0.02}Ga_{0.98}N$	***356.65***	***413.88***	***111.71***	***84.38***	***187.88***	***149.61***

Table 3.3 *Elastic constant of GaN from [3.4,3.5] , fitting, and* $In_{0.02}Ga_{0.98}N$

Brillouin scattering experiments also have measured on $In_{0.15}Ga_{0.85}N$ (1947i) and $In_{0.29}Ga_{0.71}N$ (1935i). Because the time to do the experiments in institute of earth science, Academia Sinica, is not enough, the Brillouin scattering spectra just measured for one propagation angle. We hope to keep in measuring in the future.

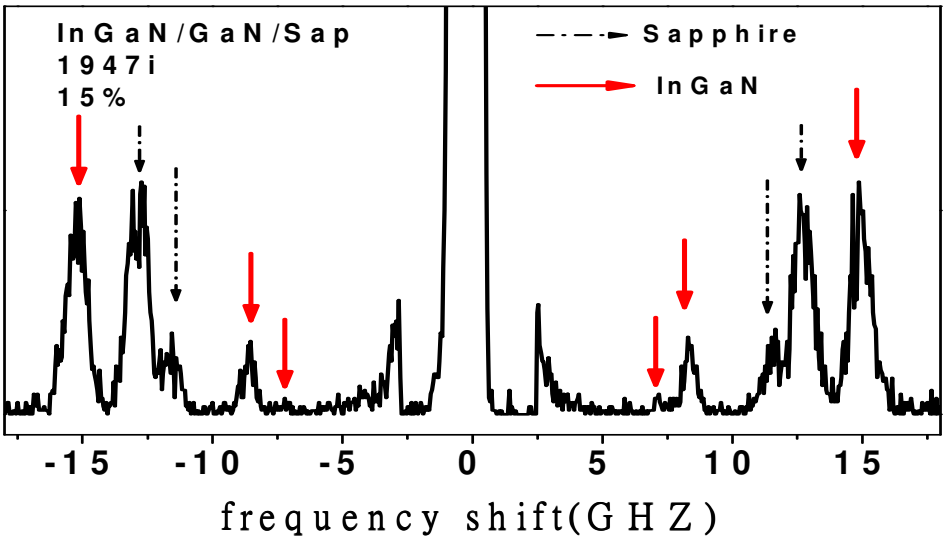

Figure 3.7 *Representative Brillouin spectra of $In_{0.15}Ga_{0.85}N$ on sapphire at $\Psi=0°$*

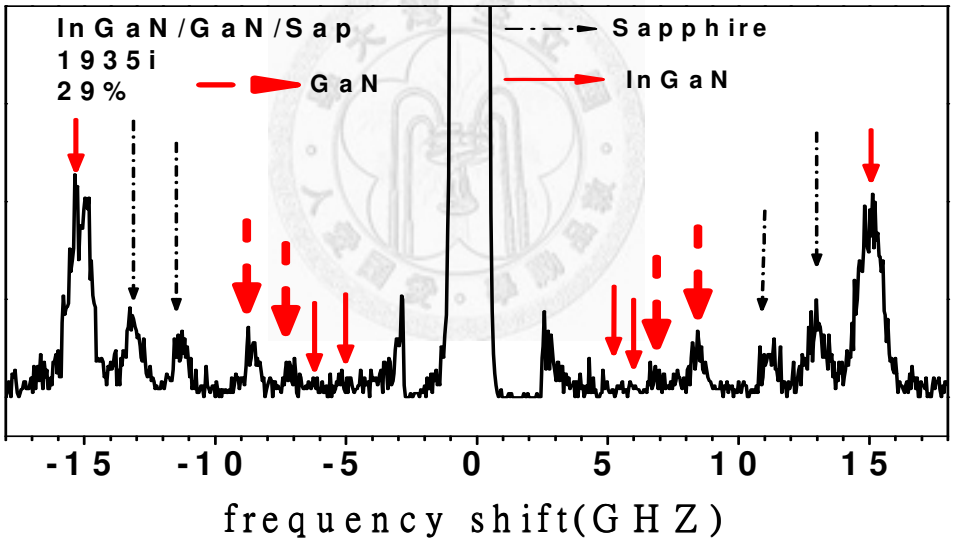

Figure 3.8 *Representative Brillouin spectra of $In_{0.29}Ga_{0.71}N$ on sapphire at $\Psi=0°$*

3.1.3.2 Photoluminescence (PL)

The PL measurement was carried out at room temperature using a 325 nm He-Cd laser. Figure 3.9 shows the room temperature photoluminescence spectra of three $In_xGa_{1-x}N$/GaN samples, 1940i, 1947i, and1935i, whose composition are x=2%, 15%,

29%. From the spectra, emission peaks were observed at 3.34eV, 3.02eV, and 2.68eV, which are due to the InGaN band edge emission. The PL peak energy shifted to low energy side due to the increase of the indium concentration. Only in the spectrum of $In_{0.02}Ga_{0.98}N$ (1940i), the emission paek of GaN at 3.42 eV appeared. The calculation was performed assuming that the InGaN band gap energy depends on the indium composition as $E_g^{InGaN}(x) = E_g^{InN}x + E_g^{GaN}(1-x) - bx(1-x)$ (eV), where b(x) is the variable bowing parameter, which depends on x [3.11, 3.12].

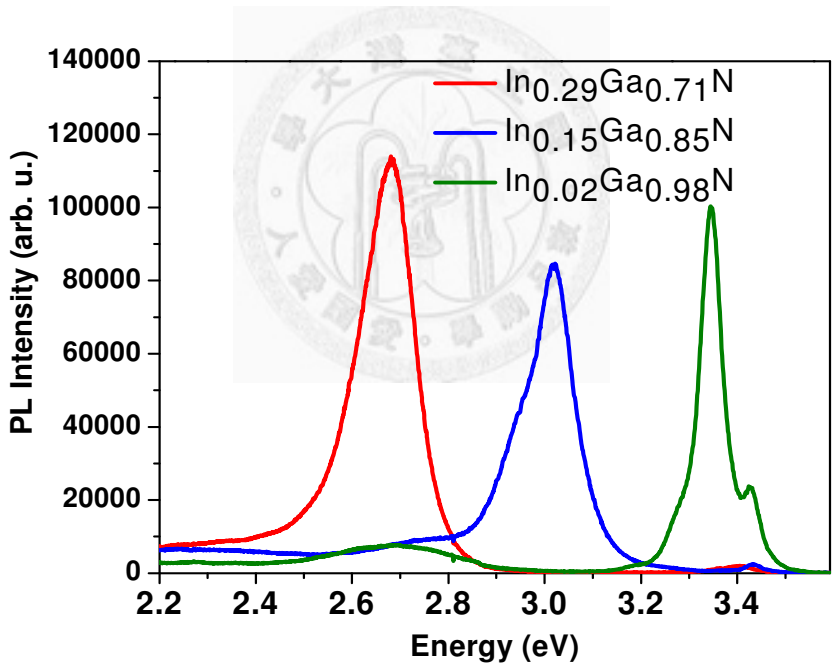

Figure 3.9 *PL spectra of $In_xGa_{1-x}N$ on sapphire*

3.1.3.3 Optical transmission (OT)

Shown in figure 3.10 is the transmittance spectrum of the sample $In_{0.02}Ga_{0.98}N$ (1940i), which was taken in the range of 200–1100nm using a cleaned sapphire

substrate as a reference. The variation of α^2 (α is the absorption coefficient) for direct band-gap semiconductors can be estimated from the equation

$$(\alpha h\nu)^2 = B(h\nu - E_g) \tag{3.4}$$

hν (hν is photon energy)where B is a proportional constant and Eg is the optical band-gap. Figure exhibits an optical transmittance of 82% in the visible range and a sharp fundamental absorption edge. Thus the band gap can be evaluated by drawing a solid line from the point of maximum gradient in the absorption curve and extrapolating the solid line to the wavelength axis. In this way, the optical band-gap of our sample is estimated to be 360 nm (3.44 ev).

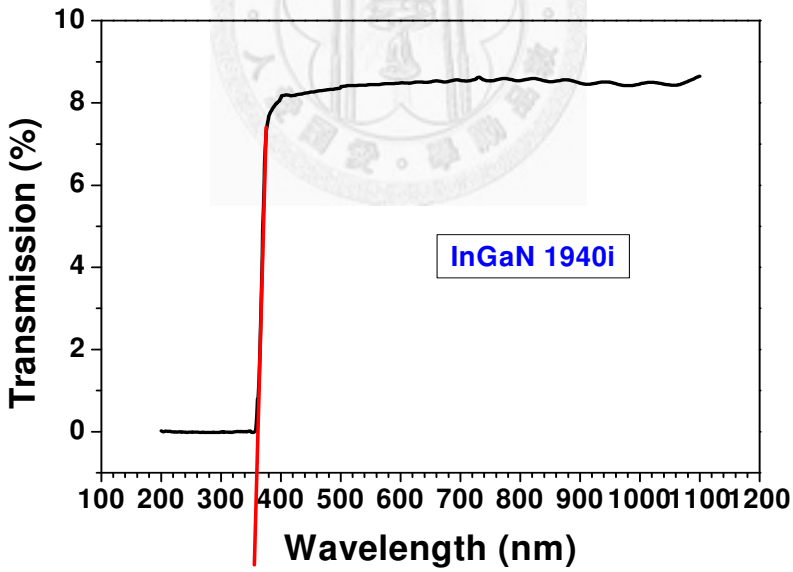

Figure 3.10 *Optical transmittance of $In_{0.02}Ga_{0.98}N$ (1940i)*

3.1.4. Summary

We investigated InGaN/GaN on sapphire thin films on the structural and optical

properties include Brillouin scattering, PL, and Optical Transmission results. The addition of indium in GaN has changed the energy gap then we obtained the emission peak shift in PL spectrum. Through Brillouin scattering measurements to compute the elastic constants. The rise or drop of elastic constants showed how the strain effect the elastic property.

3.2 AlGaN Grown on Sapphire Substrate by Metalorganic Chemical Vapor Deposition

3.2.1 Introduction

AlN, GaN, and their alloys are piezoelectric III–V nitride-based semiconductors suitable for optoelectronic devices as well as high-power, high-temperature transistor and surface acoustic wave (SAW) applications. In particular, ultraviolet laser diodes (UV LDs) using Al-doped GaN-based materials have been very attractive [3.13,3.14]. Al-doped GaN with 20-60% Al concentration is the dominant material for ultraviolet (UV) and deep UV laser diodes.

There always exist uniform or nonuniform strain in heterostructures whichmaymainly originate from lattice mismatch and different thermal expansion coefficients between the epilayer and substrate. The lattice mismatch can cause a strong piezoelectric effect, which may affect the LD emissions. However, up to now, no

established physical mechanism could be pinpointed to explain the features in the mosaic structure of III-nitride heterostructures, which has considerably postponed progress in this field of research. In order to solve this problem, a detailed study of the influence of the deformation state must be performed on the structural and electrical properties of multilayered nitride heterostructures and their mosaic structure and on defects caused by elastic strain relaxation processes. Many fundamental properties, such as elastic constants etc, have received less attention. However, the Brillouin scattering measurements of Al-doped GaN has never been conducted. In this work, we carried out a Brillouin experiment to understand the effect of Al on the elastic properties of GaN. And investigated the structural and optical properties by x-ray diffraction (XRD), and Raman scattering.

3.2.2 Experimental

In this work, all samples were divided two sets and they were grown by Metalorganic Chemical Vapor Deposition (MOCVD) in an EMCORE D180 short jar system on (0001) on sapphire. Trimethylgallium (TMGa), trimethylaluminium (TMAl) and NH_3 were used as the source precursors for Ga, Al, and N, respectively.

The first set：AlGaN epilayers were grown on sapphire by MOCVD. TMGa, TMAl, and NH_3 were used as the source precursors for Ga, Al and N, respectively. The epilayers were grown on sapphire (0001) substrate with an intermediate growth of

low-temperature AlN nucleation layer at 600 °C followed by a high temperature AlN nucleation layer at 1075 °C. In order to improve the surface morphology and the film quality, variable flow rates of trimethylindium (TMIn) were introduced during the growth for the incorporation of indium. Figure 3.11 shows the sample structure of (a) M1216, (b) M1170, and (c) M1686, respectively.

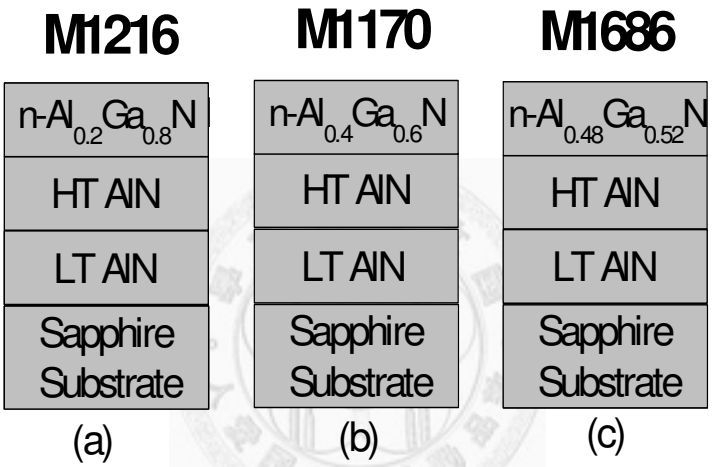

Figure 3.11 *Schematic Structures of the samples (a) M1216, (b) M1170, and (c) M1686*

The second set：A 25 nm low-temperature (590 ^{0}C at 300 Torr) AlN nucleation layer was used for AlGaN epilayers. $Al_{0.62}Ga_{0.38}N$ with lower aluminum (Al) composition (M1052) was grown at 1080 ^{0}C on low-temperature AlN nucleation layers with a V/III ratio of 4000 and a growth rate of 0.3μm/h. Figure 3.12 shows the schematic drawing of the sample M1052. In-situ reflectometry was used to monitor the growth rate and the surface morphology.

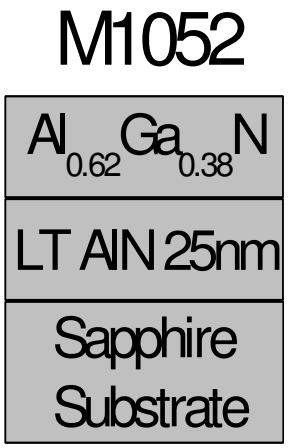

Figure 3.12 *Schematic Structures of the samples M1052*

Brillouin scattering spectra were collected for the Brillouin frequency of AlGaN samples. An argon ion laser (λ＝514.5 nm) with 80–100 mW of power and a six-pass tandem Fabry–Pe´rot interferometer were used for the Brillouin measurements. The specimens were mounted on a goniometer head of an Eulerian cradle, which was used to control the orientation of sample. The direction of phonon in specimen was changed by rotate the cradle. Brillouin scattering measurements of AlGaN on sapphire with angular variations over 0-180-degree with interval of 15-degree. A 60°/60° symmetric scattering geometry was adopted to collect the spectrum. The single refractive index was assumed for sapphire and our samples due to their trivial birefringence.

3.2.3 Result and discussion

3.2.3.1 Brillouin scattering

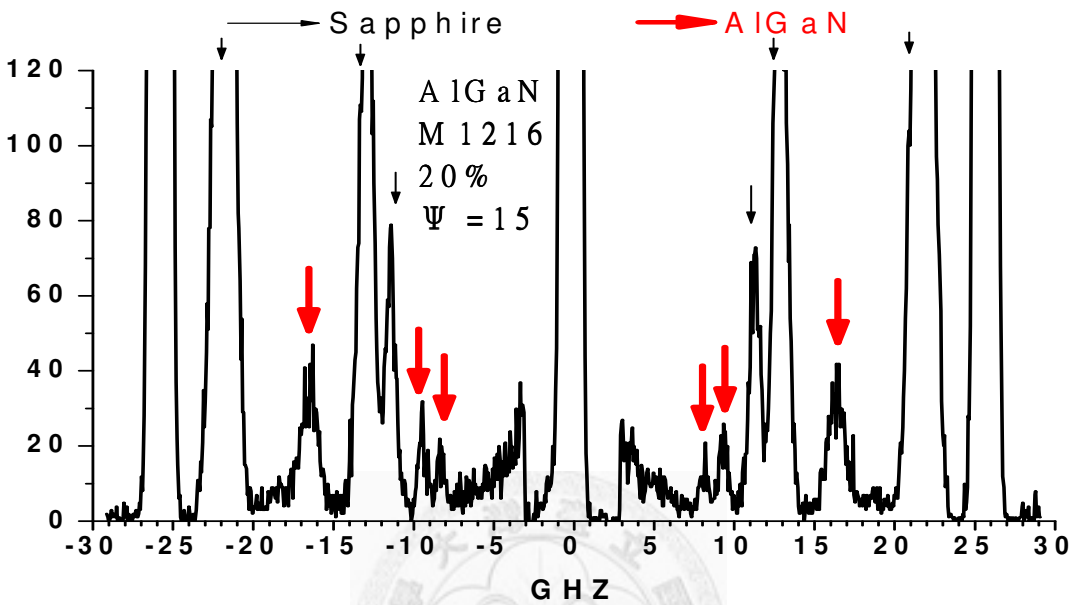

Figure 3.13 *Representative Brillouin spectra of $Al_{0.2}Ga_{0.8}N$ on sapphire at $\Psi=15°$*

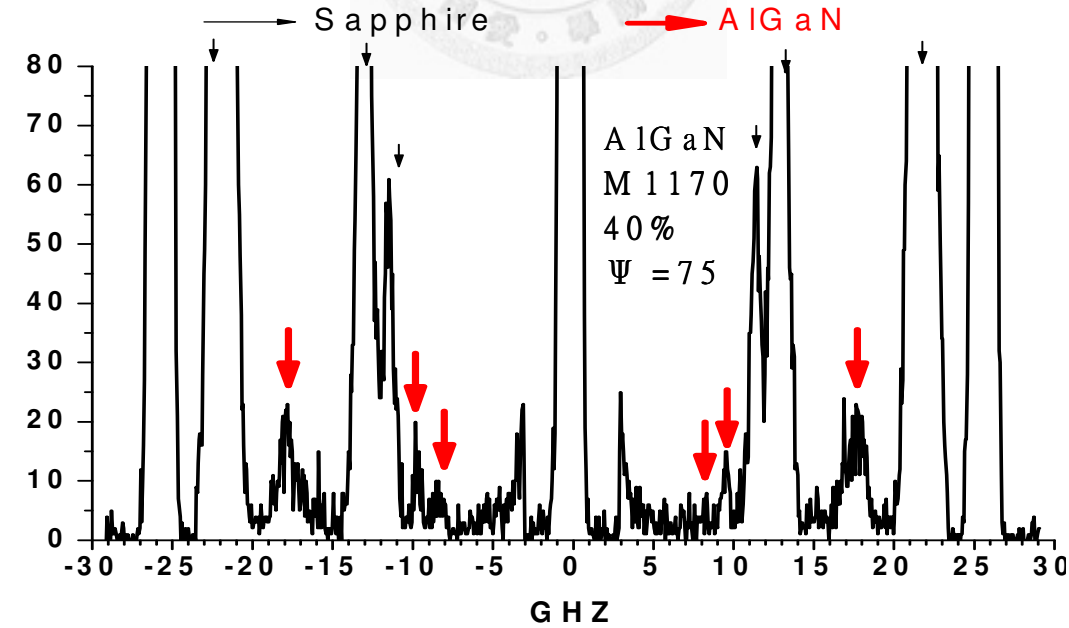

Figure 3.14 *Representative Brillouin spectra of $Al_{0.4}Ga_{0.6}N$ on sapphire at $\Psi=75°$*

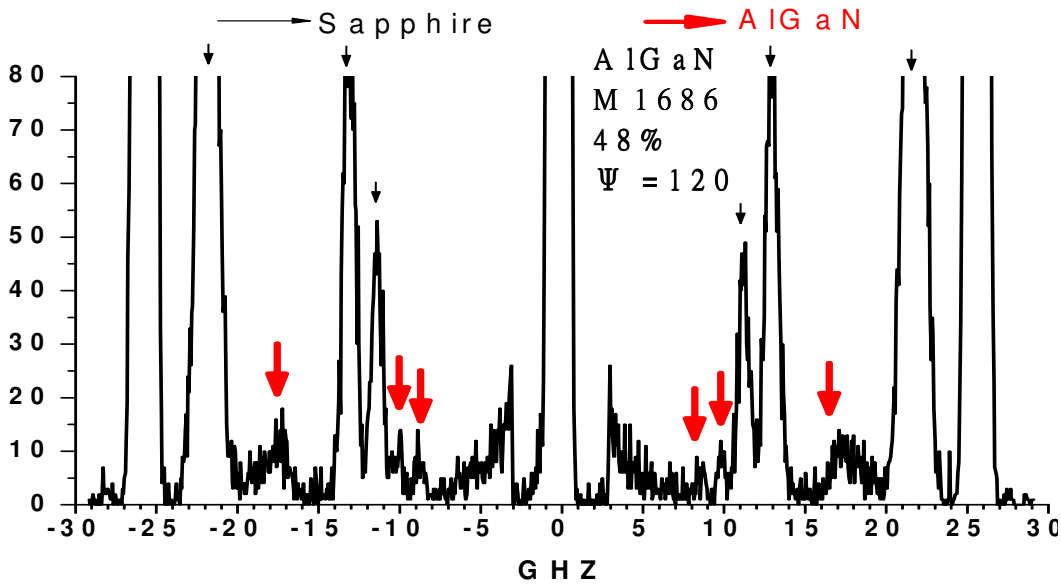

Figure 3.15 *Representative Brillouin spectra of $Al_{0.48}Ga_{0.52}N$ on sapphire at $\Psi=120°$*

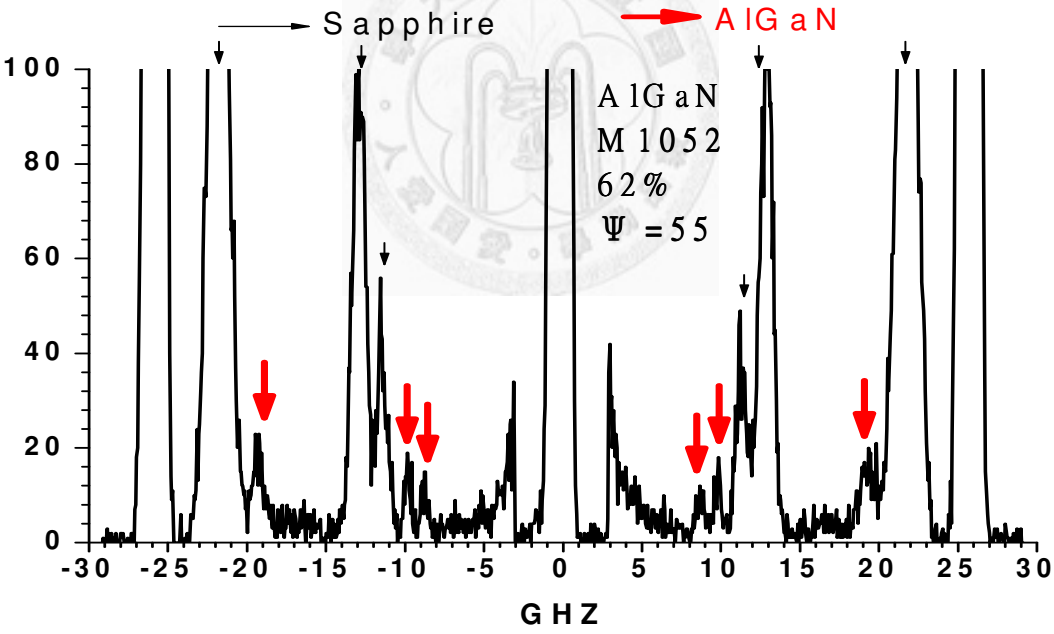

Figure 3.16 *Representative Brillouin spectra of $Al_{0.62}Ga_{0.38}N$ on sapphire at $\Psi=55$*

Figure 3.13 shows the Brillouin frequency of $Al_{0.2}Ga_{0.8}N$ (M1216) and sapphire. We obtained the TA (transverse acoustics)1, TA2, and LA (longitudinal acoustics)

frequency shifts at 8.2, 9.37, and 16.435 (GHZ) of AlGaN with~20% Al. Our Brillouin experiment utilizes a symmetric scattering geometry with an external angle between the incident and scattered beams of 60° as figure 3.3 showed. In this case, we change the specimen GaN into AlGaN. These acquisition enabled us to calculate the velocity (V) of each acoustic mode according to the formula $V= \lambda\Delta\omega /(2n \sin\theta)$ (3.1), where n, $\Delta\omega$, and λ are the refractive index of sample, the Brillouin shift, and the wavelength of laser, respectively. The refractive index of $Al_xGa_{1-x}N$ we used were from the reference [3.15]

Ψ (chi)	Δω(LA) GHZ	Δω(TA2) GHZ	Δω(TA1) GHZ	V(LA) km/sec	V(TA2) km/sec	V(TA1) km/sec
0	16.412	9.343	8.280	8.444	4.807	4.261
15	16.435	9.370	8.291	8.456	4.821	4.266
30	16.439	9.337	8.307	8.458	4.804	4.274
45	16.358	9.308	8.300	8.416	4.789	4.271
60	16.424	9.399	8.227	8.450	4.836	4.233
75	16.358	9.312	8.173	8.416	4.791	4.205
90	16.375	9.357	8.134	8.425	4.814	4.185
105	16.301	9.234	8.031	8.387	4.751	4.132
120	16.356	9.351	8.066	8.415	4.811	4.152
135	16.305	9.355	8.124	8.389	4.813	4.184
150	16.348	9.302	8.208	8.411	4.786	4.223
165	16.338	9.670	8.241	8.406	4.975	4.240
180	16.402	9.337	8.214	8.439	4.804	4.226

Table 3.4 *Brillouin frequency shifts ($\Delta\omega$) and acoustic velocities of $Al_{0.2}Ga_{0.8}N$*

Ψ (chi)	Δω(LA) GHZ	Δω(TA2) GHZ	Δω(TA1) GHZ	V(LA) km/sec	V(TA2) km/sec	V(TA1) km/sec
0	17.604	9.563	8.222	9.057	4.923	4.229
15	17.516	9.520	8.150	9.012	4.904	4.193
30	17.644	9.443	8.208	9.078	4.860	4.223
45	17.551	9.565	8.200	9.030	4.923	4.219
60	17.528	9.610	8.360	9.018	4.941	4.301
75	17.650	9.634	8.253	9.081	4.957	4.246
90	17.609	9.691	8.362	9.060	4.986	4.302
105	17.448	9.605	8.457	8.977	4.942	4.351
120	17.543	9.654	8.480	9.026	4.967	4.363
135	17.469	9.524	8.327	8.988	4.900	4.284
150	17.615	9.582	8.292	9.063	4.930	4.266
165	17.640	9.545	8.175	9.076	4.911	4.206
180	17.629	9.516	8.315	9.070	4.896	4.278

Table 3.5 *Brillouin frequency shifts (Δω) and acoustic velocities of* $Al_{04}Ga_{0.6}N$

Ψ (chi)	Δω(LA) GHZ	Δω(TA2) GHZ	Δω(TA1) GHZ	V(LA) km/sec	V(TA2) km/sec	V(TA1) km/sec
0	17.584	9.905	8.612	9.047	5.096	4.431
15	17.560	9.936	8.652	9.055	5.112	4.452
30	17.559	9.953	8.741	9.034	5.121	4.497
45	17.576	9.932	8.661	9.043	5.113	4.456
60	17.565	9.934	8.548	9.037	5.111	4.398
75	17.524	9.914	8.480	9.016	5.101	4.363
90	17.553	9.856	8.435	9.031	5.071	4.340
105	17.582	9.811	8.358	9.046	5.048	4.300
120	17.553	9.788	8.474	9.031	5.036	4.360
135	17.466	9.757	8.535	8.986	5.023	4.391
150	17.471	9.877	8.655	8.989	5.082	4.453
165	17.469	9.848	8.562	8.988	5.067	4.405
180	17.493	10.696	8.620	9.000	5.504	4.435

Table 3.6 *Brillouin frequency shifts (Δω) and acoustic velocities of* $Al_{048}Ga_{0.52}N$

Ψ (chi)	Δω(LA) GHZ	Δω(TA2) GHZ	Δω(TA1) GHZ	V(LA) km/sec	V(TA2) km/sec	V(TA1) km/sec
0	19.234	9.767	8.731	9.896	5.025	4.492
15	19.273	9.841	8.760	9.916	5.063	4.507
30	19.347	9.887	8.696	9.954	5.087	4.474
45	19.396	9.769	8.564	9.979	5.026	4.406
60	19.320	9.827	8.595	9.940	5.056	4.422
75	19.289	9.776	8.744	9.924	5.030	4.499
90	19.308	9.825	8.725	9.934	5.055	4.489
105	19.261	9.753	8.812	9.910	5.018	4.534
120	19.172	9.683	8.877	9.864	4.982	4.567
135	19.102	9.796	8.863	9.828	5.040	4.560
150	19.129	9.755	8.811	9.842	5.019	4.533
165	19.310	9.763	8.702	9.935	5.023	4.477
180	19.399	9.734	8.741	9.981	5.008	4.497

Table 3.7 *Brillouin frequency shifts (Δω) and acoustic velocities of* $Al_{0.62}Ga_{0.38}N$

Table 3.4-3.7 list the Brillouin frequency shifts and acoustic velocities by equation (3.1) for $Al_xGa_{1-x}N$, $x=0.2$, 0.4, 0.48, 0.62 respectively. According to the Christoffel's equation (3.2), the elastic constants can be calculated. The mass density of $Al_xGa_{1-x}N$ we used were from reference [3.10]. We do the same treatments on the other samples, then get the velocity of acoustic waves and fitting results as figure 3.16 showed. In Figure 3.16, the solid dots are our data, and the solid curves are the fitting results. Figure 3.16(a) shows the variation of TA1, TA2 and LA phonon waves velocity of $Al_{0.2}Ga_{0.8}N$ with propagation angle Ψ, while figure 3.16(b), 3.16(c) and 3.16(d) are those of AlGaN with Al comcentrations~40%, 48%, and 62% respectively.

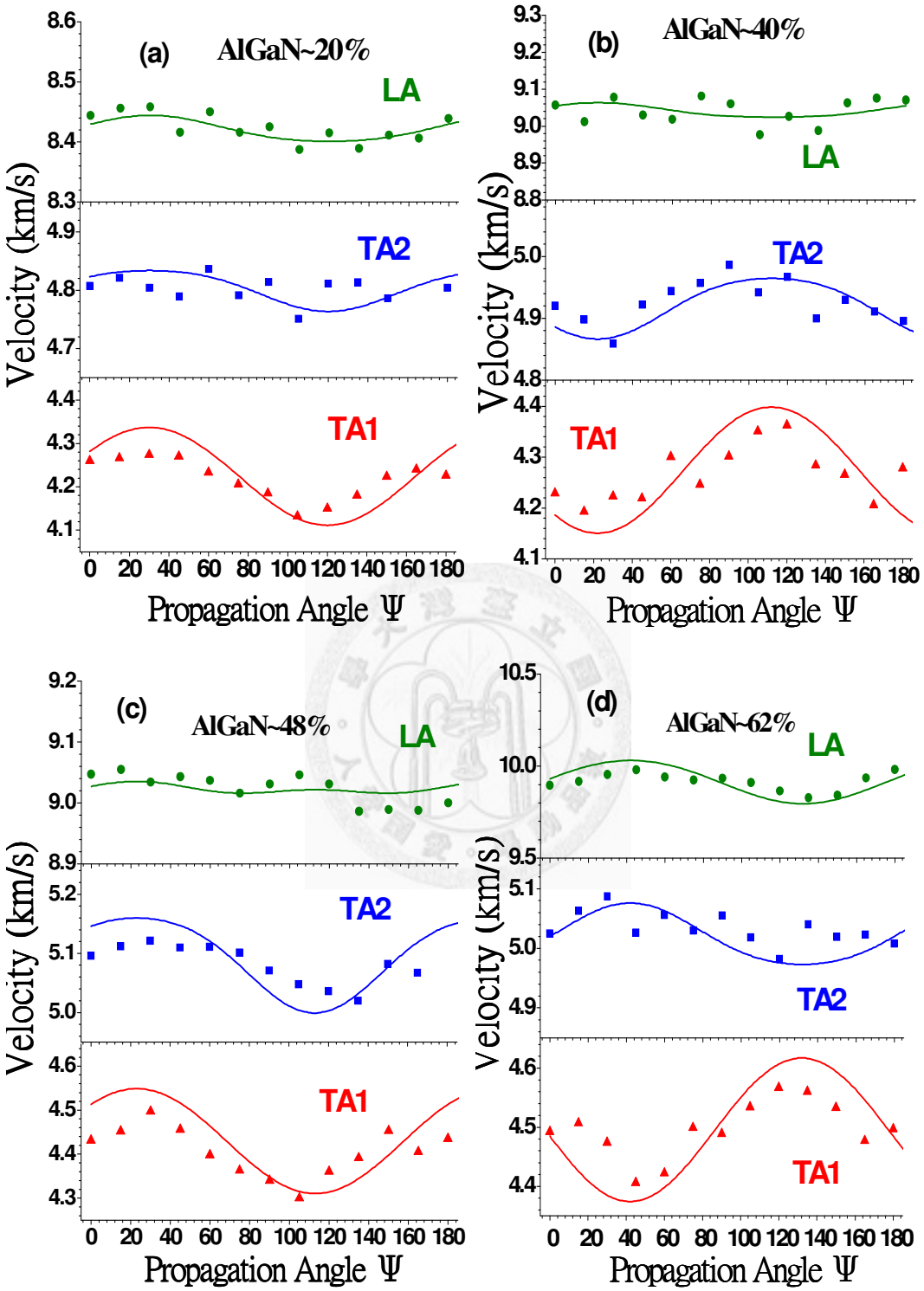

Figure 3.17 *Acoustic velocities versus Ψ angle of (a) AlGaN~20% (b) AlGaN~40% (c) AlGaN~48% (d) AlGaN~62%*

We obtained the velocity of acoustics waves increases along with the aluminum concentrations increases progressively. Especially, the velocities of LA waves change apparently. Average sound velocity of LA mode is increased from 8.43 km/s to 9.45 km/s when aluminum percentages changed from 20% to 62%. Compared the soud velocities we computed from Brillouin scattering experiments with the reference (figure.3.18) [3.16] showed. The values of refernce and our data are similar.

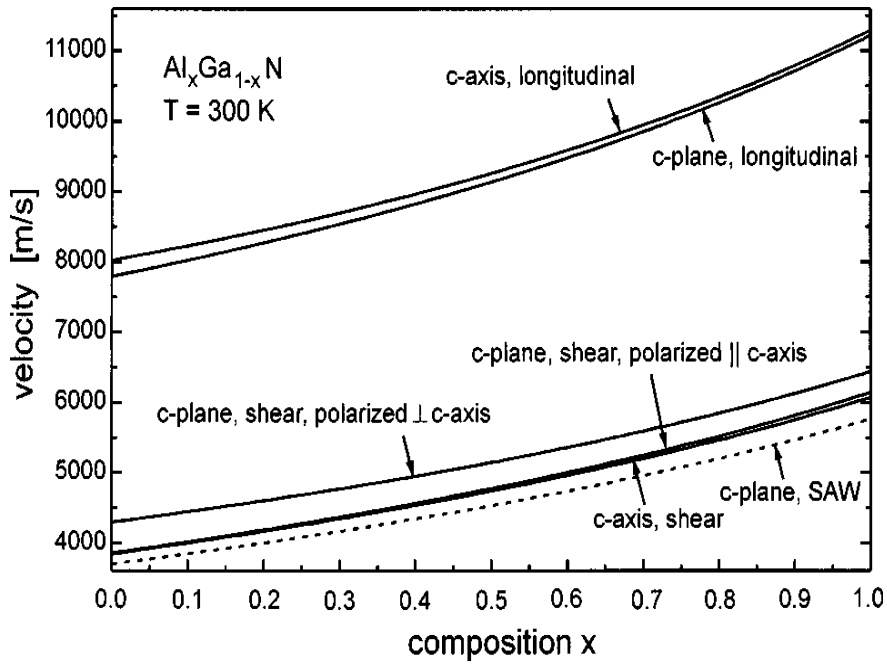

Figure 3.18 *SAW (dashed line) and BAW (solid lines) velocities of different modes propagating in the of $Al_xGa_{1-x}N$ [3.16].*

Accordingly, the elastic constants Cijs were listed in Table 1. In hexagonal system, only C_{11}, C_{33}, C_{44}, C_{66}, C_{12}, C_{13} have non-zero values ($C_{66}=(C_{11}-C_{12})/2$). It is obvious that the C_{ij}s of AlGaN are greater than those of GaN, except the C_{66}. The addition of Al in GaN has caused a significant rise in bulk modulus and a moderate

increase in shear modulus. Using the measured elastic moduli, it is easy to compute the bulk modulus. In a hexagonal lattice, the bulk modulus is related to the elastic constants by this equation (3.3)

C_{ij}	C_{11}	C_{33}	C_{44}	C_{66}	C_{12}	C_{13}
GaN [3.4]	**390**	**398**	**105**	**123**	**145**	**106**
GaN [3.5]	**366**	**366.5**	**115**	**87**	**192**	**133**
GaN (fitting)	**365.68**	**366.5**	**115.14**	**86.88**	**191.91**	**132.52**
AlGaN~20%	**385.5**	**400.44**	**108.26**	**77.78**	**229.95**	**203.46**
AlGaN~40%	**389.58**	**412.76**	**114.36**	**89.96**	**209.67**	**159.29**
AlGaN~48%	**396.7**	**413.10**	**118.47**	**96.88**	**202.95**	**144.76**
AlGaN~58%	**427.48**	**418.84**	**125.25**	**114.27**	**198.95**	**142.28**
AlN [3.17]	**413**	**386**	**126**	**142**	**129**	**96**

Table 3.8 *Elastic constants of GaN, $Al_xGa_{1-x}N$, and AlN*

3.2.3.2 High-resolution X-ray Diffraction Measurement

Diffraction can occur when X-ray interacts with a periodic structure whose periodic distance is about the same as the wavelength of the X-ray. When X-rays scattered from several sources overlap in space simultaneously, constructive and destructive interference will occur. Interference appears among the waves scattered by the atoms when crystalline solids are exposed to X-rays. The atoms in the crystal, like a periodic grating, scatter the incoming radiation, resulting in diffraction patterns. Destructive interference occurs most often, but in specific directions constructive interference occurs. Because X-rays have wavelengths on the order of angstroms, in the

range of typical inter-atomic distances in crystalline solids, they can be diffracted from the repeating patterns of atoms that are characteristic of crystalline materials.

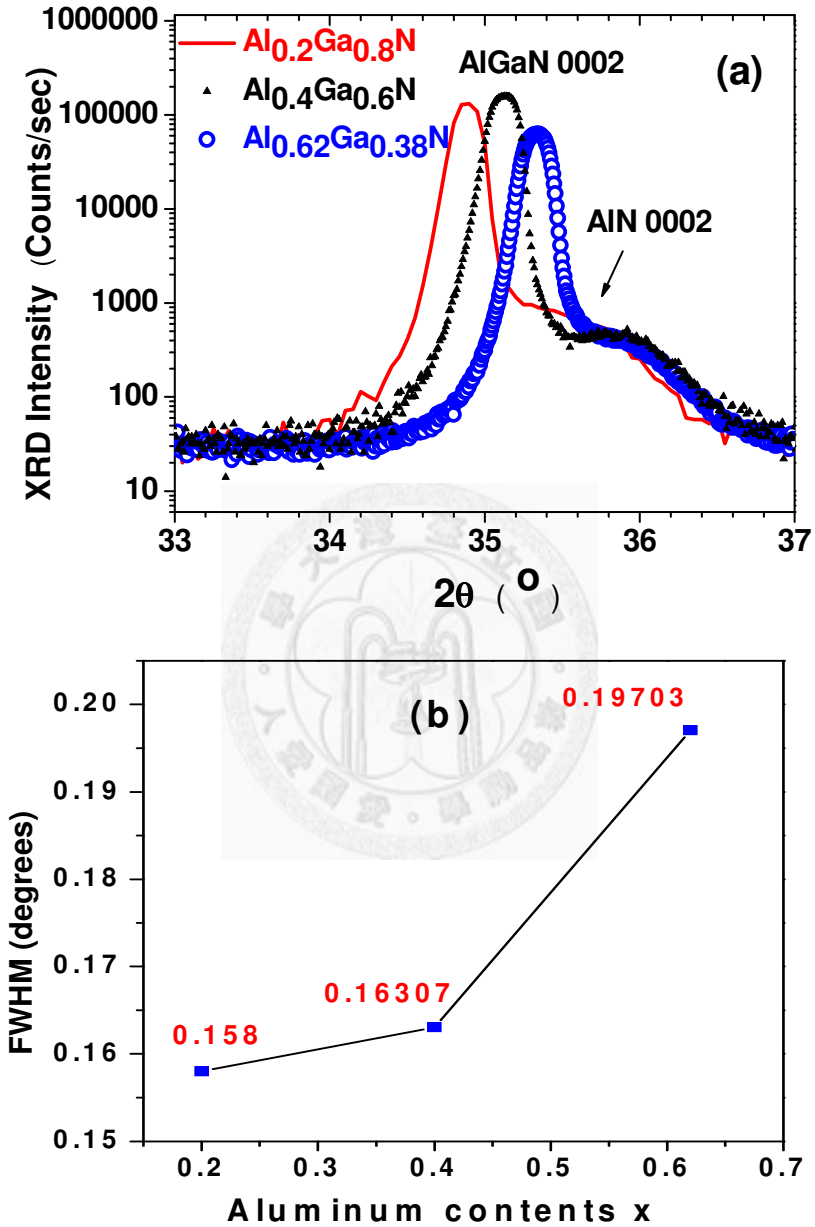

Figure 3.19 *(a) XRD spectrum of $Al_xGa_{1-x}N$*

(b) FWHM of XRD spetra versus aluminum contents

Figure 3.19(a) shows the high resolution XRD scans from 33° and 37° . It can be

appreciated that the AlGaN reflection shifts to higher angles, in correlation with an increase in the Al content (change in the lattice parameter). This change is not surprising since the critical thickness for strain relaxation scales with the Al incorporation. The full width at half maximum (FWHM) of the XRD reflections reveals the good crystalline and epitaxial quality of the layers. The evolution of the FWHM upon Al incorporation in the AlGaN layer is displayed in Figure 3.19(b). The sharp increase of FWHM of the $Al_xGa_{1-x}N$ (0002) is found $x=0.4$ to $x=0.62$, where the configuration is more sensitive to strain, for the largest Al content. The previous trends indicate that the sample crystallinity slightly deteriorates upon Al incorporation above x~0.4 and that the strain within the layer is relevant for the largest Al content.

3.6 Raman scattering (RS)

Both the E2 and the A1(LO) phonon frequency are affected by the aluminium composition *x* in $Al_xGa_{1-x}N$ layers, as shown in figure 3.20. Results for $Al_xGa_{1-x}N$ layers grown by metalorganic vapour phase epitaxy (MOVPE) on sapphire substrates reported by Demangeot *et al*. [3.18] are displayed. Similar data were presented in reference [3.19]. The A1(LO) phonon frequency increases continuously from the GaN A1(LO) to the AlN A1(LO) phonon frequency with increasing aluminium composition. This is in contrast to the E2 phonons where two sets of odes are observed, each set corresponding to one of the pure crystals that compose the alloy, i.e. GaN and AlN (two-mode

behaviour).

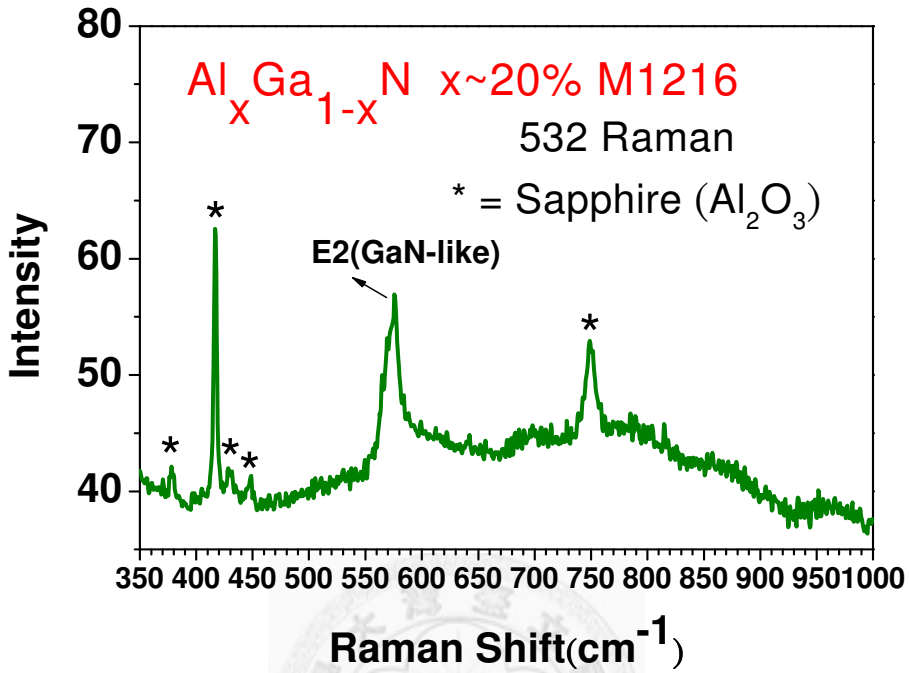

Figure 3.20 *(a) Raman spectrum of $Al_{0.2}Ga_{0.8}N$*

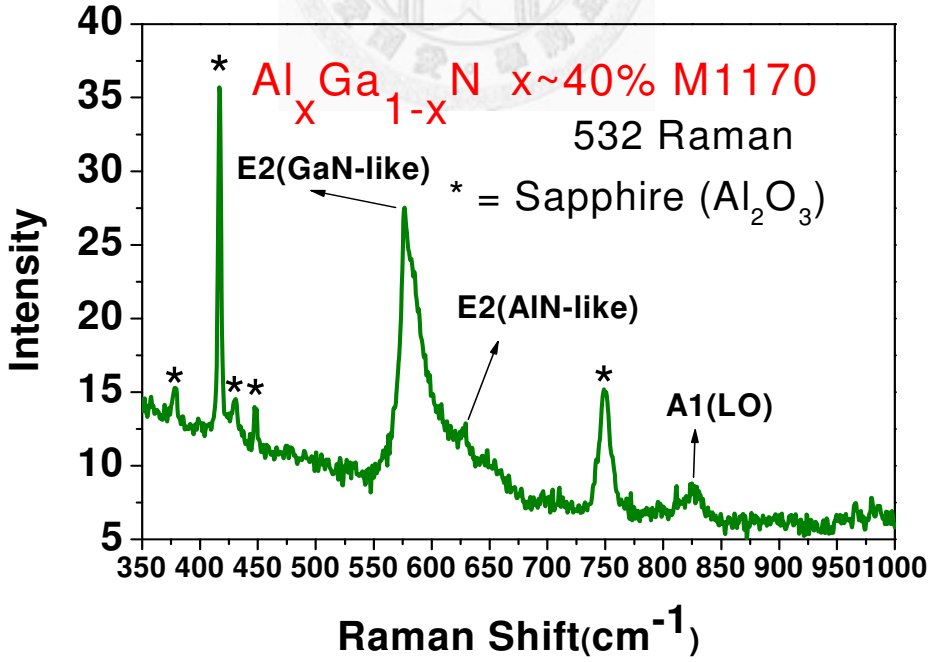

Figure 3.20 *(b) Raman spectrum of $Al_{0.4}Ga_{0.6}N$*

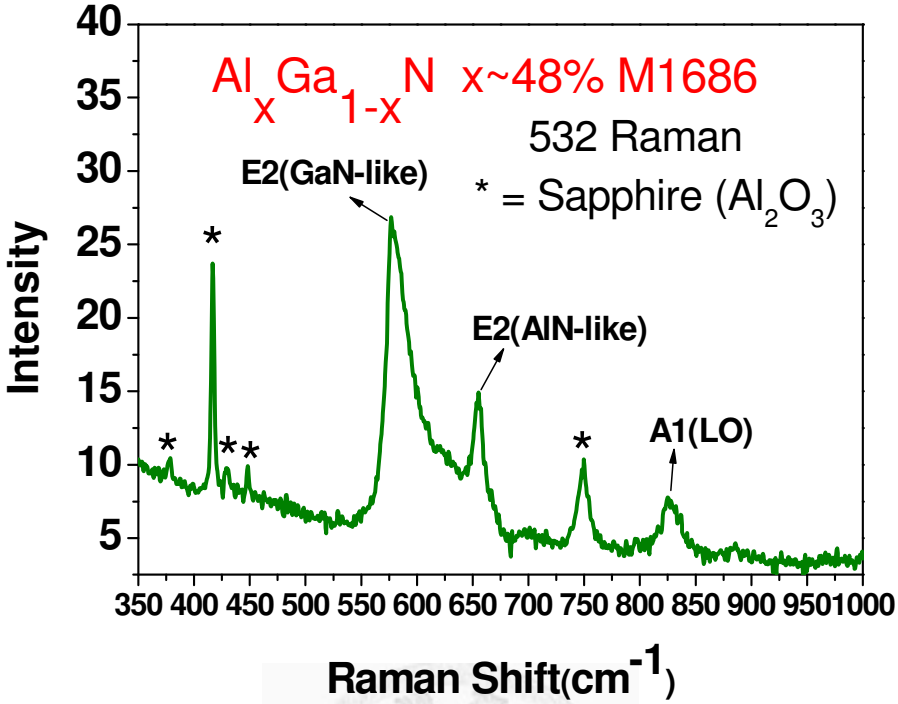

Figure 3.20 *(c) Raman spectrum of* $Al_{0.48}Ga_{0.52}N$

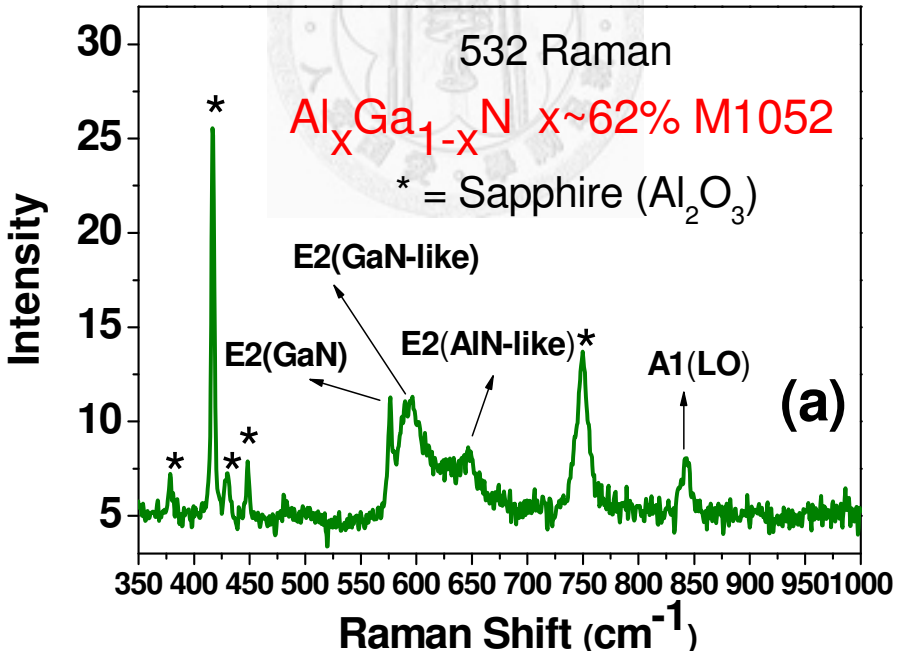

Figure 3.20 *(d) Raman spectrum of* $Al_{0.62}Ga_{0.38}N$

	$Al_{0.2}Ga_{0.8}N$	$Al_{0.4}Ga_{0.6}N$	$Al_{0.48}Ga_{0.52}N$	$Al_{0.62}Ga_{0.38}N$
E2 (GaN) (cm^{-1})				576.95
E2 (GaN-like) (cm^{-1})	575.68	580.98	582.12	594.3
E2 (AlN-like) (cm^{-1})		627.08	651.2.	650.08
Al(LO) (cm^{-1})		823.30	827.21	842.58

Table 3.9 *Raman mode of $Al_xGa_{1-x}N$*

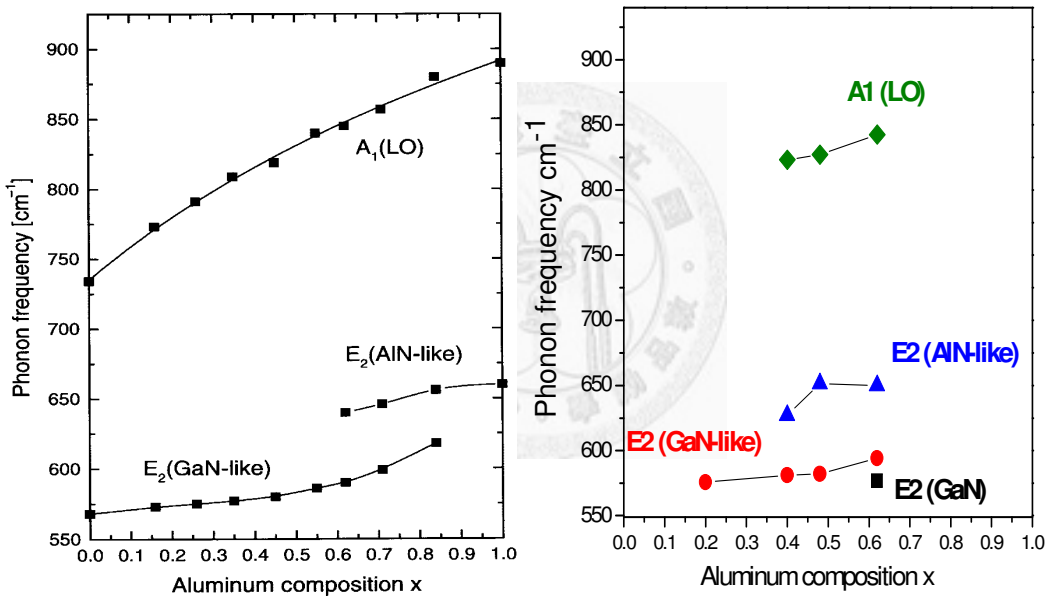

(a) (b)

Figure 3.21 (a) *Phonon frequency of the E2 and A1(LO) phonons of $Al_xGa_{1-x}N$ as a function of the aluminium composition x, obtained at room temperature under 488 nm excitation. (From [3.18]) (b) Our results in this work*

3.6 Summary

Brillouin spectroscopy has been adopted to measure the elastic properties of

$Al_xGa_{1-x}N$/sapphire for x =0.2, 0.4, 0.48, and 0.62. The sound velocities of TA1, TA2, and LA waves increase with the high Al concentrations. Especially, the velocities of LA waves increase obviously. These detailed studies of elasticity have provided information concerning intermolecular forces that is important to the overall understanding of physical properties of inclusion compounds and other molecular solids. The increase of Al in GaN cause its Raman scattering peaks move toward high wavenumber side. XRD spectra showed the strain within the layer is relevant for the largest Al content.

Reference

[3.1] G.T. Thaler, D.D. Koleske, S.R. Lee, K.H.A. Bogart, M.H. Crawford, Journal of Crystal Growth, 312, 1817 (2010)

[3.2] X.H. He, J. Zhou, N. Lian, J.H. Sun, M. Guan, Journal of Luminescence, 130, 743 (2010)

[3.3] F.M. Morales, D. Gonza'lez, J.G. Lozano, R. Garcı'a , S. Hauguth-Frank , V. Lebedev, V. Cimalla, O. Ambacher, Acta Materialia , 57, 5681 (2009)

[3.4] A. Polian, M. Grimsditch, I. Grzegory, J. A. Phy. 79, 3343 (1996)

[3.5] M . Yamaguchi, T. Yagi, T. Sota, T. Deguchi, and K. Shimada, S. Nakamura **,** J. A. Phy. 8502 (1999)

[3.6] C. C. Chen, C. C. Lin, L. Liu, S.V. Sinogeikin, J.D. Bass, Am. Miner. 86,

1525(2001)

[3.7] S. V. Sinogeikin, J. D. Bass, Phys. Earth Planet. Int. 120, 43. (2000)

[3.8] T. Kawashima, H. Yoshikawa, S. Adachi, S. Fuke, and K. Ohtsuka, J. Appl.Phys. 82, 3528(1997)

[3.9] V. Bucur , P. Lanceleur, B. Roge, Ultrasonics 40, 537 (2002)

[3.10] I. Vurgaftman and J. R. Meyer, *J.* Appl. Phys. 94, 6, 3675(1999)

[3.11] G. Wetzel, T. Takeuchi, S. Yamagachi, H. Katoh, H. Amano, and I.Akasaki, Appl. Phys. Lett. 73, 1994 (1998).

[3.12] L. Bellaiche, T. Mattila, L.-W. Wang, S.-H. Wei, and A. Zunger, Appl. Phys. Lett. 74, 1842 (1999).

[3.13] Z. C. FENG, "III-Nitride Devices and Nano-Engineering", Imperia College Press, London (2008)

[3.14] Z. C. FENG, "III-Nitride Semiconductor Materials", Imperia College Press, London (2006)

[3.15] G. M. Laws, E. C. Larkins, and I. Harrison, C. Molloy and D. Somerford, *J.* Appl. Phys. 89, 2, 1108 (2002)

[3.16] C. Degera, E. Born, H. Angerer, O. Ambacher, M. Stutzmann, J. Hornsteiner, E. Riha, and G. Fischerauer, Appl. Phys. Lett. 72, 19 (1998)

[3.17] M. Iuga, G. Stein-Neumann, and J. Meinhardt, *Eur. Phys. J. B 58*, *127* (*2007*)

[3.18] F. Demangeot, J. Groenen, J. Frandon, M.A. Renucci, O. Briot, S. Uffenach-Clur, R.L. Aulombard, MRS Internet J. Nitride Semicond. Res.; 2: 40.(1997)

[3.19] A. Cros, H. Angerer, R. Handschuh, O, Ambacher, M. Stutzmann, MRS Internet J. Nitride Semicond. Res. 2, 43. (1997)

Chapter 4 Synchrotron Radiation and Related Studies on 6H-SiC materials

4.1 Introduction

4.1.1 Silicon carbide

Silicon carbide (SiC) which is a wide band gap semiconductor with an indirect band structure is an attractive material for high-temperature and high-voltage power applications and optical sensors in the ultraviolet region. It is well known that SiC crystallizes in numerous different modifications (polytype). The most important are: cubic unit cell: 3C-SiC (cubic unit cell, zincblende); 2H-SiC; 4H-SiC; 6H-SiC (hexagonal unit cell, wurtzite); 15R-SiC (rhombohedral unit cell). 4H- and 6H-SiC are of considerable technological interest due to their large band gaps, high electron mobility, commercial availability and wide use in device manufacturing and as substrate materials. Research and development of SiC materials, devices and applications have gained much attention in recent years. Bulk single crystal wafers of 6H-SiC and 4H-SiC have been commercially available. SiC has been recognized as the power electronic materials for the 21-century [4.1, 4.2]. The demand for good quality SiC wafers is increasing. The control of the polytype during crystal growth is important, because the band gap energy and electrical properties are different for different polytypes. Recent development of the crystal growth and device fabrication for SiC crystals requires the

polytype identification and the qualitative characterization of as-grown and processed SiC crystals.

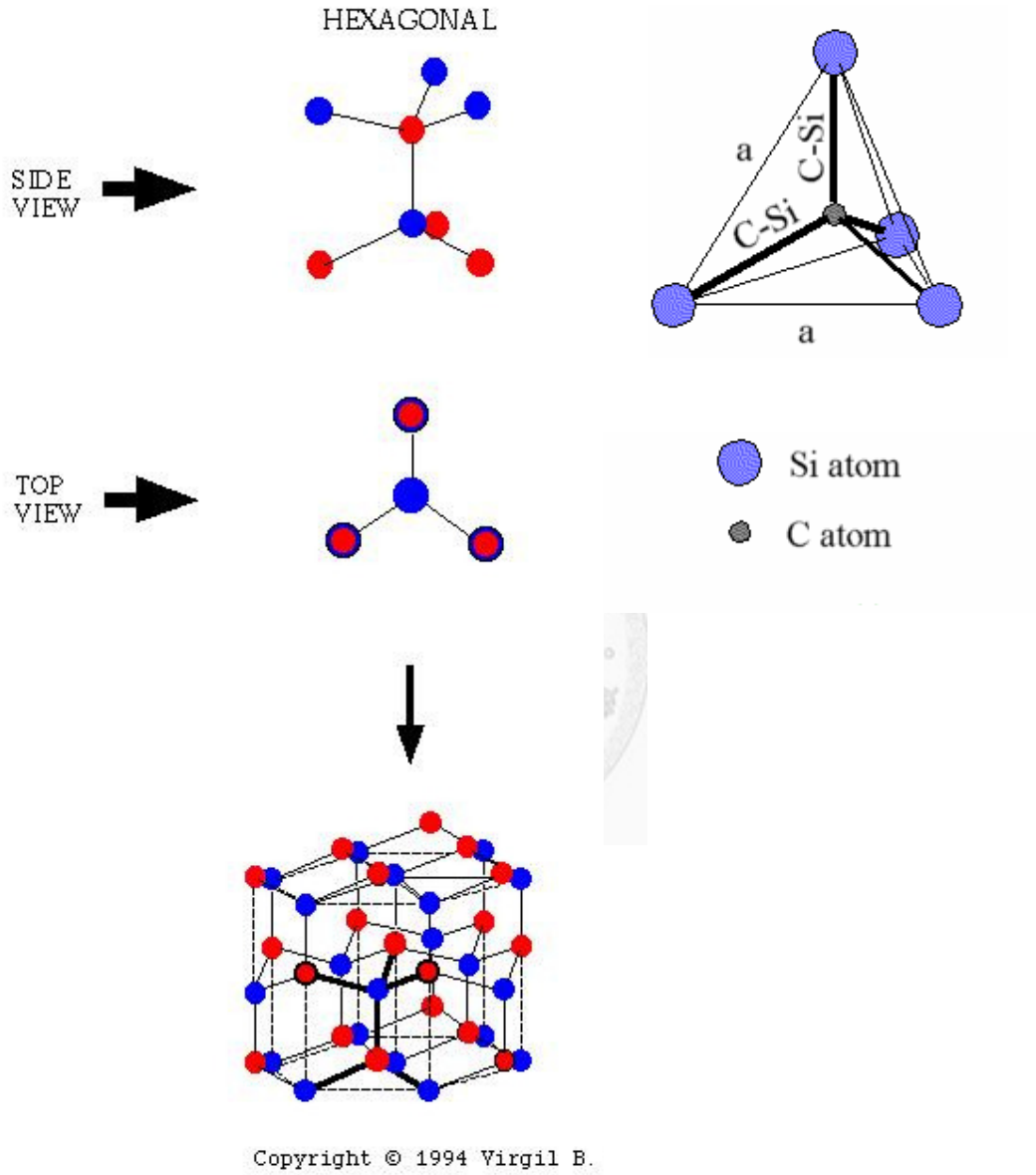

Figure 4.1 *Stacking sequence of three common SiC polytypes.*

Raman scattering is a powerful technique for the characterization of SiC. It is non-destructive and requires no special preparation of samples. Furthermore, the Raman

efficiency of this material is high because of the strong covalence of the bonding and the Raman signals are easily obtained. The Raman parameters such as intensity, width, peak frequency and polarization of Raman bands provide fruitful information on the crystal quality and material properties. A series of N-doped n-type 6H-SiC bulk wafers are studied. Interesting results are obtained and discussed.

Si-C Polytype	*6H*-SiC
Crystal structure	Wurtzite (Hexagonal)
Crystal structure	C^4_{6v}-$P6_3mc$
Lattice constant	a = 3.0730 Å, b = 10.053 Å

Table 4.1 *SiC Polytype of 6H*

4.1.2 Synchrotron radiation beamline end station

Synchrotron Radiation X-ray absorption spectroscopy (XAS, or so called X-ray Absorption Fine-Structure, XAFS) has been proved to be a strong spectroscopic analysis technique for the structure information from material. It uses x-rays to probe the physical and chemical structure of matter at an atomic scale. In a standard XAFS

spectrum, it could be divided into two parts, one is X-ray Absorption Near Edge Structure (XANES) or Near Edge X-ray Absorption Fine-Structure (NEXAFS), the other is Extended X-ray Absorption Fine-Structure (EXAFS). The great power of XANES derives from its elemental specificity. Because the various elements have different core level energies, XANES permits extraction of the signal from a surface monolayer or even a single buried layer in the presence of a huge background signal. The XANES spectra are also sensitive to the coordination environment of the absorbing atom in the sample. Finger printing methods have been used to match the XANES spectra of an unknown sample to those of known "standards". Linear combination fitting of several different standard spectra can give an estimate to the amount of each of the known standard spectra within an unknown sample. EXAFS spectra are displayed as graphs of the absorption coefficient of a given material versus energy, typically in a 500 – 1000 eV range beginning before an absorption edge of an element in the sample. The x-ray absorption coefficient is usually normalized to unit step height. This is done by regressing a line to the region before and after the absorption edge, subtracting the pre-edge line from the entire data set and dividing by the absorption step height, which is determined by the difference between the pre-edge and post-edge lines at the value of E0 (on the absorption edge). [4.3] [4.4]

The DCM tender X-ray beamline is a bend-magnet soft X-ray beamline, which provides good monochromatized photon beams with energies from 1 up to 8 keV that covers the K edges of elements from Na to Cr and L edges of the first and second rows of transition metals. This beamline provides good opportunity to study some important materials such as zeolites, catalysis, and etc. This beamline takes the leftmost 6 mrads of the horizontal radiation from the BL16 port. After the front-end, the photon beam passes through a graphite filter and slit aperture, and is then vertically collimated by a water-cooled Silicon mirror (Coating: 800Å (±10%) Nickel) located at 5.7 m. The collimated beam is then dispersed by a double crystal monochromator (DCM) at 9 m. The monochromatized beam is then focused by a bent toroidal glidcop mirror at 11.7 m and reaches the sample position at 18.20 m. This beamline delivers soft X-ray beams from 1 to 8 keV with energy resolving power of up to 7000.

Source	Acceptance Angle H × V (mrad)	Monochromator	Energy (keV)	Focused Beam Size H × V (mm)	Resolving Power E/DE	Flux (photons/sec)
BM	6 × 0.5	DCM	1 ~ 8	0.25 × 0.16	7000	3×10^{11}

Table 4.2 *BL16A DCM Tender X-ray Beamline*

.

Monochromator	DCM, Si(111), InSb(111), Beryl(1010)
Mirrors	CM and FM
Method of Focusing	1.4 m toroidal mirror
Beam Size on Sample or Detector	0.5 mm × 1 mm

Table 4.3 *Optical Parameters of BL16A*

E = 1.5 GeV, I = 300 mA, $_c$ = 8.89 Å, P = 3.45 W/mrad			
Energy Range	900 eV ~ 8 keV		
Scanning Range	12° ~ 72°		
Horizontal Acceptance Angle	6 mrad		
Mono. Crystal	Beryl (1010)	InSb(111)	Si (111)
2d (Å)	15.92	7.48	6.27
Energy Range (keV)	0.9 ~ 2	1.75 ~ 4	2.1 ~ 6
Scanning Angle	59.9° ~ 22.9°	72.0° ~ 24.5°	70.2° ~ 19.2°
Resolving Power (E/ E)	2500	3000	7000
Flux (photons/sec)	3×10^{11}		
Spot Size (H × V)	< 0.5 mm × 1.0 mm		
Sample Position	18.20 mm		

Table 4.4 *Characteristics of DCM Tender X-ray Beamline.*

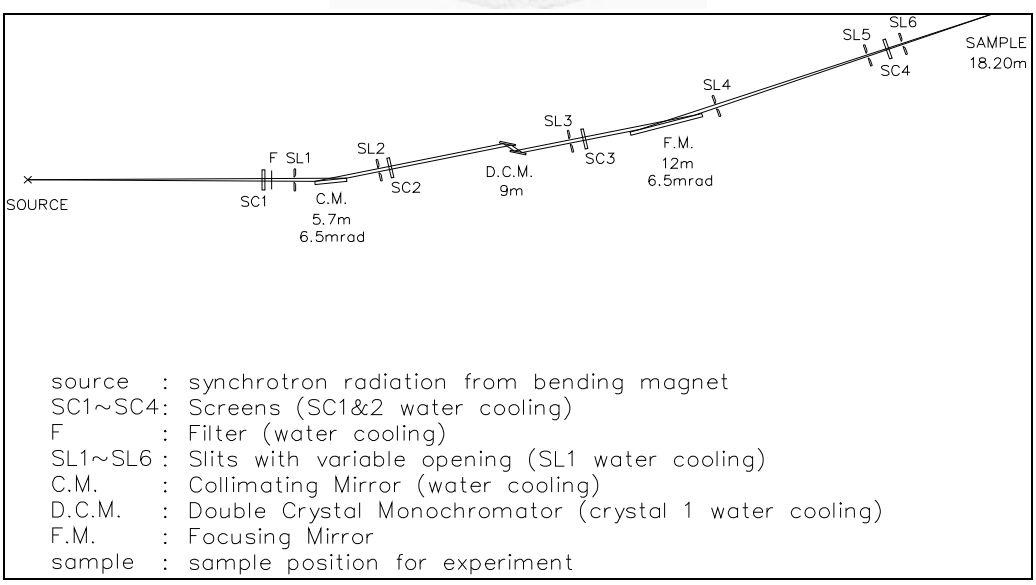

Figure 4.2 *Optical Layout of BL16A.*

1	Double ion chambers.
2	Lytle detector (Fluorescent X-ray ion chamber detector).
3	Electron yield detector.
4	LINUX/PC for beamline control, data collection and processing using SPEC/C-PLOT software.

Table 4.5 *Facilities in Experimental Station of BL16A*

4.2 Result and discussion

4.2.1 Sample information

Several commercially purchased 6H-SiC wafers from CREE company were involved in this study. They are nitrogen doped n-type with different values of resistivity and concentration, as listed in Table 4.6.

	Structure (6H-SiC bulk wafer)	Resistivity (Ω-cm)
6H054	N-doped n-type	0.054
6H151	N-doped n-type	0.151
6H177	N-doped n-type	0.177

Table 4.6 *Sample information of 6H-SiC*

4.2.2 Raman Scattering

Raman spectroscopy was performed by J.Y. (Jobin Yvon) T6400 Raman system and under excitation of 780 nm at room temperature. The laser power is controlled at

200mW. And the XAFS spectroscopy was measured in National Synchrotron Radiation Research Center (NSRRC), Hsinchu, Taiwan.

Figure 4.3 shows the Raman spectra which are employed by the J.Y. (Jobin Yvon) T6400, 780 nm. As shown, the significant change in three transverse optical (TO) mode peak with different samples is not obvious. But the longitudinal optical A1(LO) signal shift a little toward high frequency with the increase of N dopings. While the FWHM (Full-Width Half-Maximum) of A1(LO) mode is getting broaden. The FWHM of LO mode increase from 4.267 cm^{-1} of 6H177 to 6.254 cm^{-1} of 6H054 as listed in Table 3.2. We believed that it is arisen from the amorphous Si-Si vibration, indicating a slight damage of crystalline structure from the heavy N-doping.

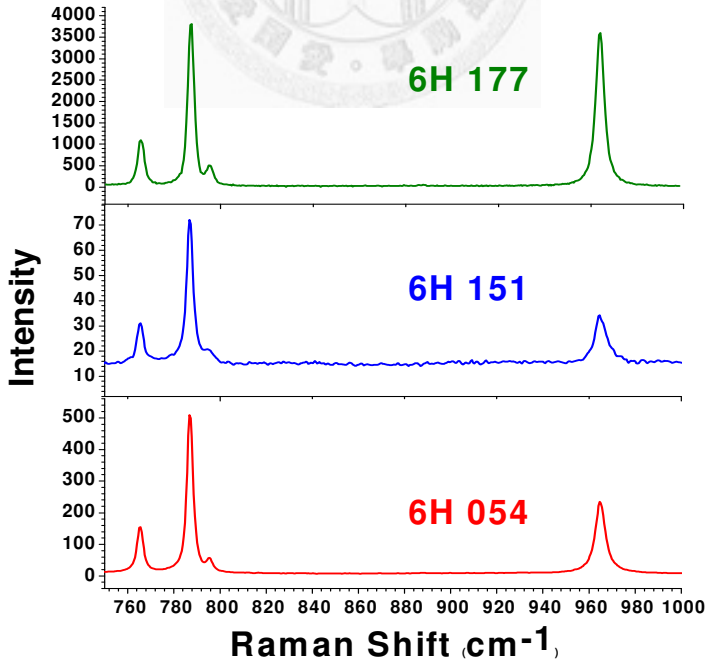

Figure 4.3 *The comparison of Raman scattering in the samples 6H-SiC.*

	6H054	6H151	6H177
E_2 (To) low (cm^{-1})	765.43	765.48	765.51
FWHM (cm^{-1})	3.186	3.2079	3.325
E_2 (To) high (cm^{-1})	787.05	786.99	787.18
FWHM (cm^{-1})	3.281	3.301	3.332
E_1 (To) (cm^{-1})	795.18	794.65	795.12
FWHM (cm^{-1})	5.923	4.055	3.283
A1 (LO) (cm^{-1})	965.05	964.78	963.84
FWHM (cm^{-1})	6.254	5.111	4.267

Table 4.7 *Statics of Raman fitting*

4.2.3 X-ray Absorption Fine-Structure Study on 6H-SiC

With the help of x-ray absorption fine structure, we can simulate the bond length nearest and next nearest to the absorbed atom. Here, silicon is the absorbed atom, the nearest and next nearest bond length is Si-C and Si-Si, respectively.

Extended x-ray absorption fine structure measurements at the Si K absorption edge were carried out at the double-crystal monochromator beamline of the National Synchrotron Radiation Research Center (NSRRC) in Hsinchu, Taiwan. The absorption spectra were record by detecting the fluorescence from the sample, which is proportional the x-ray absorption, as a function of incident photo energy in the

(1750-2700) eV range. Here we would focus on the extended x-ray absorption fine structure oscillations region (from about tens of eV above absorption edge to up to 2700-eV photo energy).

The EXAFS signal was extracted from the raw x-ray absorption spectrum and analyzed according to the procedure reported in [4.5]. Basically, the data analysis procedure consist of (1) transforming the spectra from energy to K-space with k^3-weigthed (or k^2, k^1, depends on data) multiplication; (2) subtracting the nonoscillatory background generated by fitting the data by the three equal-section cubic spline function, and thereby isolating the characteristic EXAFS oscillations of the absorption coefficient; (3) Fourier-transforming the k^3-weigthed oscillations in R space to obtain the approximate radial position of the coordination shells surrounding the Si absorbing atoms; (4) sorting out and back transforming in the K-space the peak corresponding to a given coordination shell; and, finally, (5) curve fitting of these characteristic oscillations with the known backscattering amplitudes and phase shift functions of the individual components involved in a given environment; this allows the extraction of the quantitative structure parameters of the sorted out coordination shell.

Figure 4.4 shows the original raw spectra of XAFS. Figure 4.5-4.7 shows the Si K-edge oscillation $k^3\chi(k)$ for three 6H-SiC samples. In fact, the raw spectra can not tell us much information of material in EXAFS analysis. We can only know that if it was a

good data from no much glitch in it. But by using specific fitting software, we can transform the raw data into Fourier transformation spectra. From Fourier transformation spectra, the peaks are from the reflective waves from the atoms near the absorbed Si. The first peak means the reflective wave from the nearest atom, which we can know is C. And the second wave is from the next nearest atom, Si, and so on. By the Fourier transformation spectra, the bond length could be stimulated by some software .But the following peaks become not so obvious and the stimulated result would be not as precise as the first two peaks.

Reference			American Mineralogist (2007) **92**, 403-407				
Compound			**C1 Si1** - **[Moissanite 6H]** Silicon carbide - 6H				
Cell			3.0810(2), 3.0810(2), 15.1248(10), 90., 90., 120. **P63MC (186)** V=124.34				
Remarks			R=0.020500 : XDS TYP =SiC(6H) : MIN =Moissanite 6H :				
Atom (site) Oxid.			**x, y, z, B, Occupancy**				
Si1	(2a)	0	0.	0.	0.	0.005(1)	1
Si2	(2b)	0	0.3333	0.6667	0.1664(1)	0.005(1)	1
Si3	(2b)	0	0.6667	0.3333	0.3329(1)	0.005(1)	1
C1	(2b)	0	0.3333	0.6667	0.0412(2)	0.005(1)	1
C2	(2b)	0	0.6667	0.3333	0.2080(2)	0.005(1)	1
C3	(2a)	0	0.	0.	0.3746(2)	0.005(1)	1

Table 4.8 *EXAFS Model of 6H-SiC*

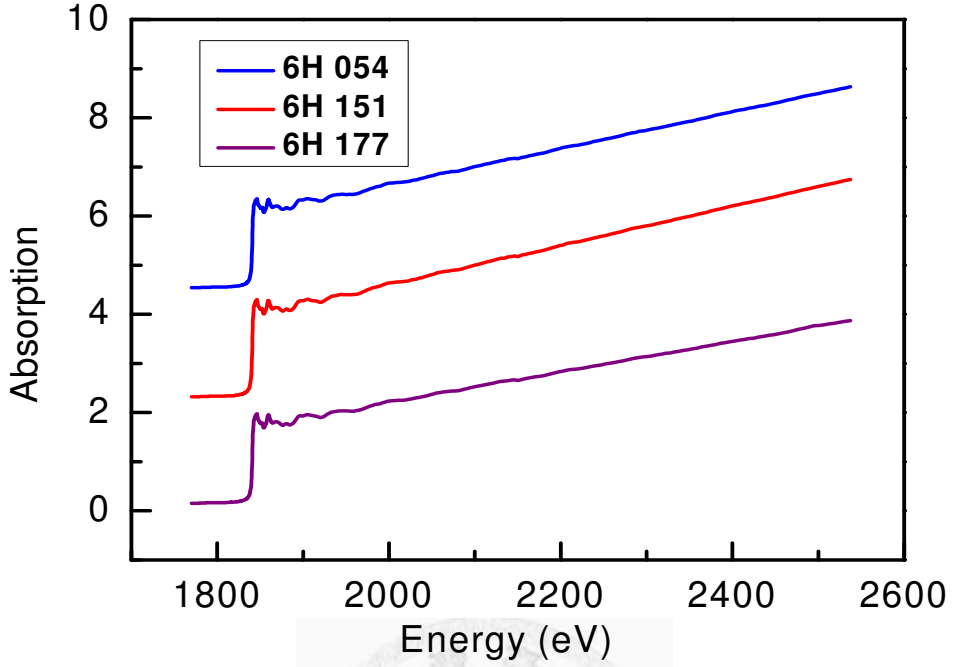

Figure 4.4 *The XAFS raw spectra of 6H-SiC*

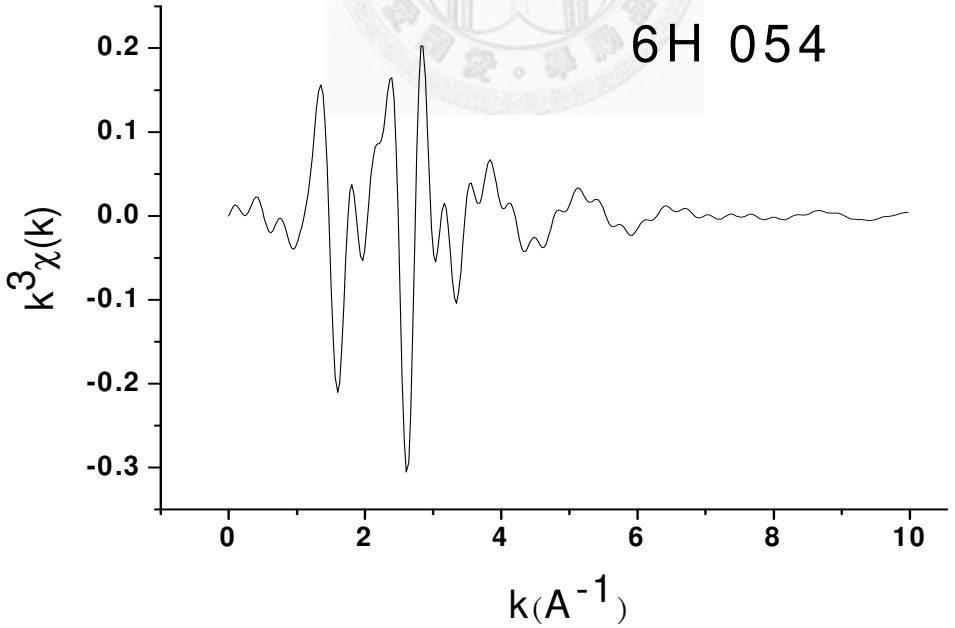

Figure 4.5 *The Si K-edge oscillation $k^3\chi(k)$ for 6H-SiC 054*

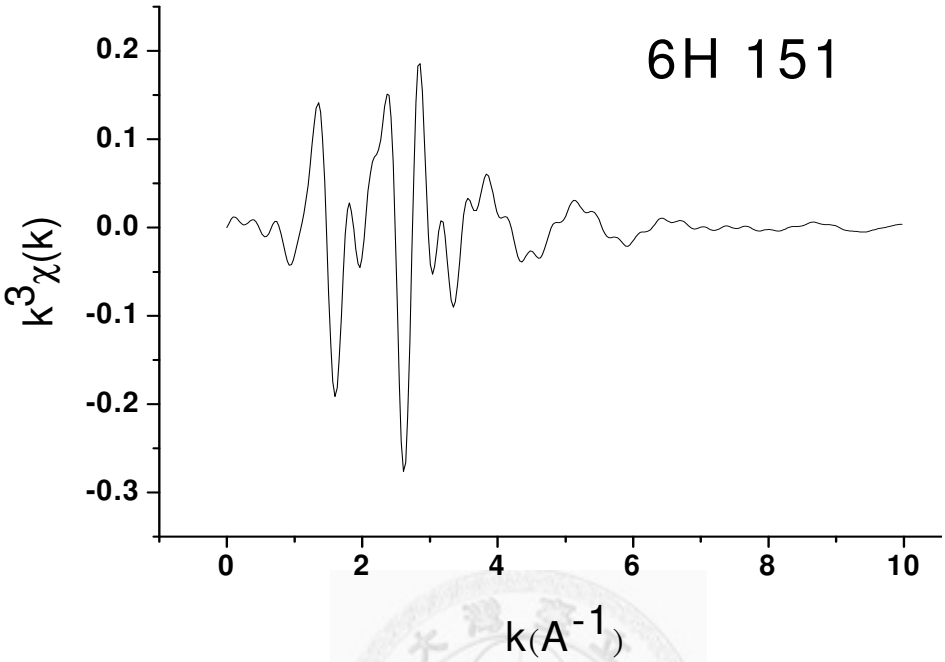

Figure 4.6 *The Si K-edge oscillation $k^3\chi(k)$ for 6H-SiC 151*

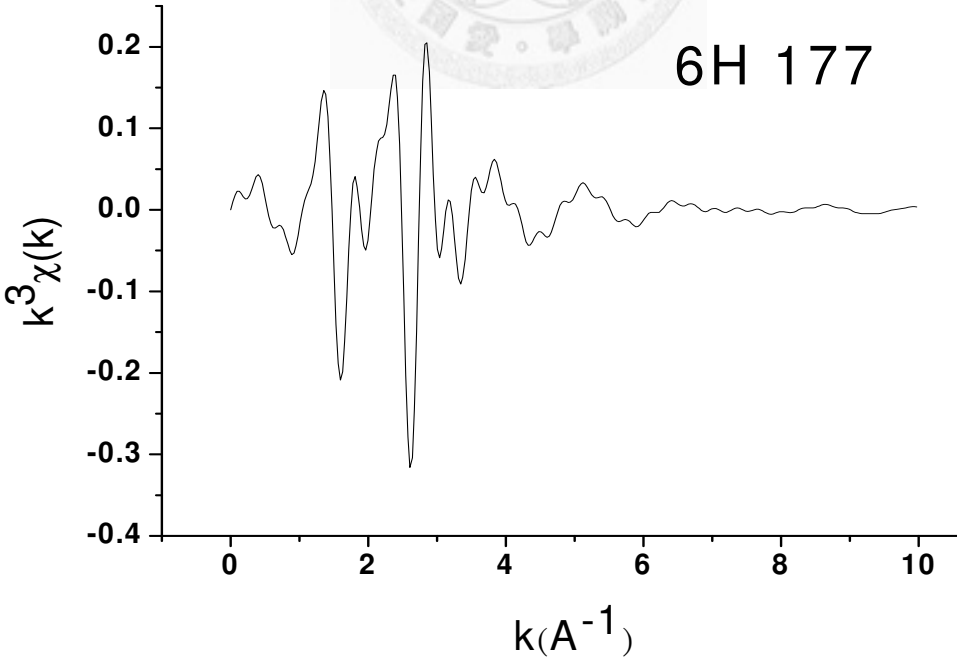

Figure 4.7 *The Si K-edge oscillation $k^3\chi(k)$ for 6H-SiC 177*

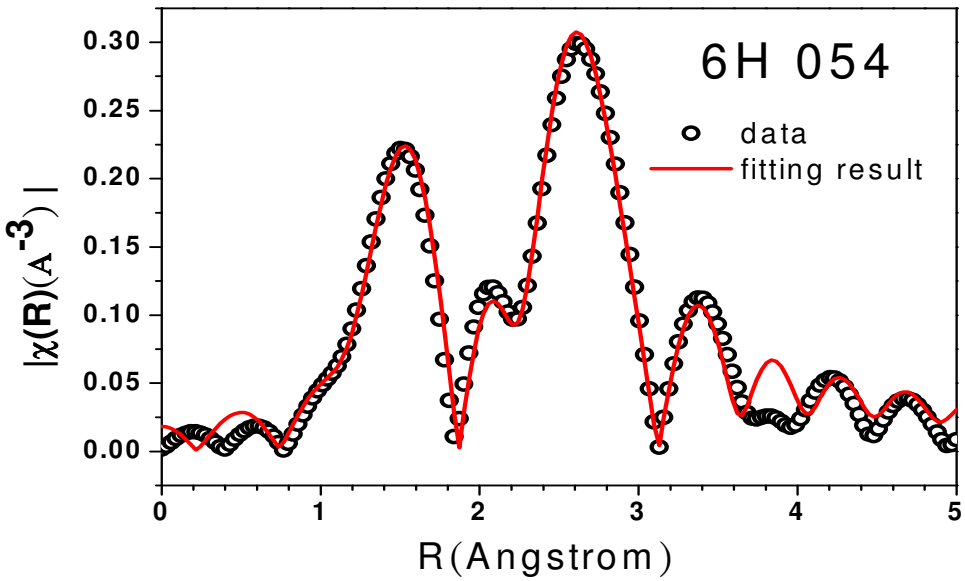

Figure 4.8 *Fourier Transformation spectra of 6H-SiC 054*

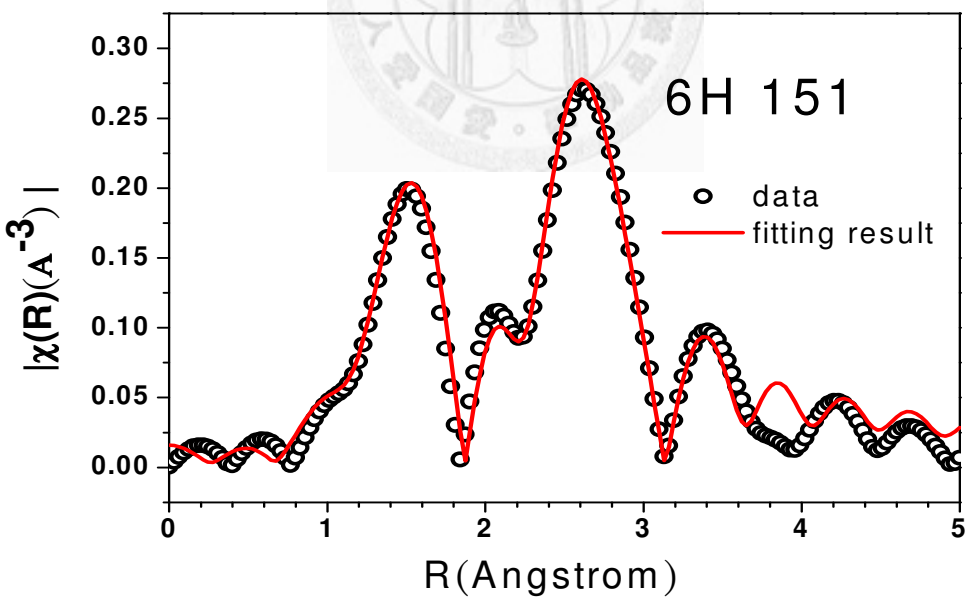

Figure 4.9 *Fourier Transformation spectra of 6H-SiC 151*

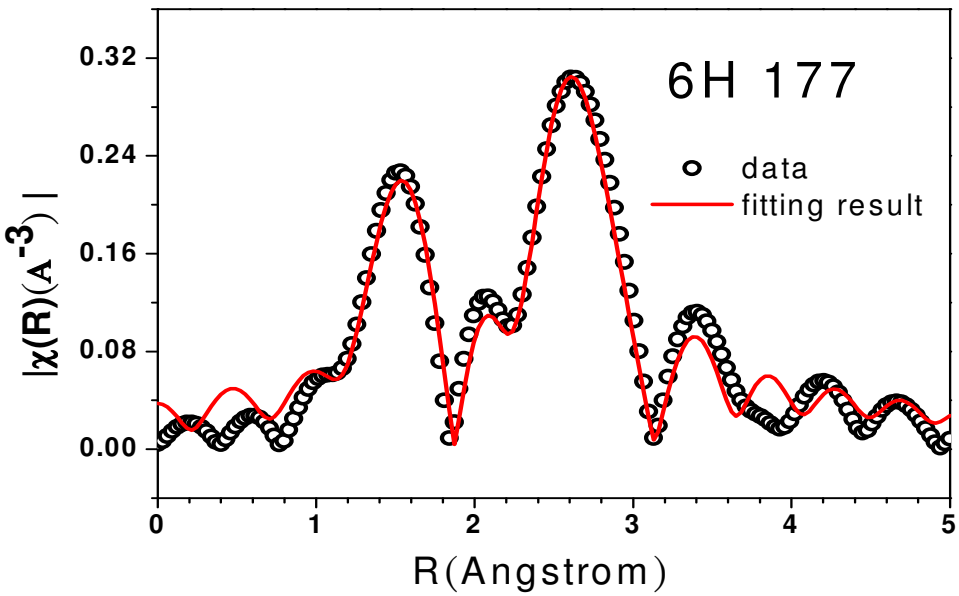

Figure 4.10 *Fourier Transformation spectra of 6H-SiC 177*

As seen in figure 4.8-4.10, and the shell information could be classified. First peak tells us that the position of reflective wave from the nearest atoms, C here. Second peak which is at around 2.7 Angstrom means the second reflective wave from next nearest atoms, Si. By the fitting process from the specific software, the bond length between the absorbing atom and its near atoms could be simulated, as list in table 4.9.

	6H054	6H151	6H177
Si-C Bond length (Angstrom, Å)	1.7729	1.757	1.735
Si-Si Bond length (Angstrom, Å)	3.033	3.058	3.046

Table 4.9 *Statistics of EXAFS fitting in 6H-SiC*

B	F	Cl	Si	C	N
2.051	4.193	2.869	1.916	2.544	3.066

Table 4.10 *The electronegativity*

From table 4.9, the change of bond length is observed. The bond length of Si-C is going to decrease as the doping concentration decreases. From the discussion with Miss Mei Yu Chen, department of physics, National Taiwan Normal Univeristy. The statements she offered were shown below：

As well known, an atom with larger electronegativity bring larger attractive ability to electron. In Table 4.10, take BF_4 and BF_3Cl molecules for example. Most of electron cloud would locate around F atoms due to large electronegativity. When we dope an Cl atom into BF_4 and the molecule become BF_3Cl, the B-F distance increase. The reason is that electronegativity of Cl atom is smaller than F atom. The ionic B-F bond transforms to the covalent B-Cl bond. The electron cloud around B atom changes to bigger. For BF_3Cl molecule, due to electron repulsive force, B-F bond distance will increase. On the other hand, 6H-SiC doping N atom is an opposite situation. Every Si atom surrounds four C atoms and forms a tetrahedron structure. Caused the similar radius of nitrogen and carbon, it has been supposed that nitrogen atom will locate on carbon site. However, the electronegativity of nitrogen is larger than carbons'. This property makes the doping nitrogen atom attracts more electron between Si and N. Nevertheless, Si and other three carbons become more covalent. The covalent bond

between Si and C become stronger due to N doping. It makes the Si-C bond length of tetragon structure become smaller in figure 4.11.

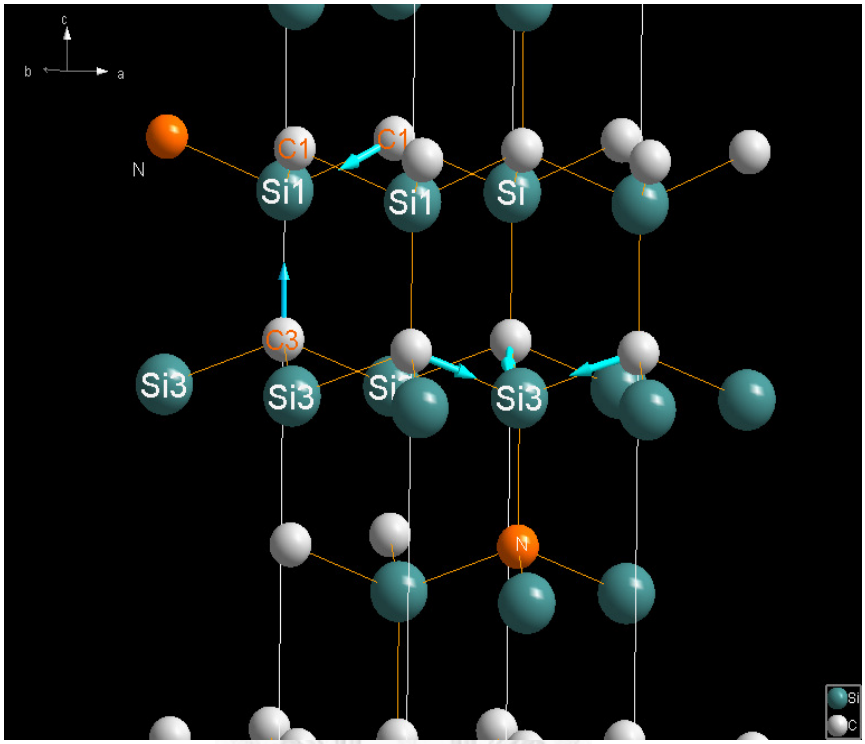

Figure 4.11 *The 6H-SiC crystal structure with doping nitrogen*

However, the situation is not so simple. Differ from the molecule BF_4, SiC form as crystal structure. The Si-C bond length of tetragon decrease, but the three carbons connect four silicon atoms. For instance, from figure 4.11, carbon which marks as C3 move upward and the distance between Si1-C3 become smaller. But the three bond lengths of Si3-C3 become larger. The other carbons which mark C1 have the similar situation. If we take count of all Si-C bond length, the total Si-C distance will increase.

4.2.4 X-ray absorption near edge spectroscopy (XANES)

The XANES spectra at the C K-edge were measured using the total electron yield (TEY) mode at beamline 20A. The TEY detection mode is surface sensitive. The XANES spectra from insulators and semiconductors recorded by TEY mode could be influenced due to charging effect dependent on time, energy, sample thickness, and conductivity. Fig. 4.12 displays the C K-edge XANES spectra of 6H-SiC films at TEY mode.

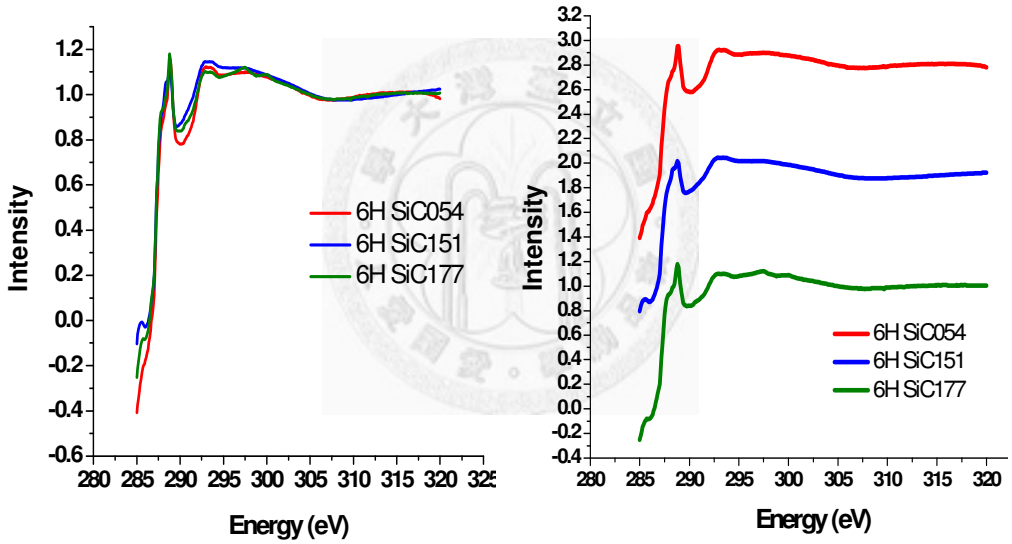

Figure 4.12 C K-edge XANES spectra

The C K-edge XANES of 6H-SiC054, 6HSiC151 and HSiC177 are shown in figure 4.12. It can be seen that all spectra have rich features at energy between 285 and 300 eV, which are assigned to the dipole transitions of C 1s to σ^* from sp3 bonded carbon. The TEY shows a pre-edge peak at 285.5 eV in 6H-SiC. The peak at this region is usually assigned to 1s to π^* transition. As TEY is surface sensitive, the peak may be

due to the presence of defect at surface, in which C is sp2-bonded

4.3 Summary

The Raman and XAFS spectroscopy are combined to analyze a series of N-doped n-type 6H-SiC bulk wafer. The first order Raman transverse optical (TO) and longitudinal optical (LO) phonon modes can be detected at same runs at room temperature by using a high sensitive microscopic system. Synchrotron Radiation X-ray absorption fine-structure has been proved to be a strong spectroscopic analysis technique for the structure information from material. The tender x-ray (around 1700eV) absorption spectroscopy for Silicon K-edge x-ray absorption measurements were employed in NSRRC, Taiwan.

Through combined Raman and XAFS studies, the coincidental result could be obtained. By the Raman spectroscopy, the LO mode intensity become weaker and broaden as the doping concentration increases. This indicates that the crystalline is damaged by the heavy doping concentration. The Raman curves have been fitted by theoretical formulas and the accurate information of the intensity, peak position, and FWHM in each TO and LO modes have been obtained.

Reference

[4.1] Ho Won Jang, Chang Min Jeon, Ki Hong Kim, Jong Kyu Kim, Sung-Bum Bae,

Jung-Hee Lee, Jae Wu Choi, and Jong-Lam Lee, Appl. Phys. Lett. vol 81, num 7, 1249, (2002).

[4.2] Y. F. Wu, B. P. Keller, S. Keller, D. Kalponek, P. Kozodoy, S. P. DenBaas, and U. K. Mishra, Appl. Phys. Lett, 69, 1438 (1996).

[4.3] N. Maeda, T. Saitoh, K. Tsubaki, T. Nishida, and N. Kobayashi, Jpn. J. Appl. Phys., Part 2 38, L799 (1999).

[4.4] T. Egawa, H. Ishikawa, M. Umeno, and T. Jimbo, Appl. Phys. Lett, 76, 121 (2000).

[4.5] Cho, Kai-Sin, " Spin-dependent properties of two-dimensional AlGaN/GaN electron systems", Graduate Institute of Physics College of Science, National Taiwan University, Doctoral Dissertation (2007).

[4.6] K. B. Lee, P. J. Parbrook, T. Wang, F. Ranalli, T. Martin, R. S. Balmer, and D. J. Wallis, "Optical investigation of exciton localization in $Al_xGa_{1-x}N$", J. Appl. Phys. 101, 053513 (2007).

[4.7] Lee, Zhen-Sheng, "Optical Properties of InGaN/GaN Multi-Quantum Wells Structure Grown by Metalorganic Chemical Vapor Deposition", Graduate Institute of Photonics and Optoelectronics, National Taiwan University, Master Thesis (2007).

[4.8] S.S. Hullavarad, N.V. Hullavarad, D.E. Pugel, S. Dhar, T. Venkatesan, R.D.

Vispute, "Structural and chemical analysis of pulsed laser deposited $Mg_xZn_{1-x}O$ hexagonal (x = 0.15, 0.28) and cubic (x = 0.85) thin films." , Optical Materials 30, 993-1000, (2008).

[4.9] S. Nakamura, M. Senoh, and T. Mukai, Jpn. J. Appl. Phys., Part 2 30, L1708 (1991).

[4.10] S. Nakamura, M. Senoh, S. Nagahama, N. Iwasa, T. Yamada, T. Matsushita, T. H. Kiyoku, Y. Sugimoto, T. Kozaki, H. Umemoto, M. Sano, and K. Chocho, Appl. Phys. Lett. 72, 2014 (1998).

[4.11] T. Mukai, H. Narimatsu, and S. Nakamura, Jpn. J. Appl. Phys., Part 2 37, L479 (1998).

[4.12] M. Khan, J. N. Kusnia, D. T. Olson, G. M. Van Hove, M. Blasingane, and L. F. Reitz, Appl. Phys. Lett. 60, 2917 (1992).

[4.13] D. Walker, X. Zhang, P. Kung, A. Saxler, S. Javadpour, J. Xu, and M. Razeghi, Appl. Phys. Lett. 68, 2100 (1996).

[4.14] 6 K. Ito, K. Hiramatsu, H. Amano, and I. Akasaki, J. Cryst. Growth 104, 533 (1989).

[4.15] S. J. Chung, M. Senthil Kumar, H. J. Lee, and E.-K. Suh, J. Appl. Phys., Vol 95, Num 7, 3565, (2004).

[4.16] S. Choopun, R.D. Vispute, W. Yang, R.P. Sharma, T. Venkatesan, H. Shen,

Appl. Phys. Lett. 80, 1529 (2002).

[4.17] A. Ohtomo, M. Kawasaki, T. Koida, K. Masubuchi, H. Koinuma, Appl. Phys. Lett. 72, 2466 (1998).

[4.18] C.W. Teng, J.F. Muth, U. Ozgur, M.J. Bergmann, H.O. Everitt, A.K. Sharma, C. Jin, J. Narayan, Appl. Phys. Lett. 76, 979. (2000)

[4.19] J. Chen, W.Z. Shen, N.B. Chen, D.J. Qiu, H.Z. Wu, J. Phys. Condens. Matter 15 L475, (2003)

[4.20] N.B. Chen, C.H. Sui, Materials Science and Engineering B 126 16–21 (2006).

[4.21] Lijia Liu, Y. M. Yiu, and T. K. Sham ,Liying Zhang and Yafei Zhang* J. Phys. Chem. C, 114, 6966 (2010)

Chapter 5 Optical Study of InGaN/GaN Multi-quantum Wells Structures Light Emitting Diode

5.1 Sample Information

The epitaxial growth of $In_xGa_{1-x}N$/GaN MQWs on sapphire (Al_2O_3) substrates, labeled as L36, L46, L47, L48 and L52, were performed by metal organic chemical vapor deposition (MOCVD). Trimethylgallium (TMGa), trimethylindium (TMIn), and ammonia (NH_3) were used as precursors for Ga, In, and N, respectively. The carrier gas was H_2 and N_2, respectively, for the growth of GaN and InGaN. For the growth procedures, the substrates are initially treated in H_2 ambient at 1173 ^oC, followed by the growth of a low-temperature (550 ^oC) GaN buffer layer and a layer of nominally undoped GaN grown at low temperature (850 ^oC) under low pressure. Afterwards, the temperature was lowered to grow eight periods of InGaN/GaN quantum wells layer. Finally, p-type GaN with thickness around 250 nm was been growth. Figure 5.1 shows the schematic drawing of the samples.

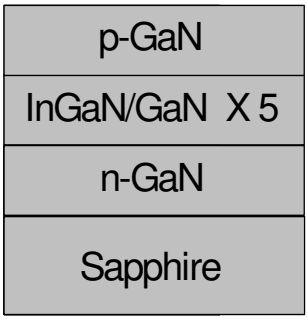

Figure 5.1 *Structures of the InGaN/GaN MQWs.*

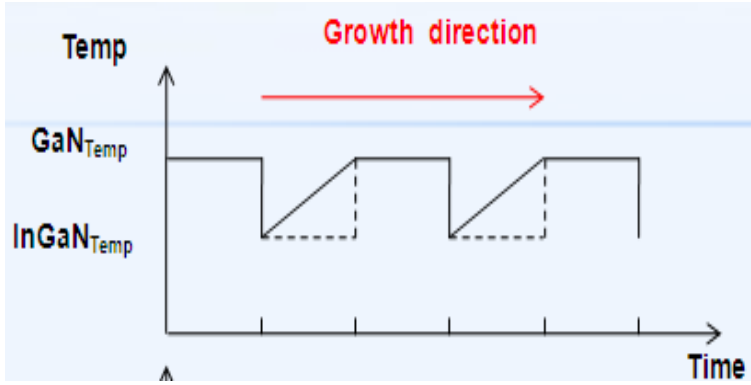

Figure 5.2 *Growth direction of L46,L47,L48*

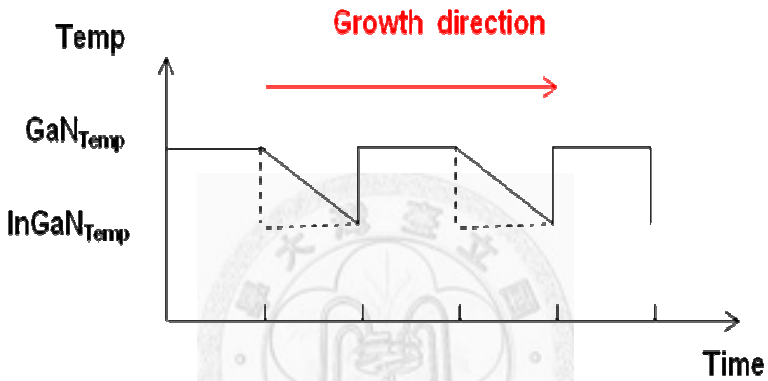

Figure 5.3 *Growth direction of L52*

5.2 Optical Measurement and analysis

5.2.1 PL Experimental Results

Fig 5.4 shows the normalized PL intensity spectra of samples L36, L46, L47, L48 and L52 at room temperature. The band gap energies related to the radiative recombination of excitons confined in the general MQWs of samples L36, L46, L47, L48 and L52 are 2.71 eV, 2.84, 2.62, 2.80 and 2.93 eV, respectively. The calculation was performed assuming that the InGaN band gap energy depends on the indium composition as $E_g^{InGaN}(x) = E_g^{InN}x + E_g^{GaN}(1-x) - bx(1-x)$ (eV), where b(x) is the variable bowing

parameter, which depends on x [5.1, 5.2].

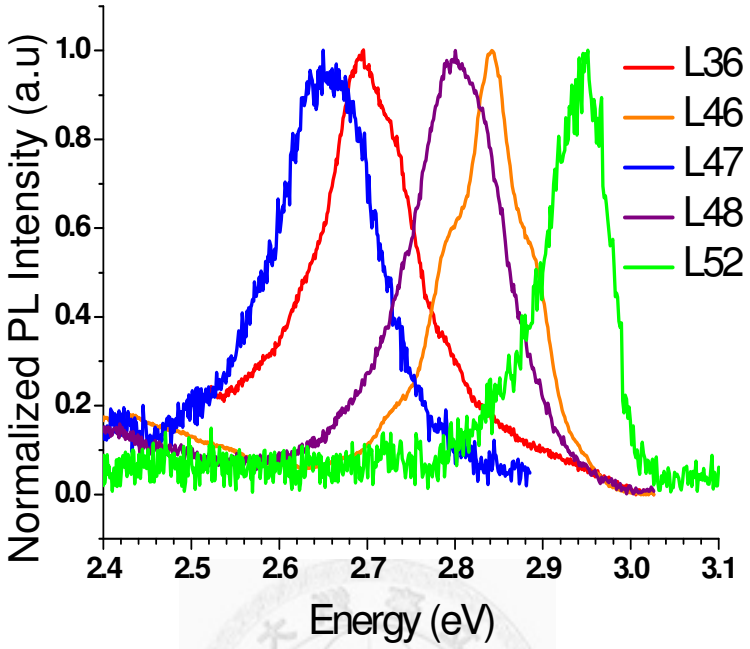

Figure 5.4 *The room-temperature PL spectrum of InGaN MQWs for the sample L36, L46, L47, L48 and L52. The spectrum is normalized.*

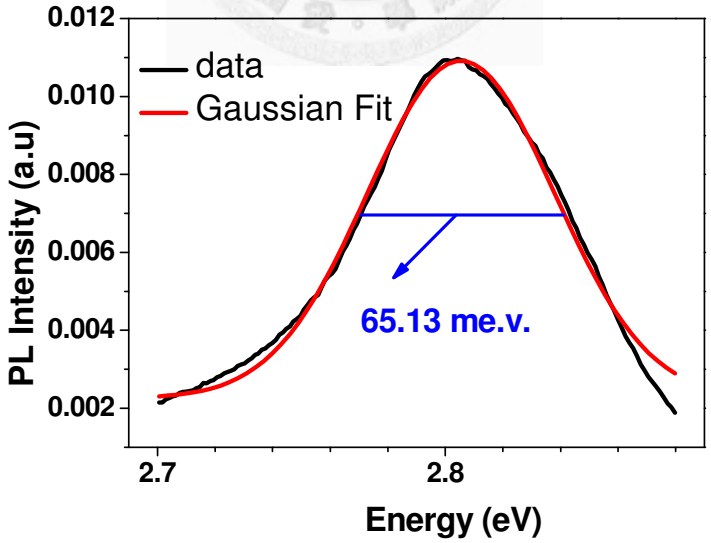

Figure 5.5 *The room-temperature PL FHWM spectrum*

Figure 5.6 (a), (b), (c), (d) and (e) shows the PL spectra of the sample L36, L46, L47, L48 and L52, respectively, over a temperature range from 10 to 300 K. All spectra are normalized to have nearly the same intensity. And we use waterfall to watch the trend of different temperature. These spectra show a multi-peak emission, which the QW-related energy peak. Because the Fabry-Perot effect, we can hardly indicate the peak position directly.

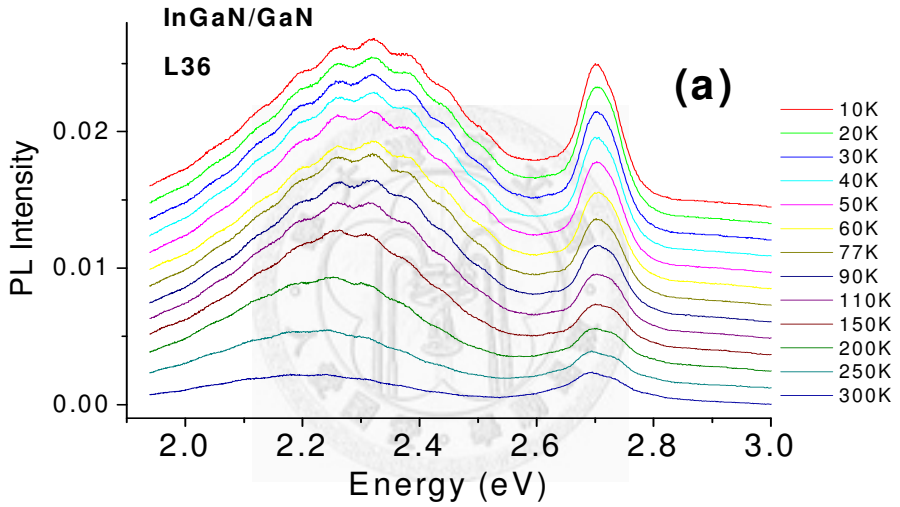

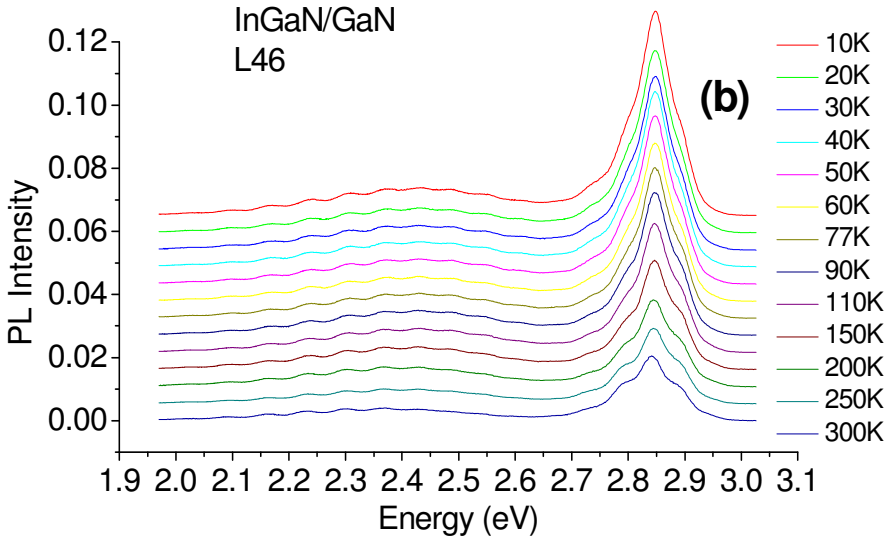

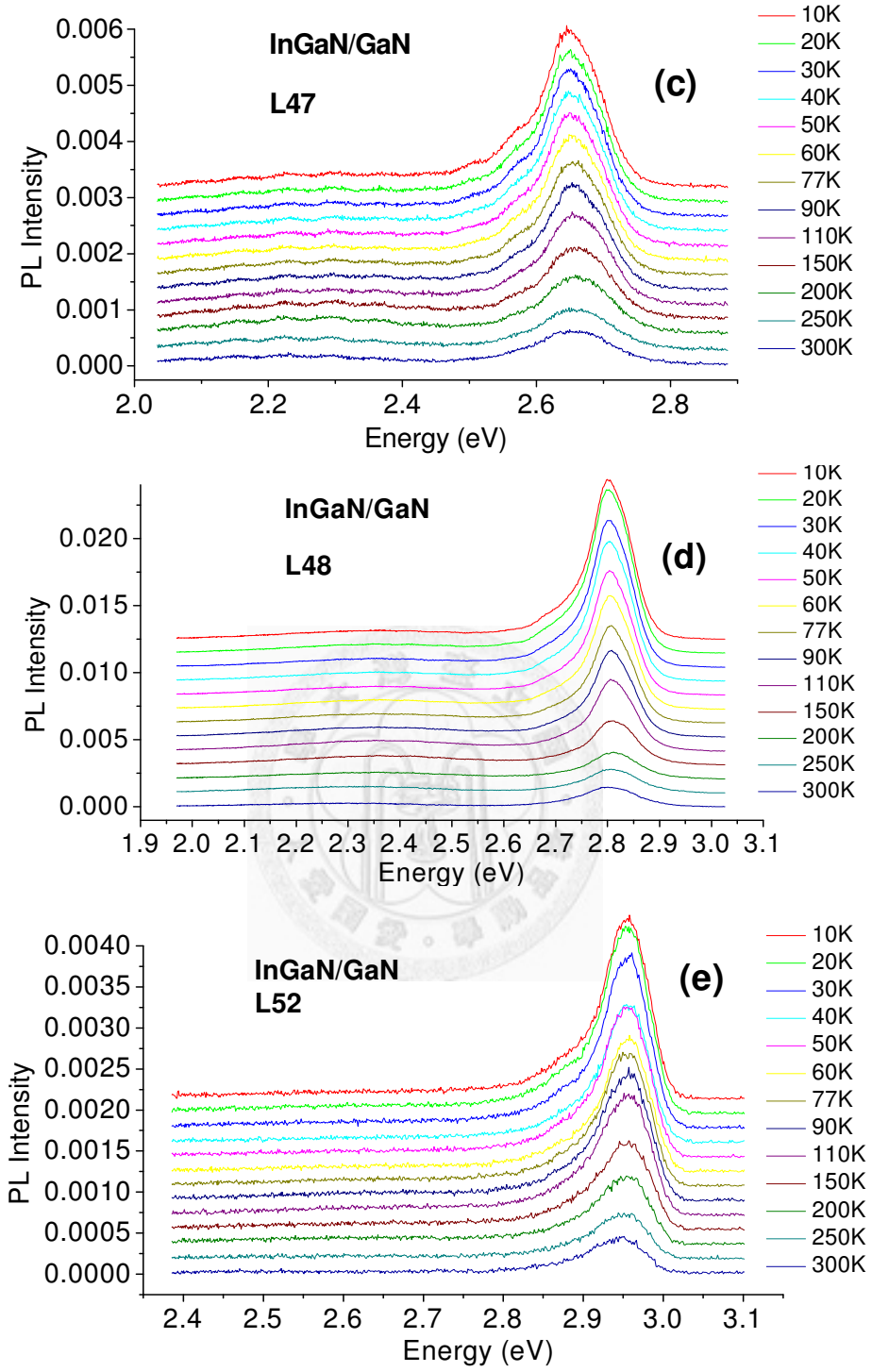

Figure 5.6 *The PL spectra for the InGaN/GaN MQW structures in the temperature range from 10 to 300 K. (a)L36, (b)L46, (c)L47, (d)L48 and (e)L52.*

In order to indicate the exact InGaN photoluminescence (PL) peak position we use Gaussian fit to fit the QW-related energy peak. Figure 5.7 gives the PL peak position of the QW-related emission as a function of temperature. The peak positions of these samples were evaluated by fitting of the PL spectra with Gaussian curves. We can find that the energy band gap of semiconductors tends to decrease in increasing temperature. As temperature increases from 10 to 300 K, the PL peak energy of sample L36 decreases from 2.708 eV to 2.702 eV, the PL peak energy of sample L46 decreases form 2.845 eV to 2.837 eV, the PL peak energy of sample L47 decreases form 2.657 eV to2.655 eV, the PL peak energy of sample L48 decreases form 2.803 eV to 2.801 eV and the PL peak energy of sample L52 decreases form 2.957 eV to 2.949 eV. This behavior can be better understood if one considers that the interatomic spacing increases when the amplitude of the atomic vibrations increases due to the increased thermal energy. This effect is quantified by the linear expansion coefficient of a material. An increased interatomic spacing decreases the average potential seen by the electrons in the material, which in turn reduces the size of the energy band gap. The unusual dependence of the dominant PL peak could be explained by a carrier transfer between different localized states with temperature increasing.

Valuable information can also be learned from studying the luminescence intensity as a function of temperature. This is because the luminescence intensity correlates with the

efficiency of the conversion of excited carriers into luminescence in the structures. By comparing efficiencies between different samples, we may be able to understand the competition between radiative and non-radiative recombination in the QW structure.

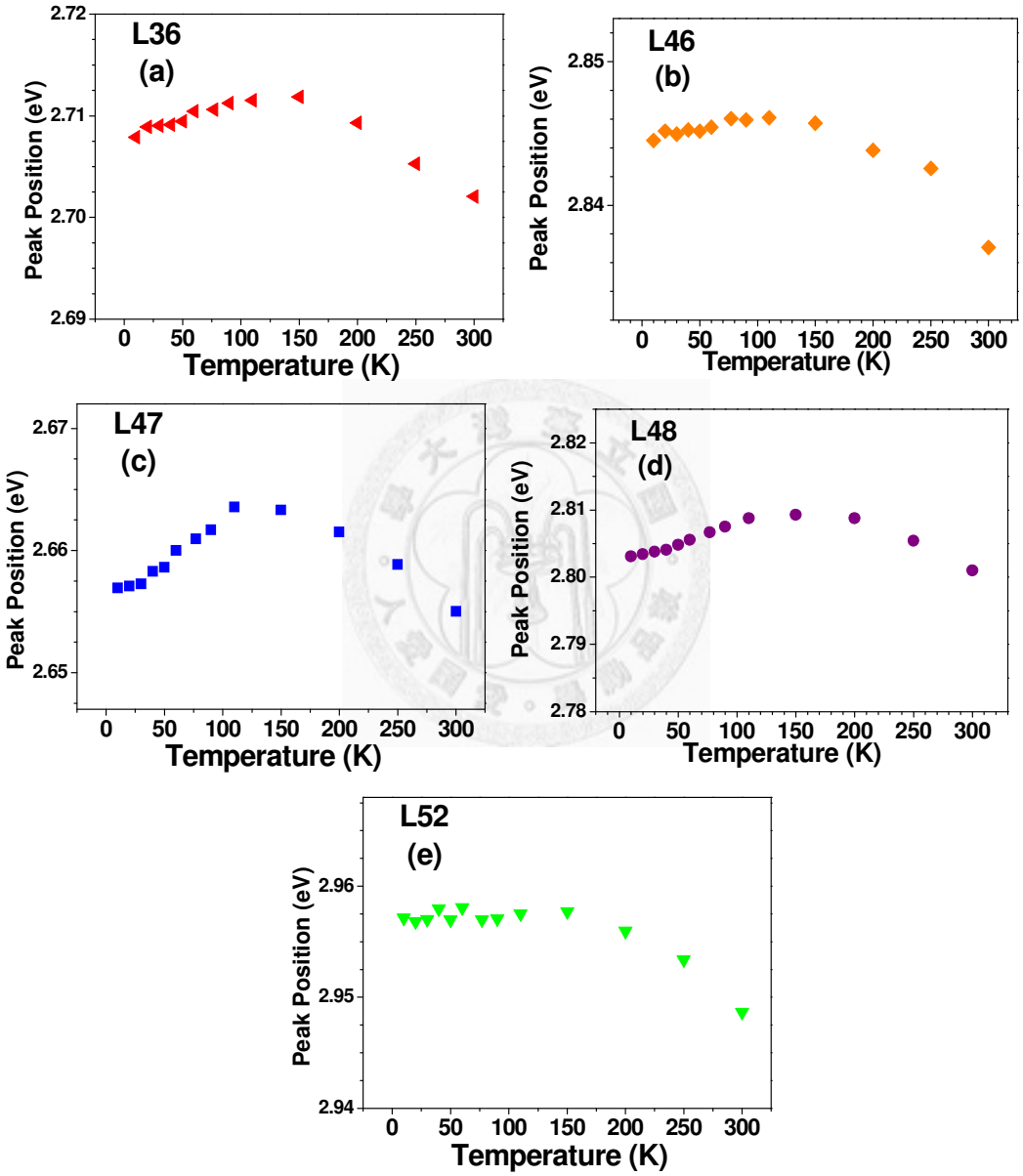

Figure 5.7 *Temperature dependence of the peak position of the QW-related emission for the InGaN/GaN blue LED structure (a)L36, (b)L46, (c)L47, (d)L48 and (e)L52.*

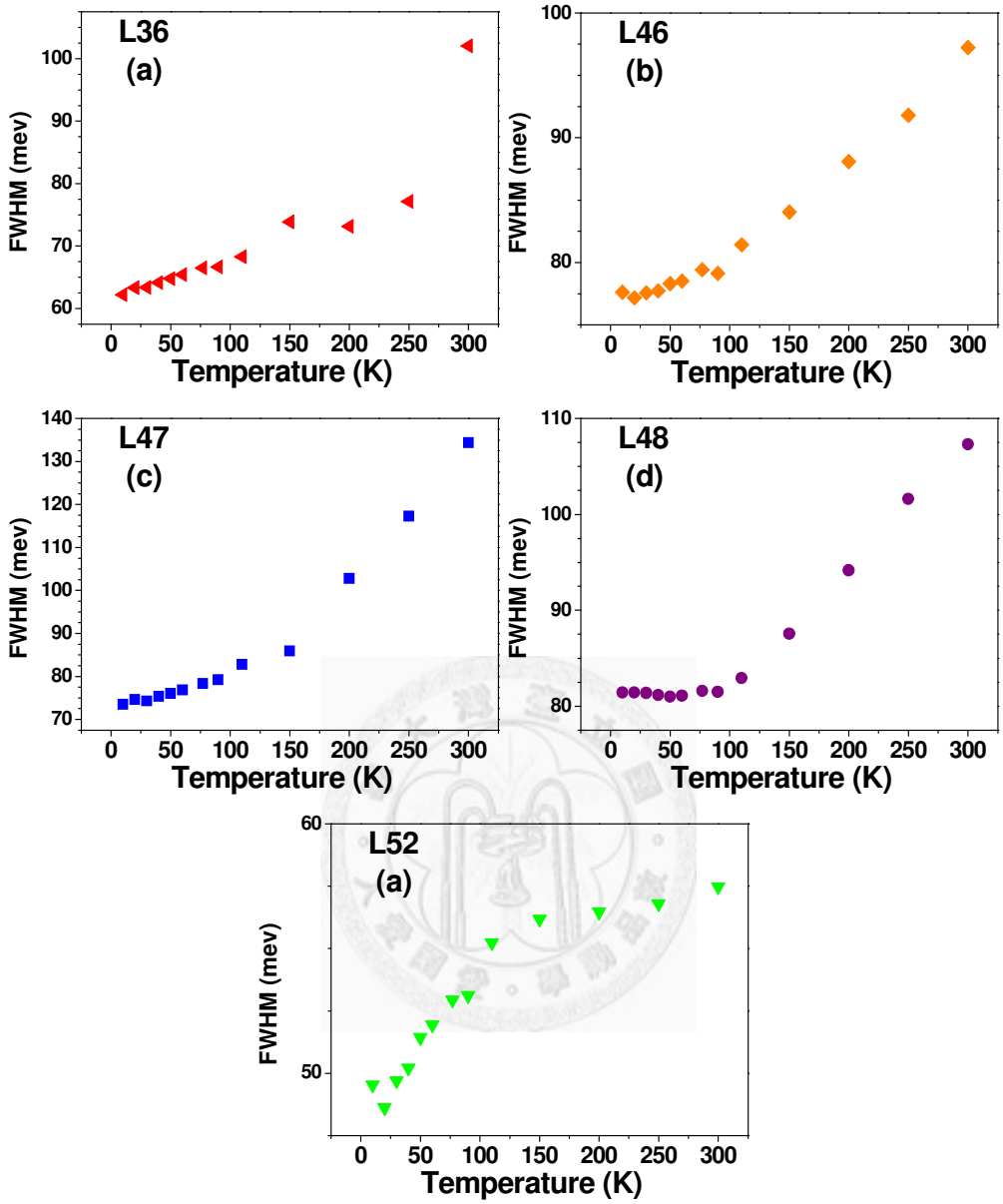

Figure 5.8 *Temperature dependence of the FWHM PL peak intensity of the QW-related emission for the InGaN/GaN blue LED structure (a)L36, (b)L46, (c)L47, (d)L48 and (e)L52.*

In such a compound, the PL intensity always decays with temperature due to the increasing nonradiative recombination. Such an anomalous phenomenon can be

attributed to carrier supply with thermal energy. With thermal energy, carriers can overcome certain potential barriers and relax into localized states formed by the InGaN clusters. We believe that there is a very complicated localization-state system for the QW structure of the sample L36, L46, L47, L48 and L52. And with increasing temperature, carriers can obtain enough thermal energy to relax into the localized states. Therefore, the localized states gradually dominate the emission at higher temperature and the FWHM increases with temperature (see figure 5.8).

5.2.2 Activation energy

Generally, the internal quantum efficiency can be evaluated by the temperature dependence of the integrated PL intensity [5.7, 5.8]. An Arrhenius plot of the normalized integrated PL intensity for the InGaN-related PL emission over the temperature range under investigation was displayed in Figure 5.9. The analysis of these data had been carried out using well-known thermal activation relation [5.9]:

$$I_{PL}(T) = \frac{I_0}{1 + Ae^{(\frac{-E_a}{K_B T})}} \tag{5.1}$$

Where A the constant, Ea the activation energy, and k_B the Boltzmann's constant. At a temperature range from 10 to 300 K, the integrated PL intensity is thermally activated with the activation energy. The activation energies obtained from equation (5.1) were listed in table 5.1. It has been suggested that the measured activation energy Ea in

InGaN samples represents the localization energies of excitons, resulting from band edge fluctuations. So we can infer that the thinner barrier width resulted in higher localization effect owing to the formation of In-rich QDs structure.

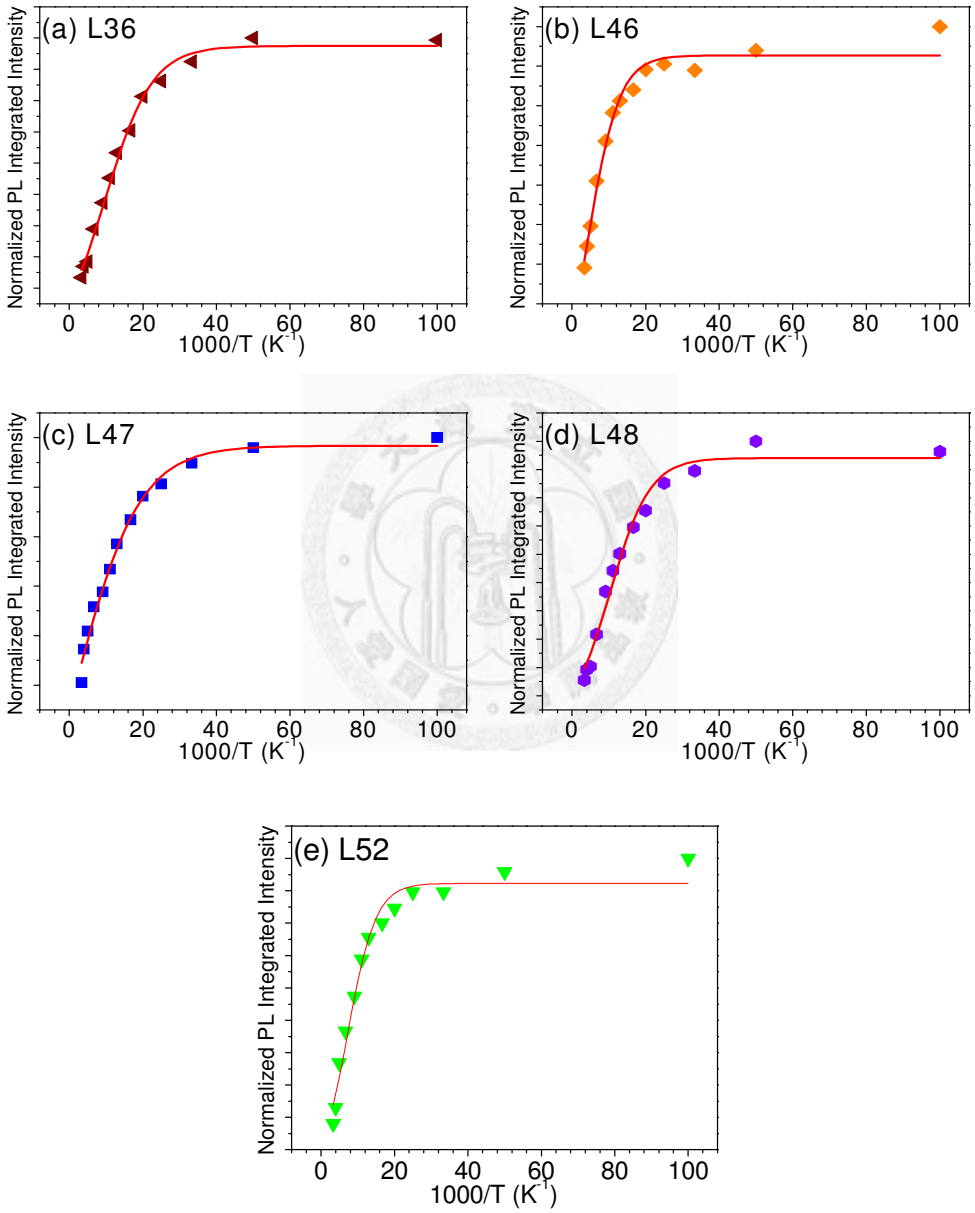

Figure 5.9 *Arrhenius plot of the normalized integrated PL intensity (I_{PL}) versus temperature for the InGaN/GaN MQW structure(a)L36, (b)L46, (c)L47, (d)L48 and*

(e)L52. Experimental data are represented by the solid squares; the red line is a fitting curve.

Samples	E_a (meV)
L36	13.57
L46	20.21
L47	9.85
L48	16.2
L52	22.78

Table 5.1 *Activation energy (E_a) obtained from equation (5.1)*

5.2.3 Photoluminescence Excitation Experimental Results

Figure 5.10-5.14 summarizes the PL and PLE of the InGaN/GaN MQWs of sample L36, L46, L47, L48 and L52 at the temperature of room temperature.

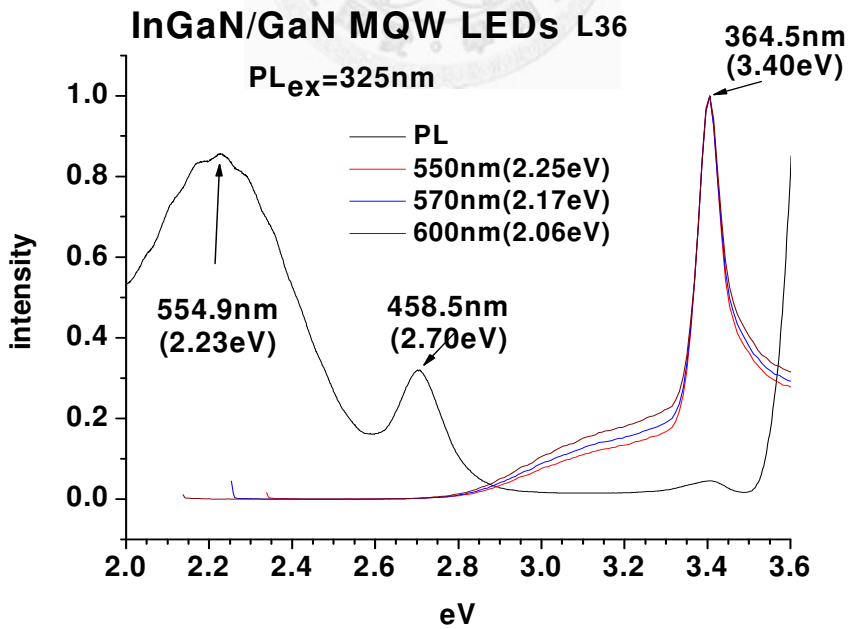

Figure 5.10 *RTPL and PLE spectra of L36*

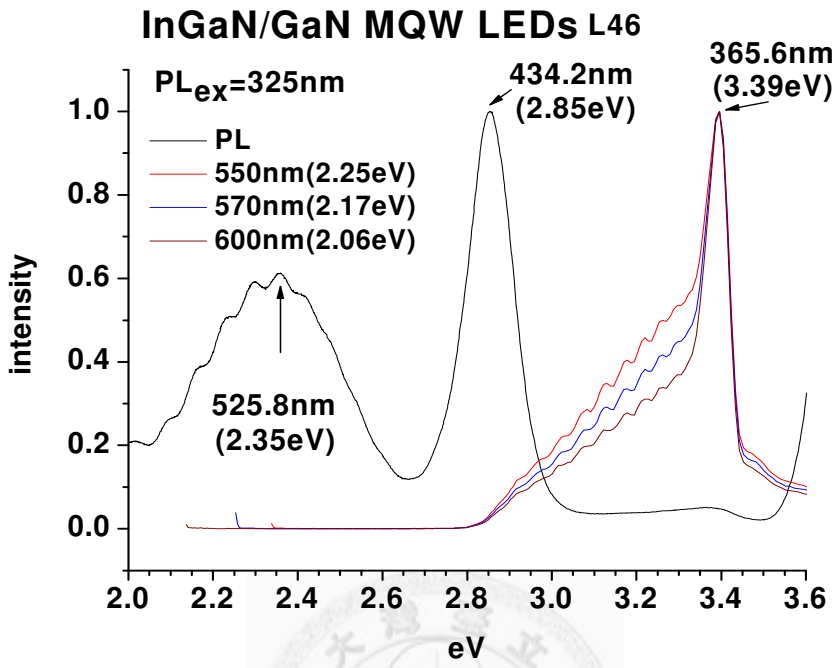

Figure 5.11 *RTPL and PLE spectra of L46*

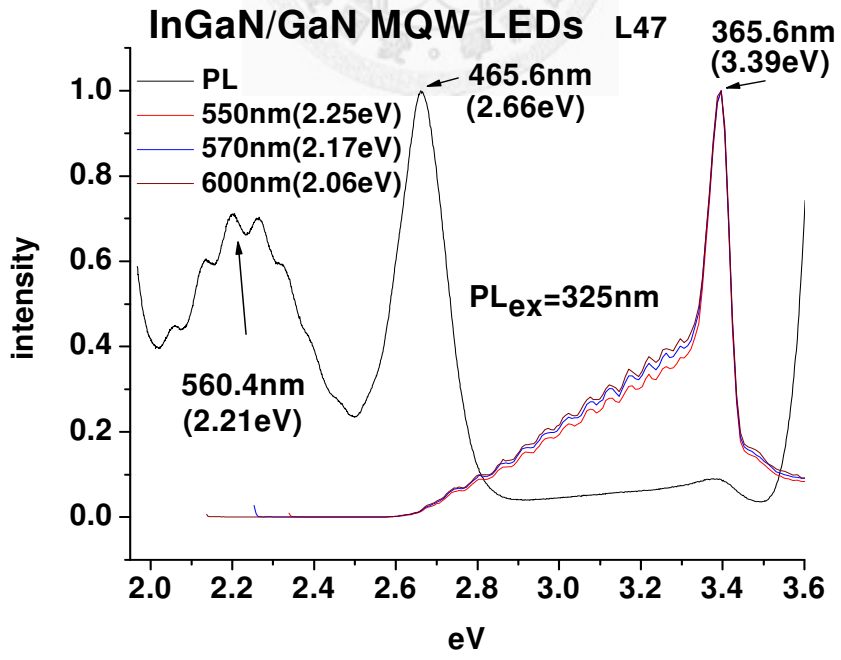

Figure 5.12 *RTPL and PLE spectra of L47*

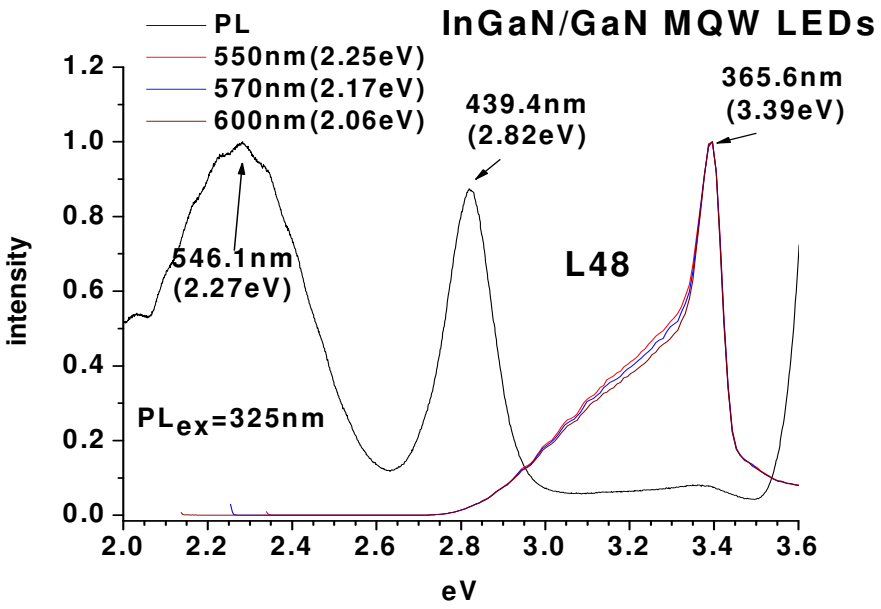

Figure 5.13 *RTPL and PLE spectra of L48*

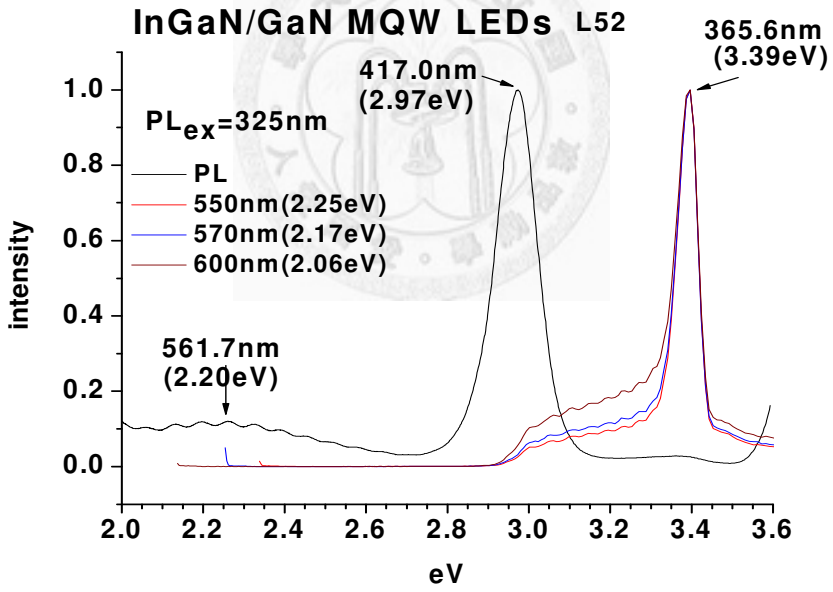

Figure 5.14 *RTPL and PLE spectra of L52*

Photoluminescence excitation (PLE) can provide the information of absorption spectrum and understand the energy state distribution. In order to analyze the Stokes' shift, which is defined as the difference in energy between the effective band gap and

the emission peak energy, it is essential to have an accurate description of the absorption edge that includes the effects of broadening. A PLE measurement was performed to get the absorption edge. Martin *et al.* suggested that by fitting the PLE spectra to sigmoidal formula:

$$\alpha = \frac{\alpha_0}{1+\exp(\frac{E_{eff}-E}{\Delta E})} \tag{5.2}$$

Where α_0 the constant, E_{eff} the effective band gap, and ΔE the broadening parameter which indicates a distribution of absorption states, and E the excitation energy at which the intensity of emission.

5.2.4 TRPL experimental results

We performed TRPL measurements at 10K for different detection energy (E_{detect}) to clarify the temporal dynamics of the luminescence. To further clarify the emission properties of InGaN/GaN MQWs, figure. 5.15 (a), (b), (c), and (d) shows the PL decay profiles for the sample L36,L46, L47, and L48 , respectively. The sample L36 measured TRPL (10K) with detecting wavelength at λ = 445.2, and 459.2 nm, respectively (see Fig 5.15 (a)). And the sample L46 detecting wavelength at λ = 433.6, and 445.6 nm, respectively (see Fig 5.15 (b)). And the sample L47 detecting wavelength at λ = 447, and 471 nm, respectively (see Fig 5.15 (c)). And the sample L48 detecting wavelength at λ = 425.2, 445.2 and 500 nm, respectively (see Fig 5.15 (d)).

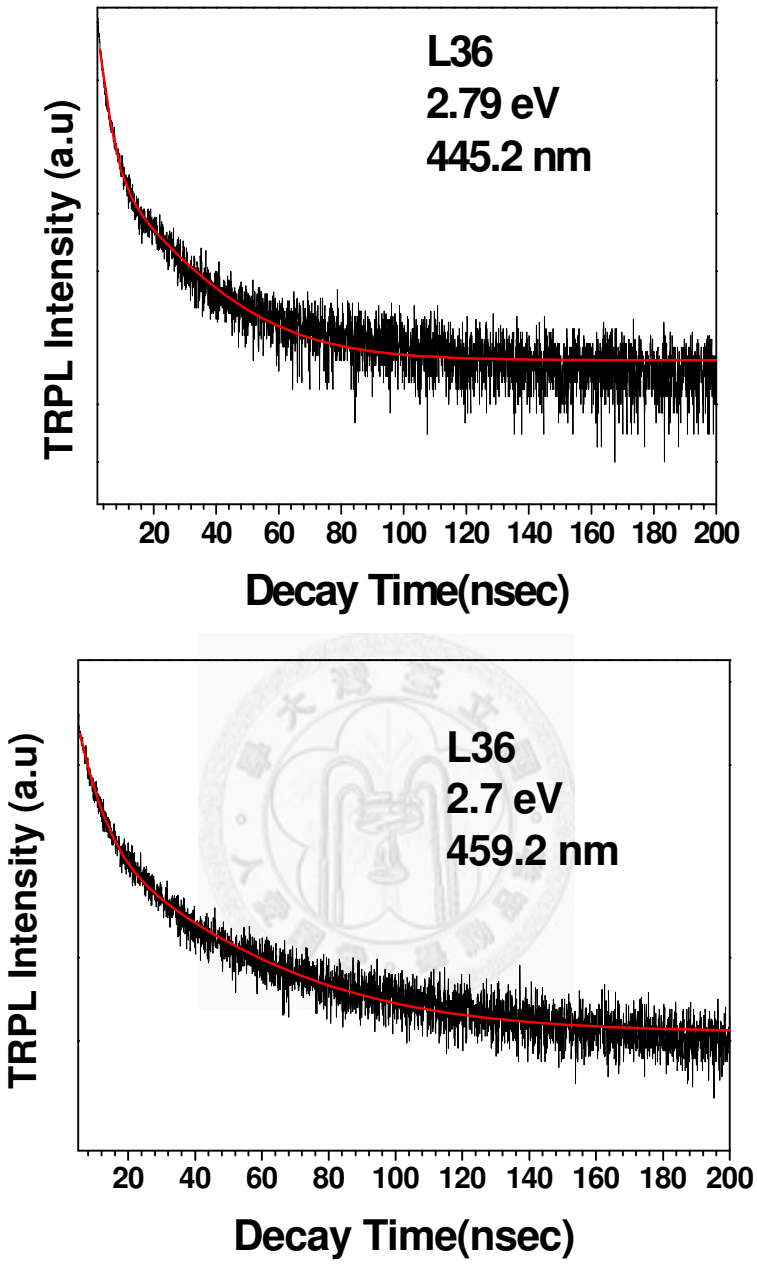

Figure 5.15 *(a) Measured TRPL (10K) for the InGaN/GaN MQW LED structure (L36) with detecting wavelength at λ= 445.2, and 459.2 nm, respectively. The red curve is a single exponential function fit.*

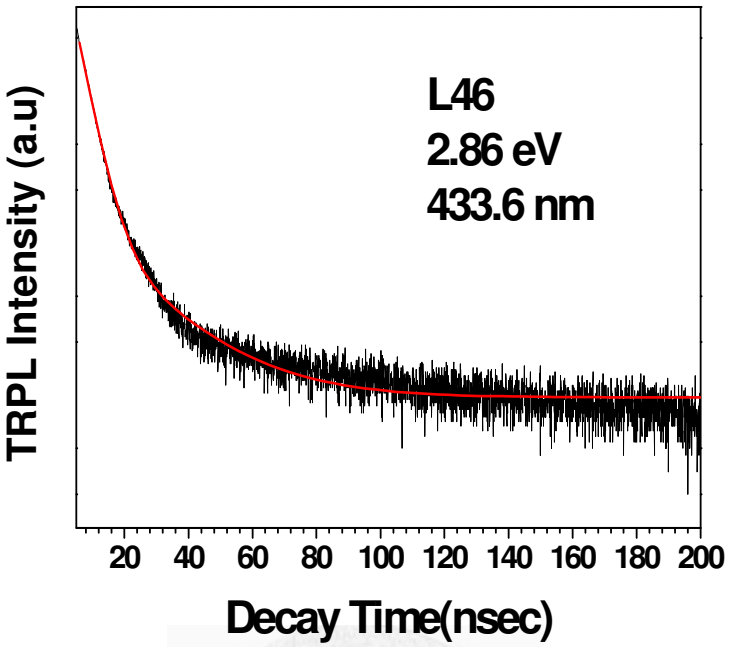

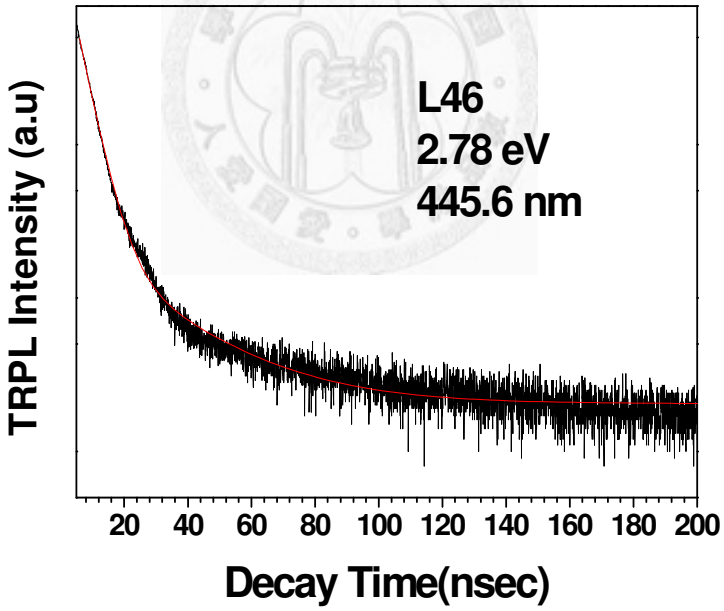

Figure 5.15 *(b) Measured TRPL (10K) for the InGaN/GaN MQW LED structure (L46) with detecting wavelength at λ= 433.6, and 445.6 nm, respectively. The red curve is a single exponential function fit.*

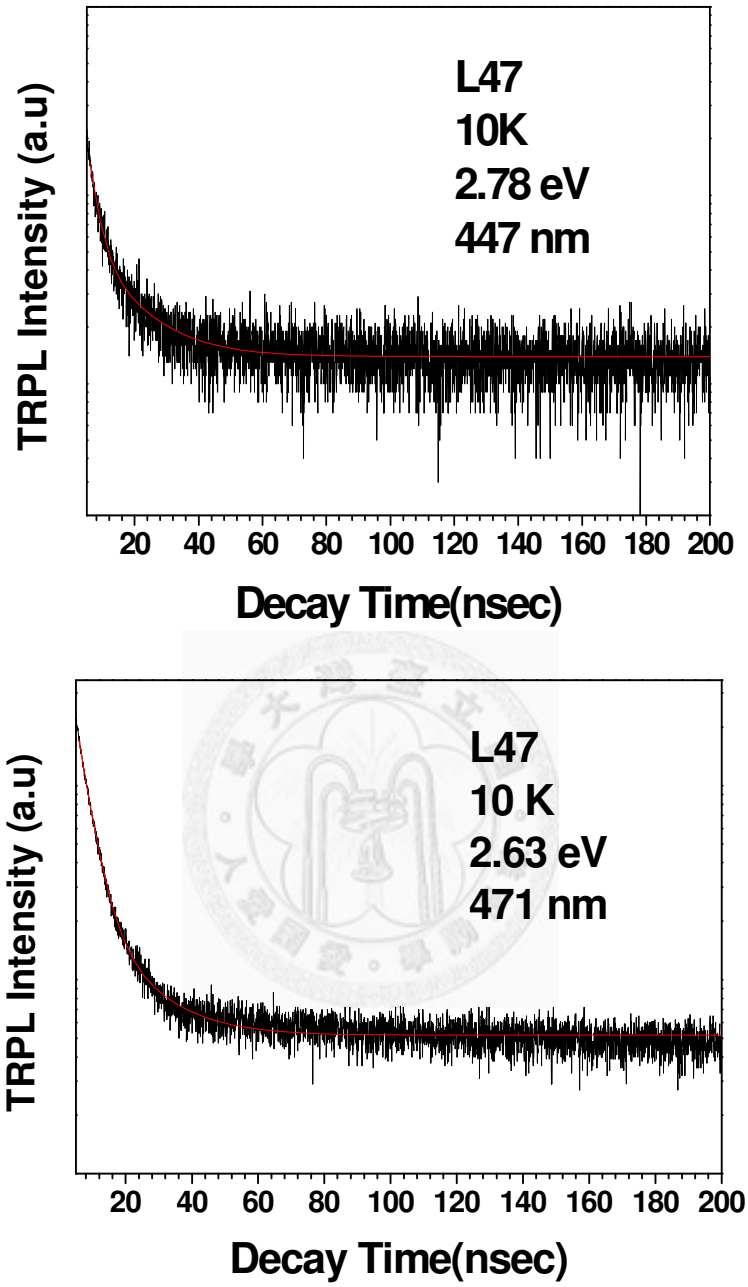

Figure 5.15 *(c) Measured TRPL (10K) for the InGaN/GaN MQW LED structure (L47) with detecting wavelength at λ= 447, and 471 nm, respectively. The red curve is a single exponential function fit.*

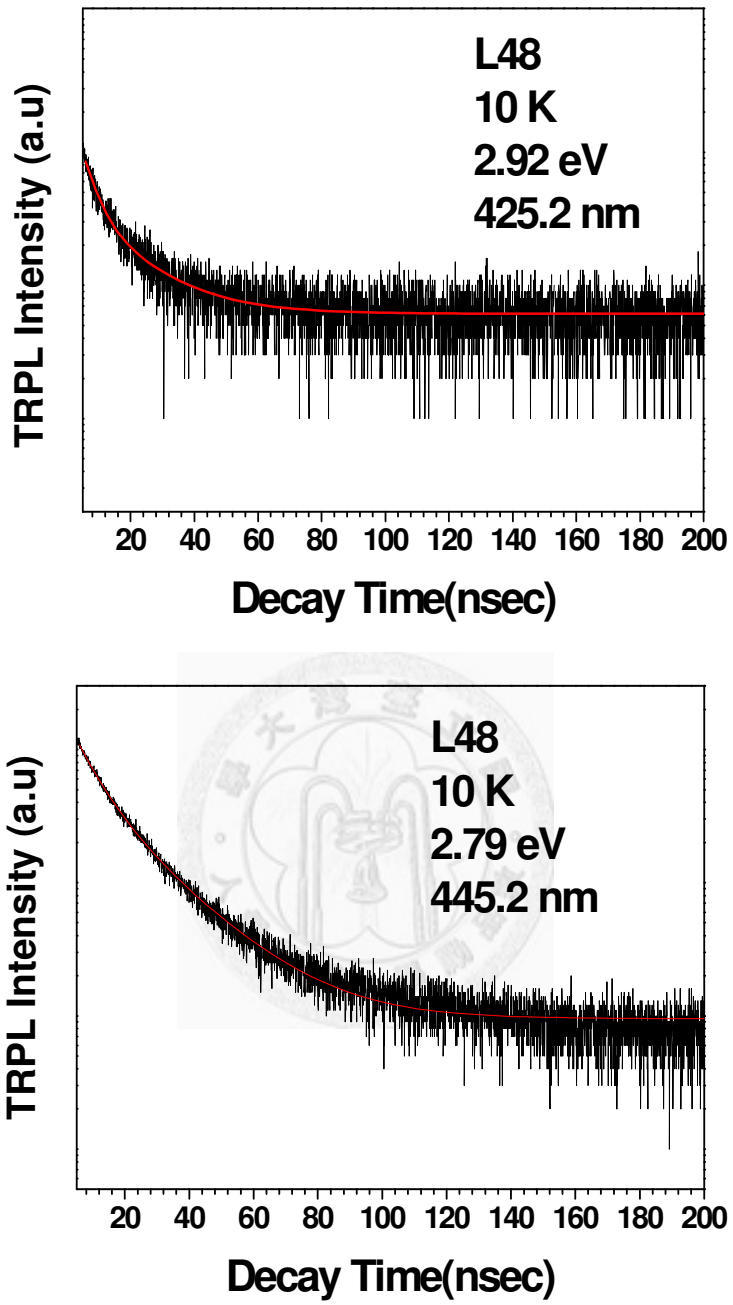

Figure 5.15 *(d) Measured TRPL (10K) for the InGaN/GaN MQW LED structure (L48) with detecting wavelength at λ= 425.2, and 445.2 nm, respectively. The red curve is a single exponential function fit.*

The low temperature (10K) TRPL of the samples were all measured. The photon energy dependence of τ_{PL} at 10K is shown in figure 5.16 (a), (b), (c), and (d) for the sample L36, L46, L47, and L48. The PL has a main peak around 2.71, 2.85, 2.66, and 2.81 eV for the sample L36, L46, L47 and L48, respectively. The PL decay time was dependent on the emission photon energy and shorter on the higher energy side (2.68 ns) than that on the lower energy side (5.93 ns) for L36 and the main emission decay time about 5.45 ns; shorter on the higher energy side (2.73 ns) than that on the lower energy side (4.43 ns) for L46 and the main emission decay time about 4.1 ns ; shorter on the higher energy side (2.2 ns) than that on the lower energy side (4.04 ns) for L47 and the main emission decay time about 3.65 ns; shorter on the higher energy side (3.01 ns) than that on the lower energy side (7.69 ns) for L48 and the main emission decay time about 6.47 ns. In other words, the τ_{PL} values increase with decreasing photon energy in five samples. This energy dependence was due to the energy transfer from higher energy localized state to lower one. This is characteristic of the localized system, where in the decay of excitons consists of both radiative recombination and the transfer process to tail states. The depth of localization can be evaluated by assuming the exponential distribution of the density of tail states and by fitting the photon energy dependence of the τ_{PL} values using the following equation [5.11-5.15]:

$$\tau_{PL}(E) = \frac{\tau_{rad}}{1 + \exp\frac{E - E_{me}}{E_0}} \tag{5.3}$$

Where τ_{rad}, E_{me}, and E_0 are the radiative lifetime, the energy similar to the mobility edge, and the depth of localization, respectively.

The radiative lifetime, the energy similar to the mobility edge, and the depth of localization obtained from equation (5.3) were listed in table 5.2. By fitting, τ_{rad} = 6.51 ns, E_{me} = 2.76 eV, and E_0 = 47.89 meV were obtained for the sample L36, while τ_{rad} = 4.47 ns, E_{me} = 2.98 eV, and E_0 = 58.76 meV were obtained for the sample L46; while τ_{rad} = 4.22 ns, E_{me} = 2.77 eV, and E_0 = 80.37 meV were obtained for the sample L47, while τ_{rad} = 7.76 ns, E_{me} = 2.92 eV, and E_0 = 79.51 meV were obtained for the sample L48. The lifetime at the low-energy side of the InGaN peaks is longer for thicker barrier width.

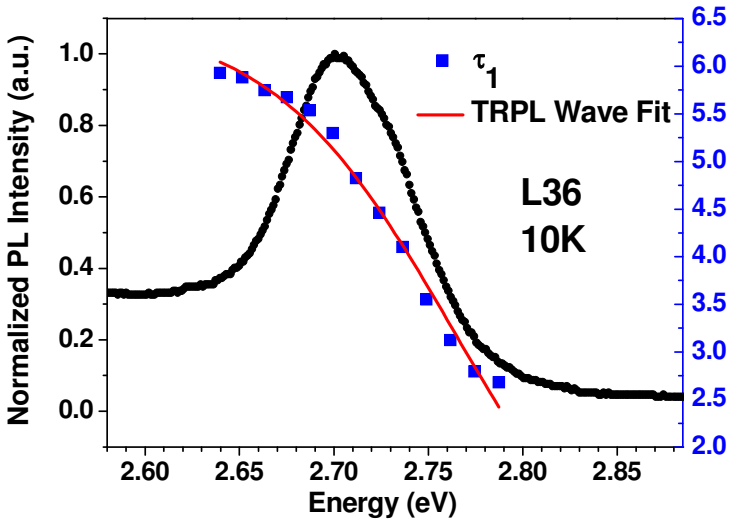

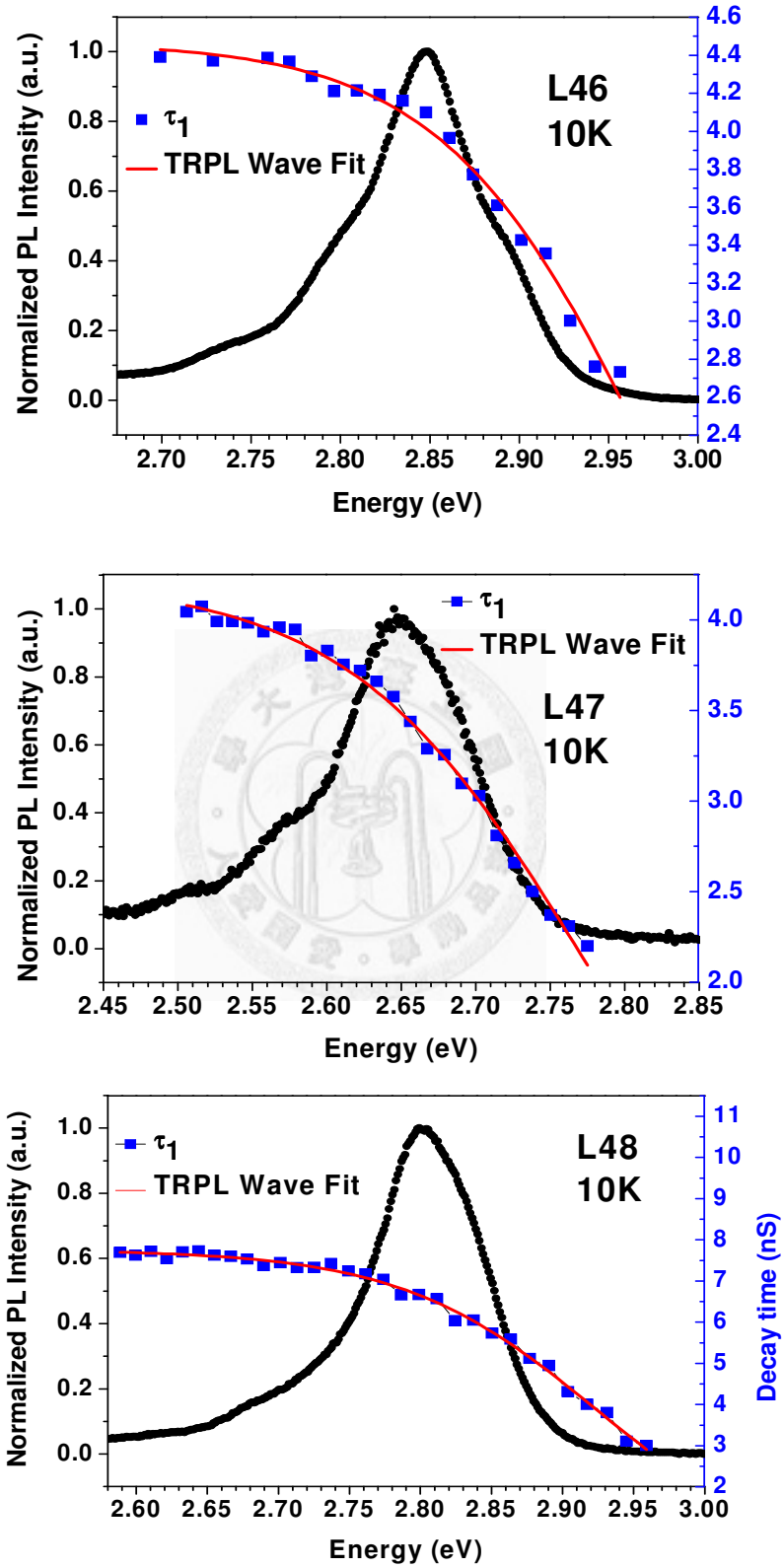

Figure 5.16 *Photon energy dependence of PL lifetime τ_{PL} for the InGaN/GaN MQW (a) L36, (b) L46, (c) L47, and (d) L48 at 10K.*

Sample name	τ_{rad} (ns)	E_{me} (eV)	E_0 (meV)
L36	6.51	2.76	47.89
L46	4.47	2.98	58.76
L47	4.22	2.77	80.37
L48	7.76	2.92	79.51

Table 5.2 *Radiative lifetime, the energy similar to the mobility edge, and the depth of localization (τ_{rad} , E_{me} , and E_0) obtained from equation (5.3)*

The temperature dependence of decay time (τ) in the temperature range from 10K to 300 K is shown in figure 5.17 (a), (b), (c), and (d) for the sample L36, L46, L47, and L48. The PL decay time was dependent on the temperature and shorter on the higher temperature (300k) side (4.291 ns) than that on the lower temperature (10k) side (5.303 ns) for L36 and the highest decay time at 30k was about 5.53 ns; shorter on the higher temperature (300k) side (3.208 ns) than that on the lower temperature (10k) side (4.098 ns) for L46 and the highest decay time at 30k was about 4.22 ns; shorter on the higher temperature (300k) side (3.232 ns) than that on the lower temperature (10k) side (3.576 ns) for L47 and the highest decay time at 30k was about 3.78 ns; shorter on the higher temperature (300k) side (4.663 ns) than that on the lower temperature (10k) side (6.7 ns) for L48 and the highest decay time at 30k was about 7.03 ns. From the figure, the decay time (τ) values slightly increase till temperature 30k or 50K and decrease while temperature increased to RT in these four samples. This is an interesting result, we'll find some other samples to clarify the reason cause this shape in the future work.

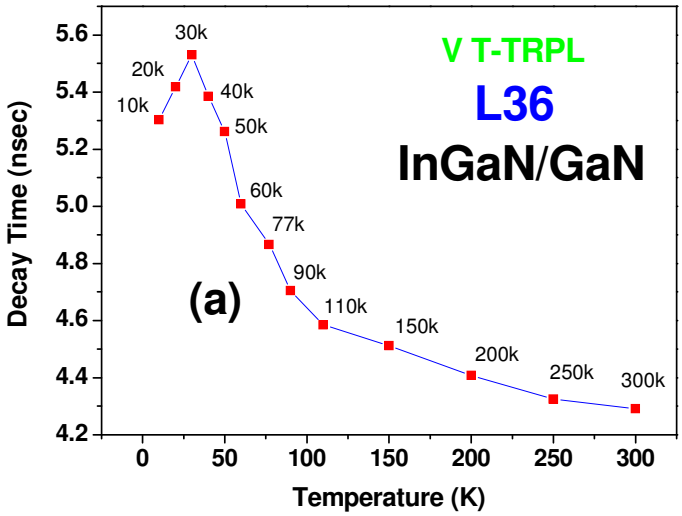
V T-TRPL
L36
InGaN/GaN
(a)
Decay Time (nsec)
Temperature (K)
10k
20k
30k
40k
50k
60k
77k
90k
110k
150k
200k
250k
300k

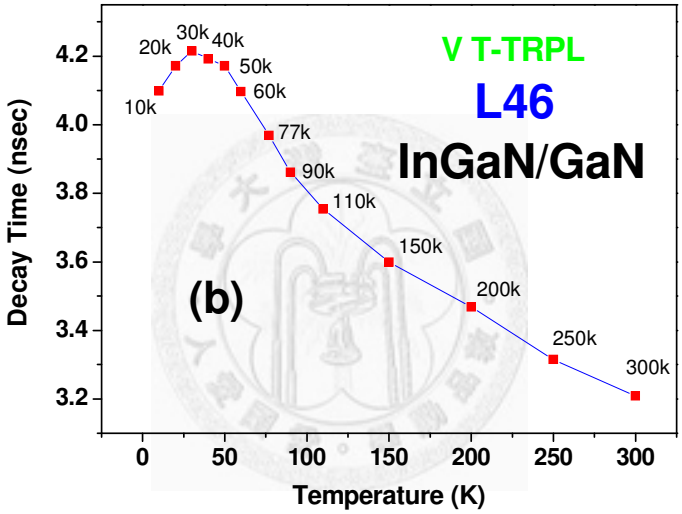
V T-TRPL
L46
InGaN/GaN
(b)
Decay Time (nsec)
Temperature (K)
10k
20k
30k
40k
50k
60k
77k
90k
110k
150k
200k
250k
300k

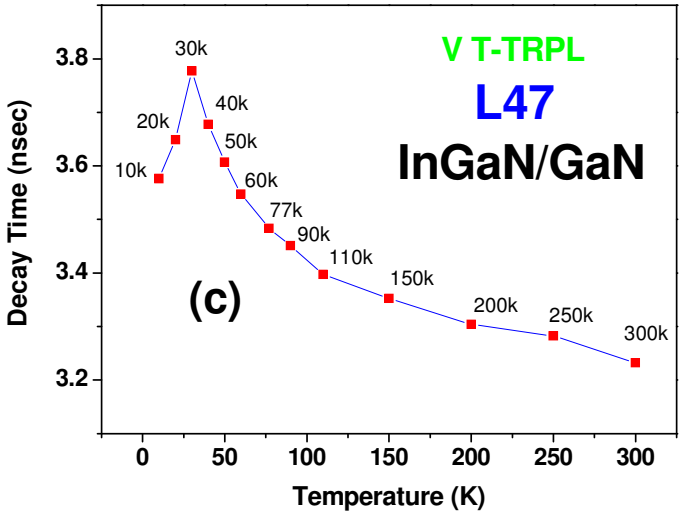
V T-TRPL
L47
InGaN/GaN
(c)
Decay Time (nsec)
Temperature (K)
10k
20k
30k
40k
50k
60k
77k
90k
110k
150k
200k
250k
300k

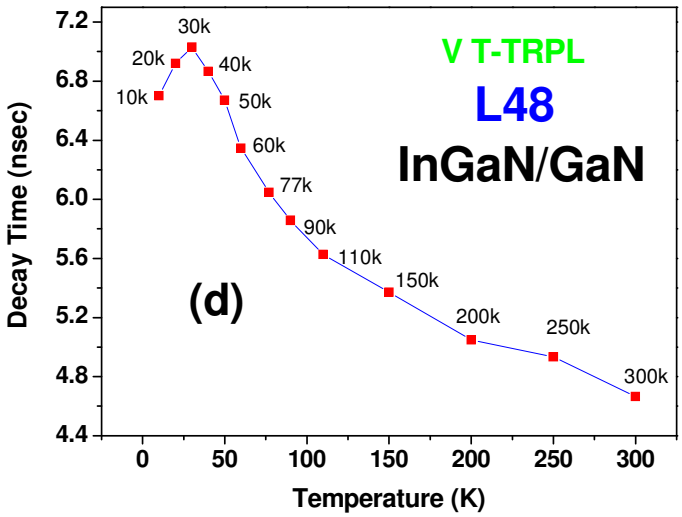

Figure 5.17 *Temperature dependence of PL lifetime τ_{PL} for the InGaN/GaN MQW (a)L36, (b)L46, (c)L47, (d)L48. in the temperature range from 10 to 300 K.*

5.3 Summary

In summary, we investigated the effect of different barrier width on the structural and optical properties include PL, TRPL measurement results of the InGaN MQW samples. At various temperatures, with increasing temperature, carriers transfer between different luminescent centers. From the calculation of activation energy, abnormally high activation energy was obtained, which shows that the excitons are not in the free states. The lower-energy side of the InGaN main emission peak is governed mainly by carrier generation in the GaN barriers and subsequent carrier transfer to the InGaN wells. Therefore, the radiative lifetime at the low-energy side of the InGaN peaks is longer; activation energy is bigger; have a deeper localization depth.

References

[5.1] G. Wetzel, T. Takeuchi, S. Yamagachi, H. Katoh, H. Amano, and I.Akasaki, Appl. Phys. Lett. 73, 1994 (1998).

[5.2] L. Bellaiche, T. Mattila, L.-W. Wang, S.-H. Wei, and A. Zunger, Appl. Phys. Lett. 74, 1842 (1999).

[5.3] X. Li, P. W. Bohn, J. Kim, J. O. White, and J. J. Coleman, Appl. Phys. Lett. 76, 3031 (2000).

[5.4] J. Elsner, R. Jones, M. I. Heggie, P. K. Sitch, M. Haugk, Th. Frauenheim, S. Oberg, and P. R. Briddon, Phys. Rev. B 58, 12571 (1998).

[5.5] F. A. Ponce, D. P. Bour, W. Gotz, and P. J. Wright, Appl. Phys. Lett. 68, 57 (1996).

[5.6] T. Wang, P. J. Parbrook, W. H. Fan, and A. M. Fox, Appl. Phys. Lett. 84, 5159 (2004).

[5.7] H. Q. Ni, Z. C. Niu, X. H. Xu, Y. Q. Xu, W. Zhang, X. Wei, L. F. Bian, Z. H. He, Q. Han, and R. H. Wu, Appl. Phys. Lett. 84, 5100 (2004).

[5.8] D. Bimberg, M. Sondergeld, and E. Grobe, Phys. Rev. B, 4, 3451 (1971).

[5.9] M. E. White, K. P. O'Donnell, R. W. Martin, S. Pereira, C. J. Deatcher, and I. M. Watson, Mater. Sci. Eng. B 93, 147 (2002).

[5.10] C. Gourdon and P. Lavallard, Phys. Status Solidi B 153, 641 (1989).

[5.11] Cheng-Yen Chen, Dong-Ming Yeh, Yen-Cheng Lu, and C. C. Yang, Appl. Phys. Lett. 89, 203113 (2006).

[5.12] Tetsuya Akasaka,a_ Hideki Gotoh, Yasuyuki Kobayashi, Hidetoshi Nakano, and Toshiki Makimoto, Appl. Phys. Lett. 89, 101110 (2006).

[5.13] T. Onuma, S. Keller, S. P. DenBaars, J. S. Speck, S. Nakamura, and U. K. Mishra, T. Sota, S. F. Chichibua, Appl. Phys. Lett. 88, 111912 (2006).

[5.14] Seiji Nagahara,a_ Munetaka Arita, and Yasuhiko Arakawa, Appl. Phys. Lett. 88, 083101 (2006).

[5.15] S. F. Chichibu, A. C. Abare, M. S. Minsky, S. Keller, S. B. Fleisher, J. E. Bowers, E. Hu, U. K. Mishra, L. A. Coldren, S. P. Denbaars, and T. Sota, Appl. Phys. Lett. 73, 2006 (1998).

[5.16] Y. Narukawa, Y. Kawakami, M. Funato, Sz. Fujita, Sg. Fujita, and S.Nakamura, Appl. Phys. Lett. 70, 981 (1997).

[5.17] Y. Narukawa, S. Saijou, Y. Kawakami, S. Fujita, T. Mukai, and S. Nakamura, Appl. Phys. Lett. 74, 558 (1999).

[5.18] M. E. White, K. P. O'Donnell, R. W. Martin, S. Pereira, C. J. Deatcher, and I. M. Watson, Mater. Sci. Eng. B 93, 147 (2002).

Chapter 6 Others

6.1 Brillouin scattering spectrum of 6H-SiC

6.1.1 Introduction

Silicon carbide is well known for its extreme hardness and excellent resistance to thermal shock, oxidation, and corrosion. Variant forms of powders, fibers, and sintered ceramics of silicon carbide are widely used as structural and engineering components in extreme environments. The availability of bulk and thin-film single crystals of silicon carbide has led to new electronic applications such as semiconducting and light-emitting devices. The crystal structure of silicon carbide is complicated because of the existence of various polytypic phases and the relative ease of incorporating defects and impurities.1 Therefore, it is important to establish a database of basic properties of pure SiC single crystals of definite polytypes so as to provide a benchmark for evaluation of tailored properties of novel SiC-based materials. As part of our recent studies of effects of neutron irradiation on the mechanical and transport properties of SiC single crystals,2 we report in this article the measurements of the elastic constants of 4H and 6H polytypic phases using Brillouin-scattering techniques. As a consequence of *sp*3 hybridization of the atomic orbitals, the basic structural elements of silicon carbide are tetrahedra with one kind of atom at the center and four unlike atoms at the corners. The crystal structure, which resembles the diamond lattice, can be constructed from

alternating packed layers of Si and C atoms occupying tetrahedral sites. Since configurations based on variant stacking sequences differ little in the free energy, a large number of different structures (polytypes) occur. The 4H and 6H polytypes correspond to stacking sequences of *ABCB*... and *ABCACB*..., respectively. Both crystal structures exhibit hexagonal symmetry. Other important polytypes include the 3C and 15R structures, which are cubic and rhombohedral, respectively [6.1].

6.1.2 Resuilts

Brillouin-scattering experiments were performed on 3 samples, 6HSiC052, 6HSiC177, 6HSiC intrinsic. The sample name 6H-SiC052 means its resistivity (Ω-cm) is 0.052. The sample name 6H-SiC177 means its resistivity (Ω-cm) is 0.177. The 6HSiC-intrinsic is undoped. And an laser (λ＝532 nm) was used for GaN on sapphire measurements. Our Brillouin experiment utilizes a 60°/60° symmetric scattering geometry, which yields acoustic velocity measurements independent of the refractive index of the specimen and the Brillouin frequency shift Δω is directly related to the acoustic velocity V and the incident laser wavelength λ. In this work, Brillouin scattering measurements of InGaN/GaN on sapphire and GaN on sapphire with angular variations over 0 to 180 degrees with interval of 15 degrees.

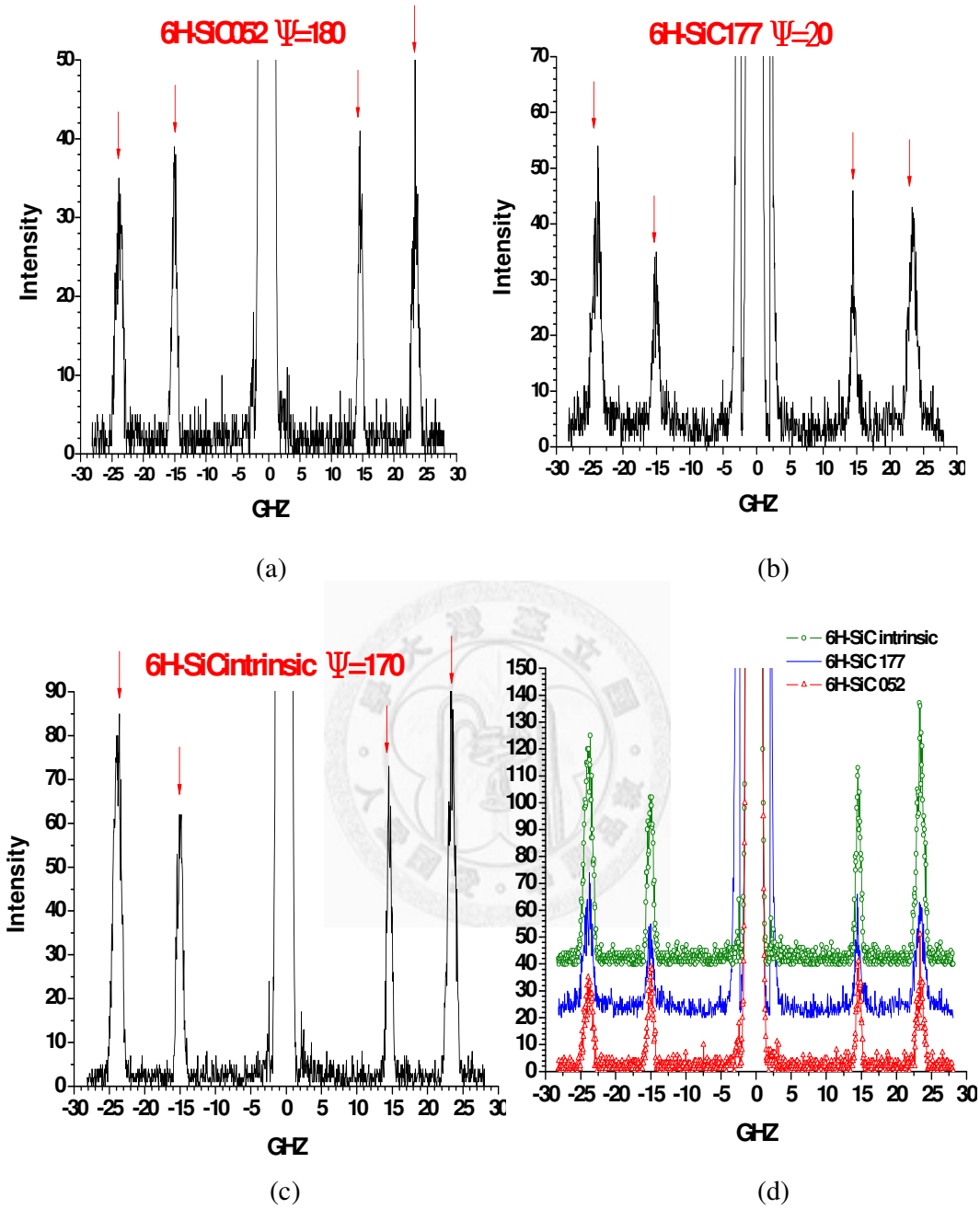

Figure 6.1 *Brillouin spectrum of (a)6HSiC052 (b)6HSiC177 (C)6HSiC intrinsic*

(d) Brillouin spectrum of (a), (b), and (c) in one figure

Figure 6.1 showed the Brillouin scattering spectrum of samples ,6HSiC052, 6HSiC177, and6HSiC intrinsic. Using equation (3.1) to calculate the velocities of

phonon acoustic waves. But figure 6.1 just showed two peaks of each sample. Computing the elastic constants C_{ij} by equation (3.2) need the velocities of LA, TA1, TA2. So we guess the velocities of TA1,TA2 are the same and try to compute the elastic constants $C_{ij.}$ But as figure 6.2 showed, the elastic constants can not fitted well. We still try to figure out the problem on fitting and finding why the spectrum just showed two peaks.

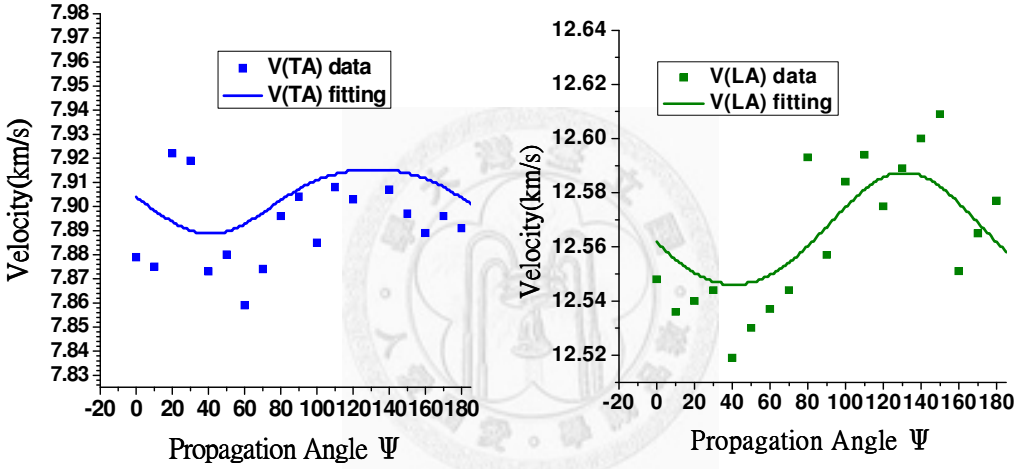

Figure 6.2 *(a) Elastic constants fitting results of 6H052*

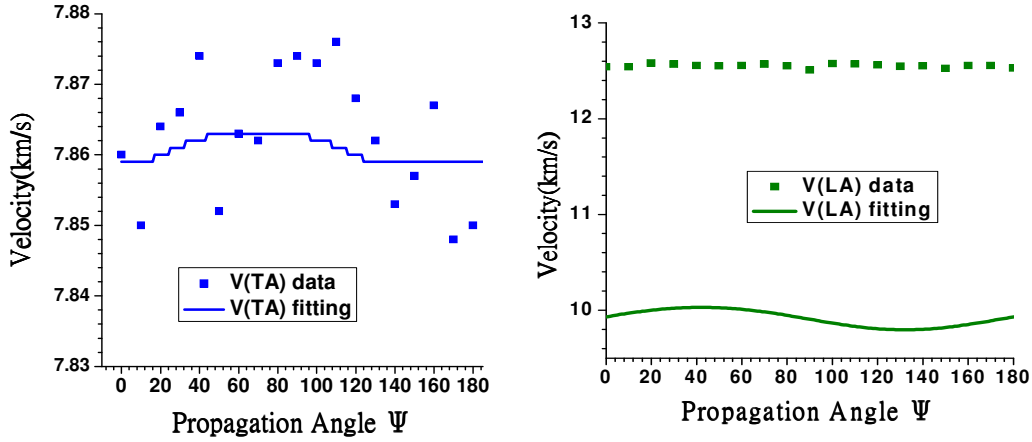

)

Figure 6.2 *(b) Elastic constants fitting results of 6H177*

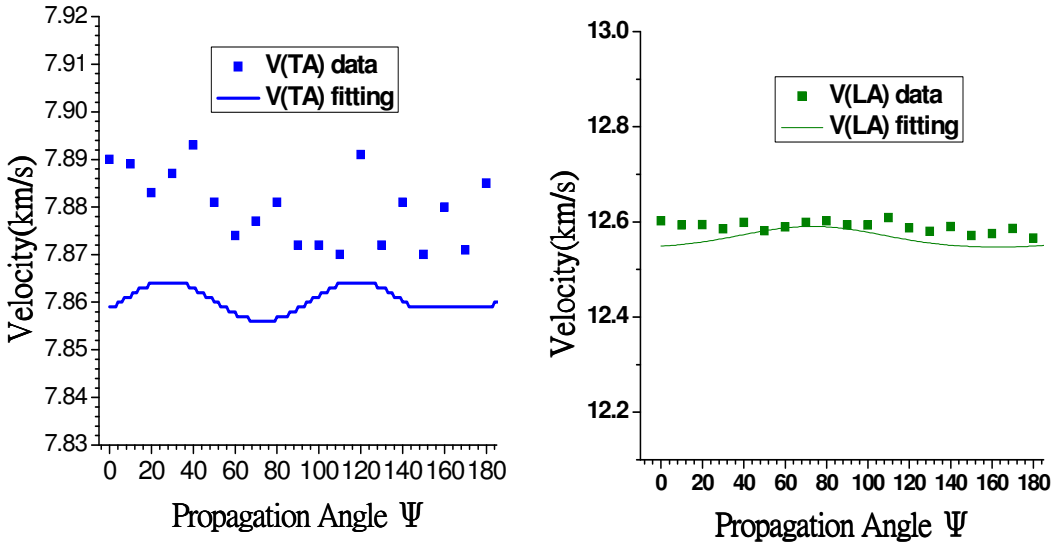

Figure 6.2 *(c) Elastic constants fitting results of 6H intrinsic*

6.2 InGaN N K-edge X-ray Asorption Near Edge Spectroscopy (XANES)

6.2.1 Synchrotron Radiation Beamline End Station

The HSGM beamline is one of the earlier versions of the Dragon beamline using spherical optical elements and a movable exit slit to maximize the photon throughput and energy resolving power. It consists of one horizontal focusing mirror (HFM), one vertical focusing mirror (VFM), one spherical grating monochromator with 4 gratings, and one toroidal refocusing mirror. This beamline covers the spectral range from 60 eV to 1250 eV, with an average energy resolving power of 5000. The end-station is primarily designed for studying condensed phase photochemistry and the electronic structures of new materials.

This beamline has been operational since 1993. Studies of desorption dynamics of molecular adsorbates, relaxation dynamics of core-excited molecules, synchrotron radiation induced surface photochemistry, electronic structure of high-Tc superconductors, and magnetic materials have been performed at this beamline.

Type	1.5 GeV Bending Magnet	
Source Size	Horizontal	s_h = 0.12 mm
	Vertical	s_v = 0.055 mm
Energy Range	60 ~ 1250 eV	

Table 6.1 *Light source of BL20A.*

Horizontal Acceptance Angle	11 mrad			
Total Power	23 W			
Monochromator	6 meter SGM			
Mirrors	Spherical HFM/VFM. Toroidal RFM			
Arm Length	Slit 1 ~ Grating		172 cm	
	Grating ~ Slit 2		400 ~ 500 cm	
Slit Opening	Slit 1		5 ~ 2000 μm	
	Slit 2		5 ~ 2000 μm	
Gratings				
Groove Density (ℓ/mm)	200	400	700	1200
Scanning Range (eV)	60 ~ 200	150 ~ 400	250 ~ 600	400 ~ 1250
Beam Size at Sample	1.5 mm × 1.0 mm			

Table 6.2 *Optical Parameters*

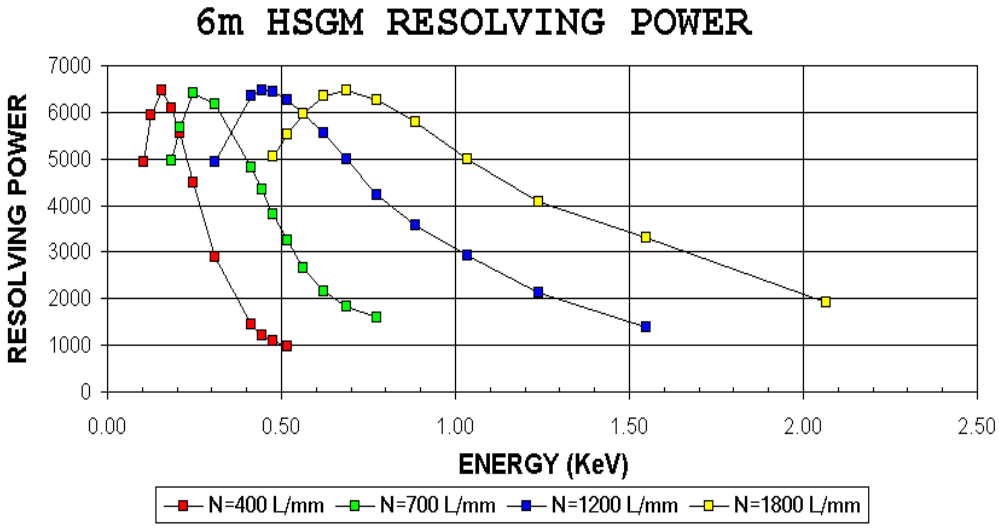

Table 6.3 *Calculated Resolutions*

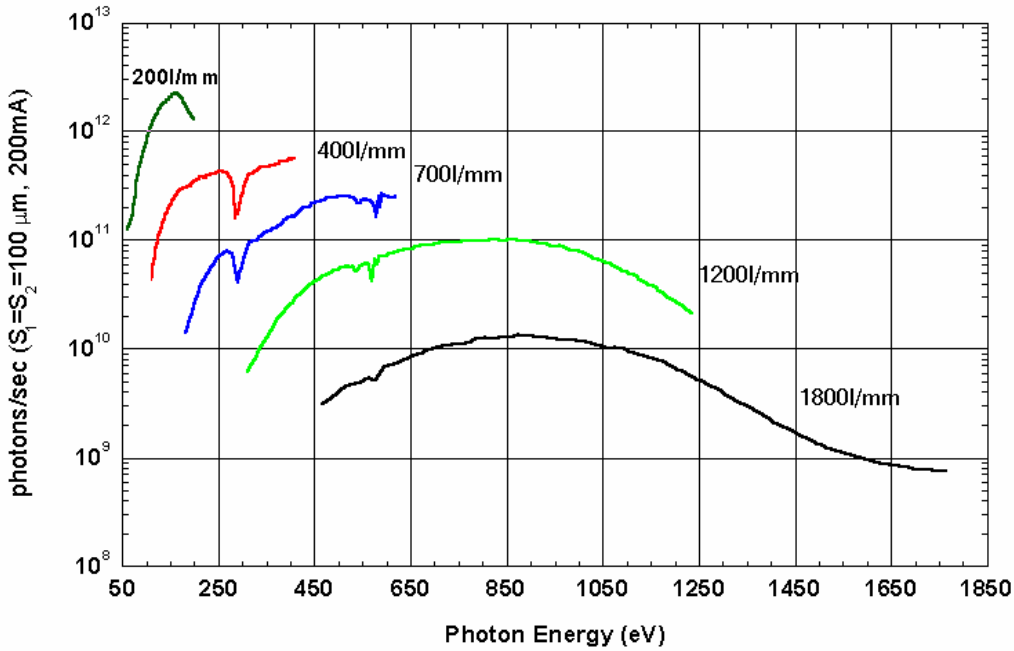

Figure 6.3 *Photon flux of BL20A*

6.2.2 Results

Prior to analysis the NEXAFS spectra were normalized to the primary beam current and corrected for energy shifts using the photocurrent from a Au grid with high transmissivity (90%) positioned at the exit slit of the monochromator. Furthermore, they were subjected to linear background subtraction (by fitting the pre-edge region) and normalized to the figure 6.4 . Fitting of a representative spectrum from a hexagonal GaN atomic limit (~ 440 eV), as described previously [6.2]. The energy positions of the absorption edge (E_{abs}) and NEXAFS resonances (E_i) were determined from fitting of the spectra in the energy range 400–422 eV using a sigmoidal ($y = A/ [1+\exp(-(x-x_0)/w)]$, where A, x_0 and w stand for the amplitude, the center, and the width, respectively) to simulate transitions to the continuum, and six gaussians (G_i, i=1, . . . , 6), to simulate transitions to bound states. The E_{abs} is defined as the inflection point of the sigmoidal. The fitting of a representative spectrum from GaN is shown in figure 6.4.

The allowed transitions in hexagonal materials are from the initial N1s state of a_1 symmetry to final Np states, i.e. $1a_1 \rightarrow a^*$ and $1a \rightarrow e^*$ [13,14] (according to dipole selection rules the angular momentum of the initial and the final states should differ by ±1). The a_1^* states result from mixing of s and p_z atomic orbitals (vector orbitals) and should be strongest for grazing incidence, while e* states result from mixing of p_x and p_y atomic orbitals (plane orbitals) and should be strongest for normal incidence. As it

was recently reported by Katsikini [6.2-6.4], in pure hexagonal AlN and GaN, the energy positions and the full width at half maximum (FWHM), of the various gaussians which simulate the NEXAFS transitions do not depend on the angle of incidence, while the area under the gaussians depends linearly on $\cos^2\theta$ [6.9].

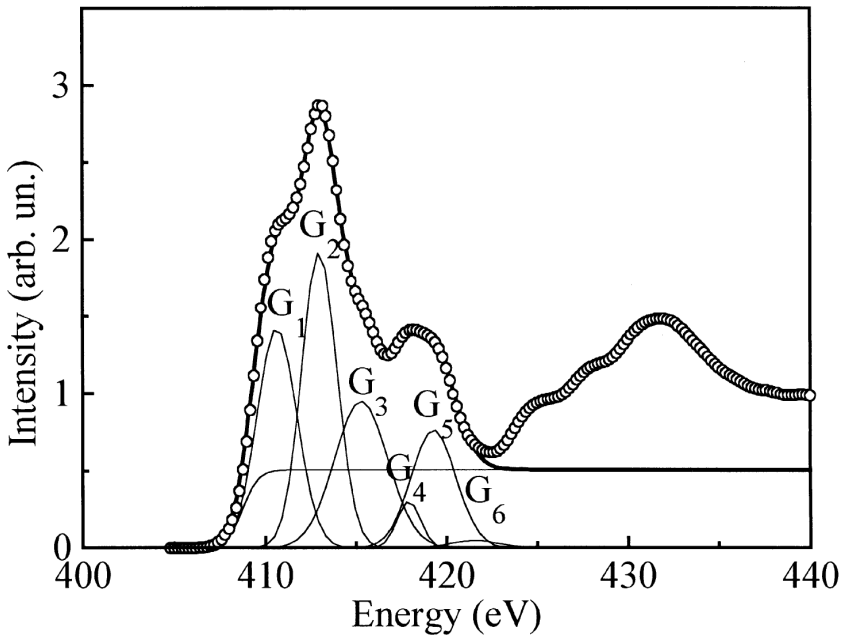

Figure 6.4 *Fitting of a representative spectrum from a hexagonal GaN from [6.9]*

InGaN N K-edge are shown in figure 6.5, we do the 6 gaussian peaks fitting for 3 samples, InGaN/GaN on sapphire were growm bu MOCVD, 1947i~15%, 1942i~29%, and 1934i~34%, respectively.The fitting peaks (G_i, i=1, . . . , 6) position were list in table 6.4

	G_1	G_2	G_3	G_4	G_5	G_6
GaN[6.9]	*410.7*	*413.2*	*415.5*	*417.7*	*419.5*	*421.5*
$In_{0.15}Ga_{0.85}N$	*401.63*	*404.11*	*406.29*	*408.58*	*410.58*	*411.73*
$In_{0.29}Ga_{0.71}N$	*402.31*	*404.75*	*406.95*	*409.20*	*411.15*	*413.48*
$In_{0.34}Ga_{0.66}N$	*402.17*	*404.63*	*406.84*	*409.01*	*411.06*	*413.14*

Table 6.4 *G_1~G_6 position of GaN and $In_xGa_{1-x}N$*

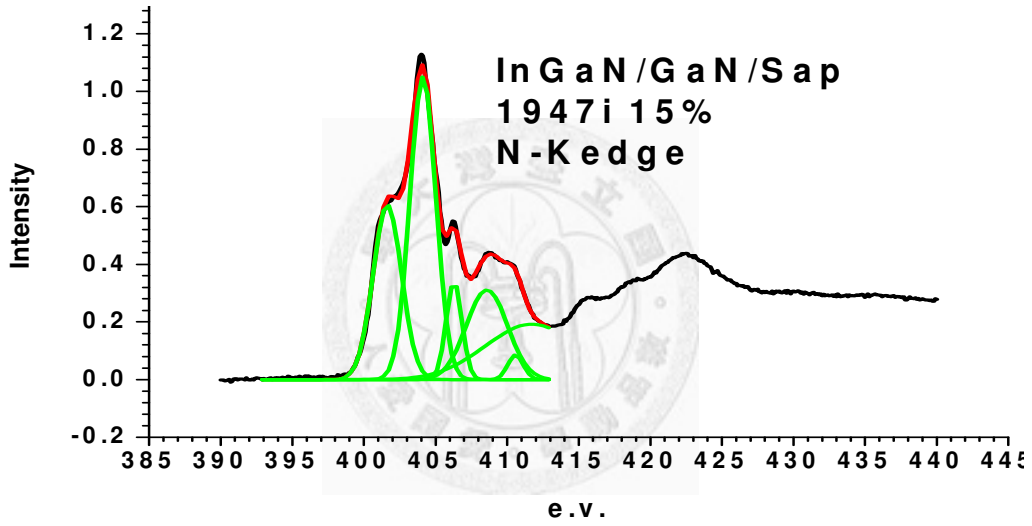

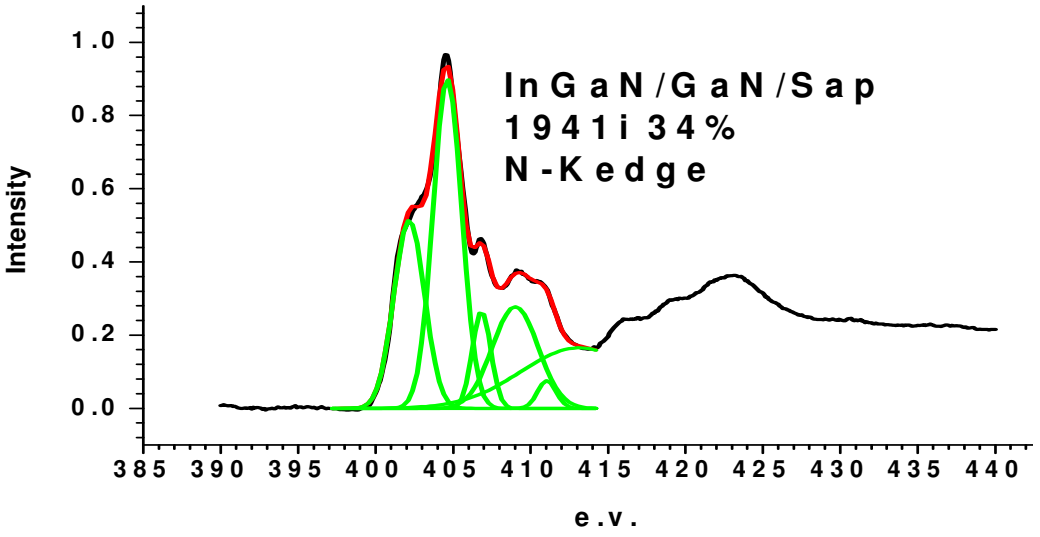

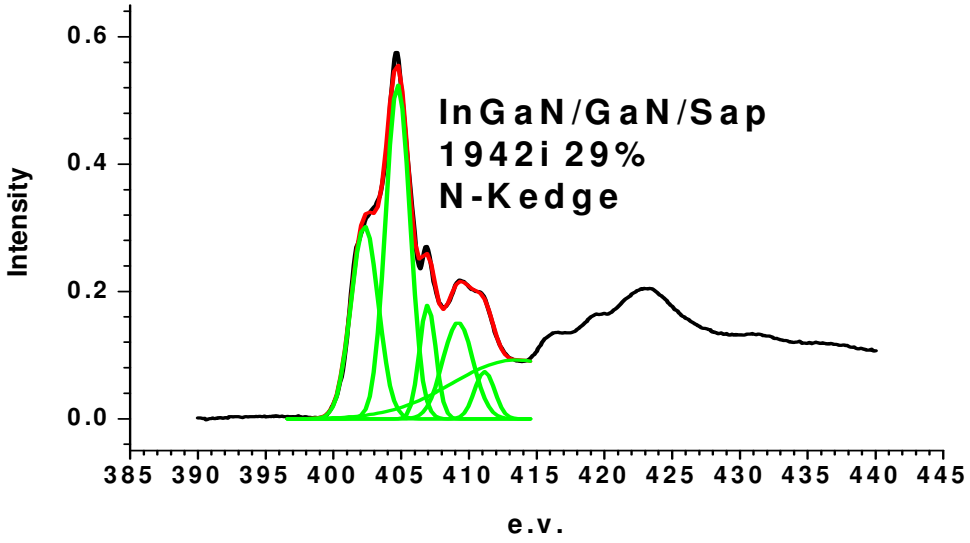

Figure 6.5 *N K-edge XANES of* $In_xGa_{1-x}N$

Reference

[6.1] K. Kamitani, M. Grimsditch, J. C. Nipko, and C.-K. Loong, M. Okada, I. Kimura, J. Appl. Phys. 82 (6), 15, 3152 (1997)

[6.2] M. Katsikini, E.C. Paloura, T.D. Moustakas, Appl. Phys. Lett. 69, 4206. (1996)

[6.3] M. Katsikini, E.C. Paloura, T.D. Moustakas, J. Appl. Phys 83, 1437(1998)

[6.4] M. Katsikini, E.C. Paloura, T.S. Cheng, C.T. Foxon, J. Appl Phys. 82, 1166 (1997)

[6.9] M. Katsikini, E.C. Paloura , M. Fieber-Erdmann, E. Holub-Krappeb, D. Korakakisc, T.D. Moustakas, Journal of Electron Spectroscopy and Related Phenomena 101, 695 (1999) 695–699